UNIVERSITÀ
DEGLI STUDI
DI PADOVA

Sede Amministrativa: Università degli Studi di Padova
Dipartimento di Ingegneria dell'Informazione

SCUOLA DI DOTTORATO DI RICERCA IN INGEGNERIA DELL'INFORMAZIONE
INDIRIZZO DI SCIENZA E TECNOLOGIA DELL'INFORMAZIONE
CICLO XXVIII

Islanding and Stability of Low Voltage Distribution Grids with Renewable Energy Sources

Direttore della Scuola: Ch.mo Prof. Matteo Bertocco
Coordinatore d'Indirizzo: Ch.mo Prof. Carlo Ferrari
Supervisori: Ch.mo Prof. Paolo Mattavelli e Ch.mo Prof. Paolo Tenti

Dottorando: Stefano Lissandron

Abstract

The employment of renewable energy sources is driving an increase of the amount of embedded generation that is connected to the medium and low voltage distribution networks. This penetration brings new challenges to improve the grid operation, but also concerns because these parts of the grid were not designed to host generation. These energy sources are usually interfaced by power electronic converters, e.g. inverters, which are flexible in terms of control capability. For instance, they can control output currents or voltages, both in phase and amplitude. So, a proper design of the regulators of inverters can improve distribution efficiency and reliability of the grid.

Distributed generation can also increase power quality and provide voltage regulation in the distribution grid. For instance, parts of the electric network can be operated intentionally as autonomous networks, when the connection to the mains is lost. In this way, the reliability of the grid can increase and uninterruptible power supply capabilities can be achieved. However, in autonomous or islanded operation the voltage must be managed by the inverters to correctly feed all the loads, since the main control is missing, and the load power has also to be shared among the distributed energy resources.

On the other side, the penetration of distributed generation can also be dangerous in some particular cases, if it is not properly managed. For instance, islanded operation can appear also unintentionally and without being expected, because of the local generation. In this case, islanded operation is a problem for the electric grid because it may damage the electric equipment or create safety hazard for the line workers. The probability of unintentional islanded operation has increased due to the newly introduced standards for generators, which in

particular impose wider frequency and voltage ranges and active and reactive power support capabilities using of P/f and Q/V droop characteristics. Anti-islanding protections that each inverter is equipped with, may fail to detect the grid transition and so uncontrolled islanded operation may appear.

In this scenario, some contributions of this Thesis are related to the islanded operation of parts of the electric grid. First, the unintentional islanding risk is studied considering the newly introduced standards for distributed energy resources and in particular for photovoltaic sources. A potential increase of such phenomenon will be shown and suggestions will be provided in order to reduce this risk.

Then, another part of the Thesis addresses the intentional islanded operation. A local controller for inverter of distributed energy resources is presented to manage a part of the grid during grid-connected and autonomous operating modes and also during the transition: during grid-connected operation, the controller tracks active and reactive power references and, during islanded mode, it exploits the droop control properties to share the load among the distributed energy resources. The peculiarity of this regulator is that it does not need to identify the particular operation mode and so a smooth transition from grid-connected to islanded mode can be achieved with no communication within the power grid or among the disconnecting switch and distributed energy resources.

Another important issue in these complex scenarios is the system stability: the interactions of more and more power electronics-interfaced power systems can indeed worsen the power quality and the stability of distribution networks. These phenomena can be addressed by analyzing the source and load impedances at the section of interaction between two subsystems. Well-established approaches exist for DC and three-phase AC networks to analyze the source-load system. Some papers focused also on single-phase AC systems, whose study is generally more difficult due to their time-varying characteristics. Another contribution of this Thesis is an extension of a method to study the stability of single-phase AC power systems, together with its experimental validation. This approach bases on the dynamic phasor method to determine the 2-dimensional source and load impedances and it addresses the stability with

the Generalized Nyquist stability Criterion, previously used to study balanced three-phase AC system stability.

Distribution grid stability can be studied also focusing on the high level interactions of its multitude of devices, such as generators and loads, and this can be done considering approximated and general models that can account different types of device. The last contribution of this work is the system stability and dynamic studies of large distribution grids, with large penetration of distributed generation. Simplified models for the single units are linked together in large small-signal models, with a scalable and automatable approach for the dynamic analysis, that can address the study of a grid with a generic number of node, with no more effort by the user. In particular, this activity was done during a visiting research period done by the Author at the Institute Automation of Complex Power Systems of RWTH Aachen University (Germany).

The results of this Thesis are given in terms of analytic and simulation studies, together with experimental validations. Also hardware-in-the-loop and real-time simulation approaches have been used for implementation and validation purposes.

Sommario

L'impiego di fonti di energia rinnovabile sta portando ad un aumento della quantità di generazione integrata connessa alle reti di distribuzione di media e bassa tensione. Questa penetrazione sta aprendo nuove sfide per migliorare il funzionamento della rete elettrica, ma anche alcuni rischi e problemi perché queste parti di rete non erano inizialmente state progettate per ospitare generazione. Tali sorgenti energetiche sono solitamente interfacciate da convertitori elettronici di potenza, ad esempio inverter, che risultano essere unità estremamente flessibili in termini di funzionalità e controllo. Ad esempio, gli inverter hanno grande autonomia sul controllo delle correnti e tensioni d'uscita, sia in fase che in ampiezza. Quindi, una corretta ed appropriata progettazione dei loro regolatori può migliorare l'efficienza della distribuzione e l'affidabilità della rete.

La generazione distribuita può inoltre migliorare la qualità della tensione fornita ai carichi all'interno della rete elettrica. Ad esempio, parti di rete possono essere mantenute in funzionamento intenzionalmente come reti autonome anche quando la connessione alla rete principale viene a mancare. In questo modo, l'affidabilità della rete può aumentare, ottenendo sempre continuità di servizio di fornitura dell'energia elettrica. Tuttavia, in funzionamento autonomo o ad isola la tensione deve essere controllata dagli inverter al fine di alimentare correttamente tutti i carichi, dal momento che il controllo solitamente effettuato dal gestore di rete viene a mancare, e la potenza richiesta dai carichi deve anche essere suddivisa adeguatamente tra le risorse energetiche distribuite.

Dall'altro lato, l'aumento della generazione distribuita può portare anche ad avere dei rischi aggiuntivi in alcuni casi, se non viene gestito correttamente. Ad

esempio, il funzionamento ad isola può manifestarsi anche involontariamente e senza essere previsto a causa della generazione locale che può mantenere in funzione parti di rete elettrica. In questo caso, il funzionamento ad isola è un problema per la rete elettrica perché può danneggiare le apparecchiature elettriche o creare pericoli per la sicurezza dei lavoratori. La probabilità di funzionamento involontario ad isola è aumentata di recente a causa di nuove normative introdotte per i generatori le quali, in particolare, impongono gamme di funzionamento più ampie per frequenza e tensione e impongono il supporto alla regolazione della frequenza e della tensione con caratteristiche droop di tipo P/f e Q/V ai singoli generatori. Ogni inverter può essere dotato di protezioni contro il modo di funzionamento involontario ad isola, tuttavia tali protezioni potrebbero in alcuni casi non riuscire a riconoscere la transizione dal modo di funzionamento in parallelo alla rete principale a quello ad isola. Questo potrebbe impedire la disconnessione degli inverter e portare al modo di funzionamento ad isola non controllata.

In questo scenario complesso, alcuni contributi di questa Tesi sono legati al funzionamento ad isola di parti di rete elettrica. In primo luogo, il rischio di formazione dell'isola involontaria è studiato considerando l'effetto delle nuove normative introdotte per la connessione delle risorse energetiche distribuite ed in particolare delle fonti fotovoltaiche. Si mostrerà che tale rischio è potenzialmente in aumento e alcuni suggerimenti potranno essere ricavati per cercare di contenere il fenomeno di isola non intenzionale.

Un'altra parte della Tesi affronta il modo di funzionamento in isola intenzionale. Un controllore locale per inverter per risorse energetiche distribuite è presentato per gestire una parte di rete durante il funzionamento in parallelo al gestore principale, durante il funzionamento autonomo (o ad isola) e anche durante la transizione: durante il funzionamento in parallelo alla rete, il regolatore insegue riferimenti di potenza attiva e reattiva e, nella modalità ad isola sfrutta le proprietà del controllo droop al fine di suddividere il carico tra le risorse energetiche distribuite e per regolare la tensione. La peculiarità di questo regolatore è che non necessita di identificare la particolare modalità di funzionamento e quindi la transizione dal modo di funzionamento in parallelo alla rete principa-

le a quello autonomo può avvenire senza comunicazione all'interno della rete elettrica, né tra gli inverter né con il sezionatore che connette la rete al gestore principale.

Nello scenario fin qui descritto, un altro aspetto importante è quello legato alla stabilità del sistema, più o meno esteso: le interazioni tra sistemi di conversione dell'energia sempre più basati su convertitori elettronici di potenza possono infatti peggiorare la qualità dell'alimentazione e la stabilità della rete. Questi fenomeni possono essere affrontati analizzando le impedenze di sorgente e carico in corrispondenza della sezione di interazione tra due sottosistemi. Per questo, esistono approcci efficaci per quanto riguarda le reti in corrente continua ed alternata di tipo trifase per analizzare il sistema sorgente-carico. Alcuni lavori si sono concentrati anche sui sistemi a corrente alternata monofase, il cui studio è generalmente più complesso a causa delle loro caratteristiche di tempo-varianza. Un altro contributo di questa Tesi è la descrizione di un'estensione per lo studio di stabilità di sistemi di alimentazione in corrente alternata monofase, assieme alla sua validazione sperimentale. Questo metodo si basa sull'applicazione dei fasori dinamici per determinare le impedenze di sorgente e di carico di tipo bidimensionale e affronta la stabilità con il criterio generalizzato di Nyquist, precedentemente impiegato per lo studio di sistemi trifase in corrente alternata bilanciati.

La stabilità della rete di distribuzione può essere studiata anche concentrandosi sulle interazioni di alto livello dovute alla sua moltitudine di dispositivi, come generatori e carichi, e questo può essere fatto considerando modelli approssimati e generali che possono descrivere diverse tipologie di dispositivo. L'ultimo contributo di questo lavoro è lo studio di stabilità di sistema e lo studio dinamico di grandi reti di distribuzione, con grande penetrazione di generazione distribuita. Modelli semplificati per i singoli dispositivi sono collegati insieme in grandi modelli di piccolo segnale, con un approccio scalabile e automatizzabile per l'analisi dinamica, che può affrontare lo studio di una rete con un numero generico di nodi, senza richiedere sforzi aggiuntivi da parte dell'utente. In particolare, tale attività è stata svolta nel corso di un periodo di ricerca presso l'Istituto Automation of Complex Power Systems di RWTH Aachen University

(Germania).

I risultati di questa Tesi sono supportati da studi analitici, tramite simulazione al calcolatore e con validazioni di tipo sperimentale. Inoltre, sono stati utilizzati strumenti quali l'hardware-in-the-loop e la simulazione in tempo reale al fine di implementare alcuni concetti e poterli validare.

Acknowledgments

I am very grateful to my advisor and professor Paolo Mattavelli for the guidance and the possibilities he has given me during these last three years. Knowing him and working with him, I have appreciated and enjoyed several times his competence and precision. With him, I have had the opportunity to learn a lot in several fields, starting from technical and academic ones and going to professional and personal fields: he has positively influenced all of them. All the work in this Thesis has been done with his help.

I want to thank prof. Paolo Tenti because he has been the first who approached me to the topics I have worked on during the last years. He developed in me the interests for this research field and he gave me the possibility of pursuing this Ph.D.

I thank also Luca Dalla Santa and Riccardo Sgarbossa for their cooperation and help to obtain some results that will be presented in this Thesis.

Finally, I want to thank all my family and my friends who loved me in these years and who always will love me in the future. I will always be grateful to my mother and my father for all the goals I have reached so far and for those I will reach soon.

Contents

Nomenclature

Acronyms

BIBO	Bounded-Input Bounded-Output
DER	Distributed Energy Resource
DFT	Discrete Fourier Transform
DG	Distributed Generation
FFT	Fast Fourier Transform
FPGA	Field Programmable Gate Array
GNC	Generalized Nyquist stability Criterion
HIL	Hardware-In-the-Loop
HV	High Voltage
LKI	Kirchhoff's current laws
LKV	Kirchhoff's voltage laws
LV	Low Voltage
MIMO	Multiple-Input Multiple-Output
MPP	Maximum Power Point
MPPT	Maximum Power Point Tracking

MV	Medium Voltage
NDZ	Non-Detection Zone
NI	National Instruments
PCC	Point of Common Coupling
PF	Power Factor
PLL	Phase-Locked Loop
PV	PhotoVoltaic
PWM	Pulse-Width Modulation
RES	Renewable Energy Sources
RT	Real-Time
SOGI	Second-Order Generalized Integrator
SRF-PLL	Synchronous Reference Frame Phase-Locked Loop
UIO	Unintentional Islanded Operation

Symbols

$\mathbf{x}$	Complex signal or number
$\mathbf{x}^I$	Imaginary part of $\mathbf{x}$
$\mathbf{x}^R$	Real part of $\mathbf{x}$
$\triangleq$	Definition
Δ	Small-signal variation
$\mathrm{diag}\,(\cdot)$	Diagonal matrix having the entry vector as diagonal elements
$\mathbb{I}_n$	Identity matrix of dimensions $n \times n$

$\mathbb{C}$	Set of complex numbers
$\mathbb{R}$	Set of real numbers
$\mathfrak{Im}$	Imaginary part of a complex quantity
$\mathfrak{L}$	Laplace transform
$\mathfrak{Re}$	Real part of a complex quantity
$\langle x \rangle_k$	Dynamic phasor of order k of the signal x
j	Imaginary component or unit
s	Laplace independent complex variable
$x(t)$	Time domain signal (indicated with lowercase letter)
x_d	d component of the space vector $\mathbf{x}_{dq}$
x_q	q component of the space vector $\mathbf{x}_{dq}$
*	Conjugation of complex number
^{T}	Transposition of matrix

Chapter 1

Issues and challenges for future grids

During the last years, Distributed Generation (DG) from Renewable Energy Sources (RES) has significantly increased because of growing power demand and increasing concerns about fossil fuels. Among the different energy sources, the diffusion of PhotoVoltaic (PV) systems is the fastest-growing within the electric distribution systems worldwide and its employment is driving an increase of the amount of embedded generation connected to the Medium Voltage (MV) and Low Voltage (LV) distribution networks [1–3]. Figs. 1.1 and 1.2 show the fast spread of Distributed Energy Resources (DERs) within the power system, respectively for the Italian and German cases.

As this penetration increases, there are some issues that can appear in the

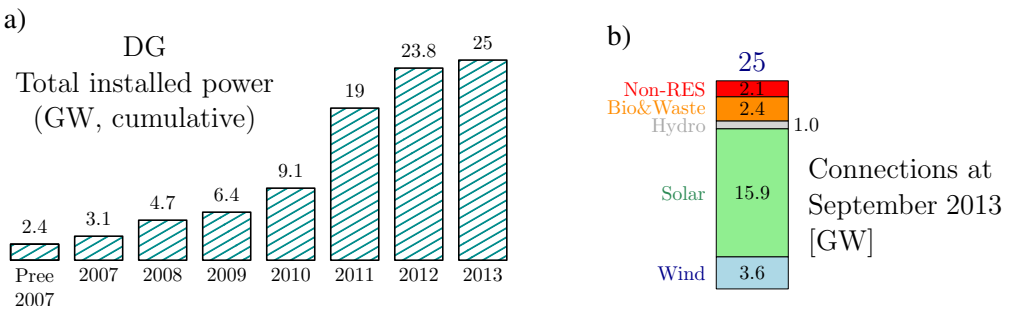

Figure 1.1: a) Historic development of the installed capacity of DERs, and b) share of DG in September 2013 (Italian case) [4]

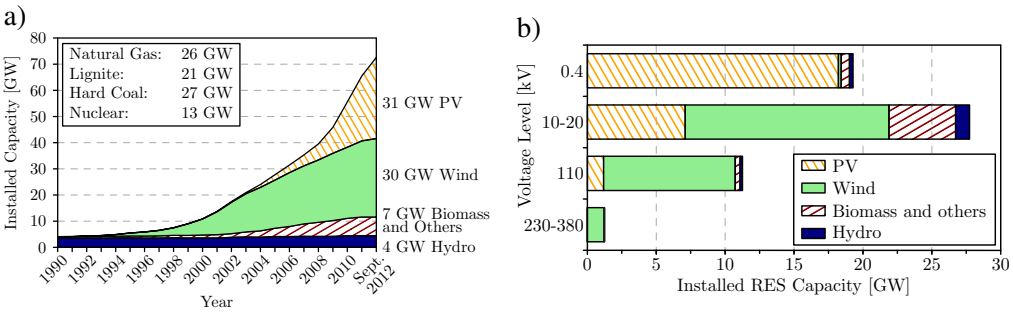

Figure 1.2: a) Historic development of the installed capacity of RES compared with conventional power sources (March 2012), and b) distribution of RES over the typical nominal voltage levels (German case) [5]

electric grid at MV and especially LV levels, because the largest part of DERs is connected here and because this part of the grid was not originally designed to host generating units [1, 5, 6]. One example of these risks is the increase of feeder voltages, especially when the power generation is high and the load demand is low. Also voltage flicker can be caused by DG because of the intermittent nature of RES. Considering PV units, their output powers strongly rely on the solar irradiance that can vary rapidly, for example when the clouds move fast. These two issues are particularly evident when large PV-DG plants are connected close to the end of long feeders. Furthermore, DG can increase the line unbalances, since the largest part of PV units has single-phase connection [1, 6].

Voltage fluctuations, caused by the intermittence, impact on the voltage regulation devices, usually load tap chargers, which may experience a larger number of operations per year. The lifetime of these devices, and in general of all automatic line equipment, such as capacitors and voltage regulators, can be reduced by the increasing DG penetration, requiring more maintenance [1, 6]. Intermittence causes also frequent switching of voltage-controlled capacitor banks and frequent operation of voltage regulators, leading to reactive power flow fluctuations. If these variations are large enough, this may also affect subtransmission and transmission systems, with possible important economic impacts, because the transmission of reactive power is more expensive than its local supply [1].

In high penetrated DG scenarios, another possible issue is the reverse power flow on the feeder, when the local DG exceeds the local load demand. For instance, in Italy almost $20\,\%$ of High-Voltage (HV) to MV transformers experienced reversed power flow for more than 450 hours in 2013 [4]. This phenomenon can negatively affect protection systems, since they are usually designed for unidirectional power flows [1, 5]. Finally, also power losses of the grid are affected by DG: while low and moderate DG penetration levels can help reduce the losses, too high penetration levels could increase them [1].

DG can increase frequency variations of the electrical system, for example causing over-frequencies when there is a surplus of generation. In this situation, a sudden disconnection of a large share of the PV generation capacity can cause severe under-frequencies and even rolling blackouts [5]. New interconnection requirements are trying to provide smoother responses to frequency variations of PV systems, when system over-frequencies appear [5, 7, 8].

DERs are usually interfaced by power electronics converters, i.e. inverters, to the grid and their control capabilities can be beneficial for the distribution grid operation [2, 3, 9]. For example, they can support the voltage, regulate the Power Factor (PF), and balance the currents on each phase, providing a general improvement of distribution efficiency, reliability, and power quality [6]. Small-scale DERs are now forced by some standards to provide all the available active power at unitary PF and no reactive power control is allowed [6, 10, 11]. However, allowing the inverters to inject reactive power can help reduce voltage fluctuations caused by intermittence of RES, reduce the steady-state voltage rise, and reduce the distribution losses [1,5,6]. The reduction of the fluctuations can minimize the impact of PV on voltage regulators and switched capacitors extending their life cycle, while steady-state voltage support can help accommodate more DERs in the grid [6]. With other words, exploiting active and reactive power control capabilities of inverters, it is possible to decrease their penetration impact, alleviating the problems described so far [5].

In this scenario, this Chapter first describes how to reorganize the grid structure, defining and illustrating the concept of *microgrid*, and how this entity can help improve grid performances in Sec. 1.1. Particular attention is given on how

to improve the reliability of the grid, in case of mains disconnection, through the control of autonomous microgrids in Sec. 1.1.2. Sec. 1.1.3 describes possible supporting functions of inverters to frequency and voltage regulation of distribution grids, focusing on the new standard requirements. In Sec. 1.2 and 1.3 some specific risks associated to DG are described: respectively the potential instabilities and the risk of uncontrolled islanded operation both for distribution networks. These two issues together with the autonomous operation of microgrids are the core of this Thesis in the following Chapters.

1.1 Hierarchical organization of future grids

The most admitted and used approach to handle the large penetration of RES in distribution grids nowadays is to cluster DERs and loads forming microgrids, and hierarchically manage them [9, 12, 13]. So a microgrid can be defined as a cluster of DERs and loads, which includes suitable control structures and layers to improve cooperation and integration of the different units. Geographical extension, power level, and voltage level of microgrids can be different, but a microgrid can be operated mainly in two operating modes: the grid-connected or the islanded operating mode [3, 12]. Microgrids can be AC or DC grids and they can be single-phase or three-phase. An example of microgrid is in Fig. 1.3: the microgrid is connected to the main grid at the Point of Common Coupling (PCC) via a breaker and by opening and closing this switch is possible to change the operating mode of the microgrid.

Different types of energy source and several kinds of load make the distribution grid scenario very complex and this aspect is even accentuated by microgrid management algorithms. The reason is that all these devices can potentially act at the same time and with different time scale behaviors. There could be low level controllers for the DG units, high level energy market mechanisms or algorithms that improve the quality of service at intermediate level and many others.

This complexity and the time scale separation suggest a layered architecture, as shown in Fig. 1.4. Starting from the fastest and closest to DER con-

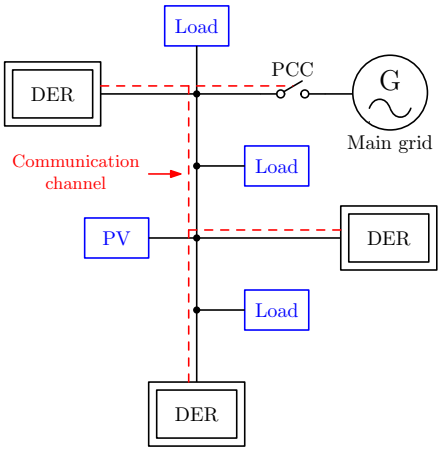

Figure 1.3: Example of microgrid

trollers, it is possible to identify the *zero control* layer. The regulators that belong to this layer are inverter-resident and they are used to control output voltage or current of power converters. Typical requirements for these controllers are high bandwidth and performance in order to guarantee a fast time response under generic operating conditions [10].

Above the zero control there is the *primary control* that takes care of the stability of the microgrid, controlling local variables, such as voltage, frequency, and current injection, and managing the power sharing among the DERs. Primary controllers usually do not require any communication among the power converters of the microgrid [9, 10, 14, 15]. Moreover, these local regulators can implement *droop* control and virtual impedance [10].

Secondary control acts as a centralized controller optimizing other aspects of the microgrid, for example reducing voltage and frequency steady-state errors from the nominal values, improving the power quality and stability, reducing the losses of the grid, and so on. This control layer exploits communications and wide-area monitoring architectures to coordinate the action of all the DERs within a given area. This leads to response times for secondary controllers in the range of minutes, and so slower dynamics compared to the primary control.

Finally, *tertiary control* usually regulates power flows exchanged by the microgrid with the power distribution network. This optimization is usually based on economic reasons and so it has the slowest dynamics.

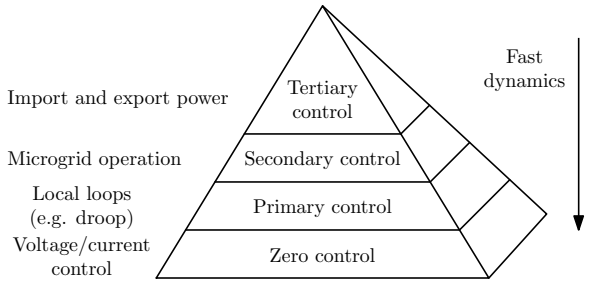

Figure 1.4: A possible layered architecture for the simultaneous execution of different algorithms in a smart microgrid

1.1.1 Zero control

DERs are usually controlled as *grid-feeding* devices for grid-connected operation, i.e. they work as current sources that track particular active and reactive power references [10]. This zero controller allows for example the injection of all the available power that can be provided by the energy source, e.g. PV, wind, etc. This control is implemented with different types of closed-loop current regulators, but ideally these devices can be represented as an ideal current source with an high parallel impedance. A simplified scheme of a grid-feeding power converter is in Fig. 1.5.a, where p_{ref} and q_{ref} are respectively the active and the reactive powers to be generated. Usually, this kind of generator is synchronized to the AC voltage at the connection point, with Phase-Locked Loop (PLL) schemes [10].

On the other hand, *grid-forming* DERs control the output voltage and frequency, tracking the corrisponding references V_{ref} and ω_{ref} with proper control loops: usually an inner current closed-loop regulator and an outer voltage one [10]. They can be represented as an ideal AC voltage generator with a low output impedance, as in Fig. 1.5.b.

Usually *grid-forming* DERs are employed in autonomous or islanded operating mode, with other primary controllers which set their frequency and voltage references. In particular, they are required to take part to the voltage and frequency control since the usual control imposed by the utility grid is missing in this operating mode [10]. This primary control is described in the next section, i.e. *droop control* for intentional islanded operation.

Figure 1.5: a) Grid-feeding and b) grid-forming inverters as in [10]

1.1.2 Primary control for intentional islanded operation

A microgrid can intentionally be operated in autonomous or islanded mode, meaning that it can operate disconnected from the main grid. Focusing on AC microgrids, to allow this operating mode the frequency and the amplitude of the voltage in the microgrid must be managed by DERs to correctly feed all the loads. Furthermore, the required power from the loads has to be shared among all the DERs [3, 12].

A widely investigated technique to manage the parallel operation of DERs in islanded mode and to pursue the goals of frequency and voltage regulation and power sharing is the P/f and Q/V droop control. Droop techniques are attractive in microgrids, because they do not rely on time-critical communication among DERs. For this reason they can be classified as primary controllers. To exploit droop control for intentional islanded mode, DERs are usually controlled as grid-forming devices [3, 9, 10, 16–22].

Power flow equations

The power flow dependencies of an electric line of a distribution system are described in this section in order to understand the basic idea of droop control. Active and reactive powers are described as function of the voltages at the beginning and at the end of the line. In AC microgrids operating in sinusoidal regime with the angular frequency ω_o, the electric lines can be described as a series of a resistance and an inductance, neglecting the parallel conductance and capacitance, as in Fig. 1.6: this approximation can be done for short electric cables [23].

In sinusoidal operation, the phasor representation can be used to describe

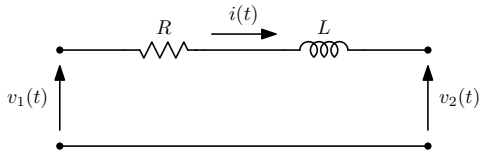

Figure 1.6: Resistive-inductive electric line

the voltages $v_1(t)$ and $v_2(t)$, respectively at the beginning and at the end of the line, and the current $i(t)$ of the cable in Fig. 1.6 [24]. The phasor of the line current results

$$\mathbf{i} = \frac{\mathbf{v}_1 - \mathbf{v}_2}{\mathbf{Z}} = \frac{\mathbf{v}_1 - \mathbf{v}_2}{R + j\omega_o L} \tag{1.1}$$

where the letter in bold indicates the phasor of the respective voltage or current, $\mathbf{Z} \triangleq R + j\omega_o L$ is the complex impedance of the electric line and j is the imaginary unit.

Writing the complex quantities with their absolute value and argument, $\mathbf{v}_1 = V_1 e^{j\varphi_1}$ and $\mathbf{v}_2 = V_2 e^{j\varphi_2}$ and $\mathbf{Z} = Z e^{j\theta}$ with V_1, V_2, $Z \in \mathbb{R}$, the complex power $\mathbf{s}$ that flows at the beginning of the line results

$$\mathbf{s} = p + jq = \frac{1}{2}\,\mathbf{v}_1\,\mathbf{i}^* = \frac{{V_1}^2}{2Z} e^{j\theta} - \frac{V_1 V_2}{2Z} e^{j(\varphi+\theta)} \tag{1.2}$$

where $\varphi \triangleq \varphi_1 - \varphi_2$ and the * operator is the complex conjugation. The $1/2$ factor is due to the peak value representation for phasors and because single-phase connection is considered. Evaluating the real and imaginary parts of $\mathbf{s}$ in (1.2), active p and reactive q powers result:

$$p = \mathfrak{Re}\left[\mathbf{s}\right] = \frac{{V_1}^2}{2Z}\cos\theta - \frac{V_1 V_2}{2Z}\cos\left(\varphi + \theta\right) \tag{1.3a}$$

$$q = \mathfrak{Im}\left[\mathbf{s}\right] = \frac{{V_1}^2}{2Z}\sin\theta - \frac{V_1 V_2}{2Z}\sin\left(\varphi + \theta\right) \tag{1.3b}$$

Some approximations can be introduced in (1.3) depending on the type of the electric line: Tab. 1.1 shows that HV electric lines have an inductive dominant component, while LV cables have a dominant resistive component.

If the inductive component is dominant in the previous analysis (for example for HV lines), it is possible to introduce the approximation $R \simeq 0$, leading to

Line type	R' [Ω/km]	X' [Ω/km]	I_N [A]	R'/X' –
LV	0.642	0.083	142	7.7
MV	0.161	0.190	396	0.85
HV	0.06	0.191	580	0.31

Table 1.1: Typical values of resistance per unit length R', reactance per unit length X', nominal current I_N and R'/X' ratio for different kinds of electric line; data from [25]

$\mathbf{Z} = j\omega_o L = Xe^{j\pi/2}$. Equations (1.3) simplify as:

$$p = \frac{V_1 V_2}{2X} \sin\varphi \tag{1.4a}$$

$$q = \frac{{V_1}^2}{2X} - \frac{V_1 V_2}{2X} \cos\varphi \tag{1.4b}$$

In many practical cases, it is possible to consider $\varphi \simeq 0$ since the impedance of the line is usually small and so $\sin\varphi \simeq \varphi$ and $\cos\varphi \simeq 1$. With these approximations, equations (1.4) become:

$$p \simeq \frac{V_1 V_2}{2X} \varphi \tag{1.5a}$$

$$q \simeq \frac{{V_1}^2}{2X} - \frac{V_1 V_2}{2X} = \frac{V_1}{2X} \Delta V \tag{1.5b}$$

where ΔV is the difference $V_1 - V_2$.

From (1.5a), it follows that the active power depends mostly on the phase shift φ between the voltage waveforms at the beginning and at the end of the line, while from (1.5b) the reactive power depends mostly on the voltage amplitude drop ΔV across the line. From these observations, it results that, for a fixed $\mathbf{v}_2$, the active power flow of the line can be controlled by acting on φ via φ_1 and the reactive power flow can be controlled by acting on ΔV via V_1.

Considering vice versa the case of an electric cable with dominant resistive component, for example an LV line, where $L \simeq 0$ leading to $\mathbf{Z} = Re^{j0} \in \mathbb{R}$. In

this case, equations (1.3) simplify as:

$$p = \frac{{V_1}^2}{2R} - \frac{V_1 V_2}{2R}\cos\varphi \tag{1.6a}$$

$$q = -\frac{V_1 V_2}{2R}\sin\varphi \tag{1.6b}$$

As done before, considering $\varphi \simeq 0$ and so $\sin\varphi \simeq \varphi$ and $\cos\varphi \simeq 1$, equations (1.6) become:

$$p \simeq \frac{{V_1}^2}{2R} - \frac{V_1 V_2}{2R} = \frac{V_1}{2R}\Delta V \tag{1.7a}$$

$$q \simeq -\frac{V_1 V_2}{2R}\varphi \tag{1.7b}$$

Now from (1.7a) the active power depends mostly on the voltage amplitude difference ΔV between the voltage waveforms at the beginning and at the end of the line, and from (1.7b) the reactive power flow depends mostly on their phase shift φ. For a resistive line, for a fixed $\mathbf{v}_2$, thus the line active power can be controlled by acting on ΔV through V_1 and the reactive power can be controlled by acting on φ via φ_1. Comparing these dependencies with those of the inductive line, it is possible to notice that they are inverted, while for a generic resistive-inductive line the active and reactive powers are influenced by φ and ΔV at the same time and so there are coupled dependencies.

Basic droop control

In order to describe the basic droop control, consider a microgrid with inductive electric lines where the active power flow can be controlled by acting on the phase of the voltage and the reactive power flow can be controlled by acting on the voltage amplitude. Based on this idea, P/f and Q/V droop control consists of regulating the output frequency of the inverter as a function of supplied active power (by acting on the frequency, the voltage phase can be regulated) and regulating the output voltage amplitude according to delivered reactive power [18, 19]. Since the steady-state frequency of the network must be unique and constant, droop techniques exploit the frequency as a communi-

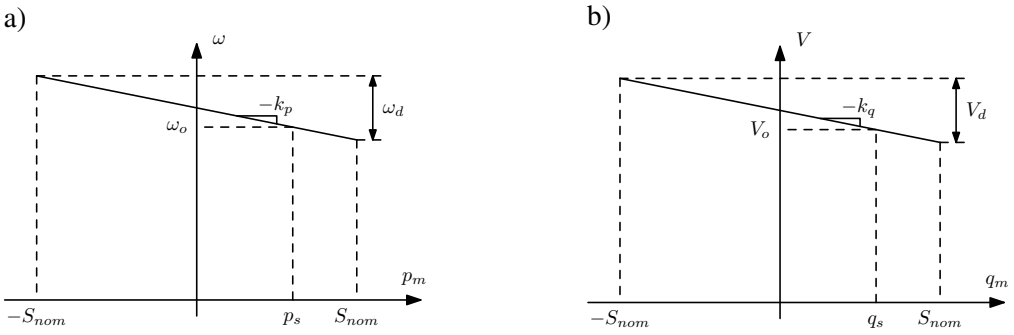

Figure 1.7: Basic droop characteristics: a) P/f droop and b) Q/V droop

cation channel in order to properly share the power among different inverters.

This control has to be applied to a *grid-forming* inverter, whose references are set as:

$$\omega_{ref} = \omega_o - k_p \left(p_m - p_s\right) \tag{1.8a}$$

$$V_{ref} = V_o - k_q \left(q_m - q_s\right) \tag{1.8b}$$

where p_m and q_m are the measured active and reactive powers at inverter output, ω_o and V_o the nominal angular frequency and amplitude of the microgrid voltage, k_p and k_q the *droop coefficients*, and p_s and q_s constant values in conventional droop control. The droop characteristics (1.8) are shown in Fig. 1.7. The droop coefficients, i.e. k_p and k_q, affect the active and reactive power sharing and the system dynamic response in islanded mode [18]. The paper [10] refers to this control scheme as *voltage-source-based grid-supporting* function.

This kind of regulation can stabilize the voltage profile and keep the voltage amplitude and frequency in well-defined ranges [17, 19, 26–28]. Consider for simplicity the P/f loop: equation (1.8a) is shown in Fig. 1.8 for two inverters with different droop characteristics, i.e. with different slopes. In a steady-state operation, the frequency ω_{ss} of the grid must be constant and unique, otherwise the power flows are not constant. So ω_{ss} determines, through the intersections, the two powers p_1 and p_2 generated by the two DERs. By a proper design of the droop coefficients it is possible to regulate the dynamic response of the system and the share of the load demand among the DERs [18]. Since the frequency

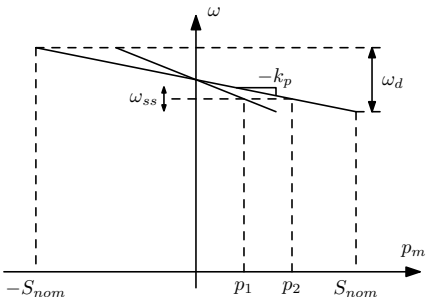

Figure 1.8: Droop characteristics in autonomous operation for two different DERs

ω_{ss} is unique in a steady-state condition, but not the voltage amplitude, this regulation scheme can precisely share the load active power among different inverters, but this precision is not high for reactive power sharing.

The relations (1.8) can be used only for a microgrid with cables dominated by the inductive component. If the cables have strong resistive component, this kind of controller can destabilize the microgrid operation. Different types of droop controllers have been proposed to overcome specific problems of the basic solution described before: for networks with resistive-inductive lines, solutions such as linear transformation in the plane of the powers [29, 30] or virtual output impedance technique [18, 31–33] can be employed. Additional studied improvements are related to the precision of reactive power sharing [31, 34] and the power sharing performances for nonlinear loads [19, 32]. There are other solutions that use more complex regulators in order to separate the characteristics of the steady-state solution to those related to transients [34, 35]. Other papers provide additional services beyond the basic grid operation, helping the voltage support and reactive power compensation [22, 36].

1.1.3 Primary control for grid support

Inverters for DG systems may produce active and reactive power at any level, according to the active power supplied by the primary energy source and according to the rated power of the electronic devices: this allows the DERs to produce any power at any PF [10, 37]. However, some standards for grid-connected operation, as [11], impose the injection of all the available active

power at unity PF and this can create concerns. This injection often is done with a grid-following device.

In such situations, the PF at the PCC can go down on a lagging power system and the injection of reactive power locally from DG inverters would be beneficial for the grid operation, instead requiring it from the PCC [37]. As anticipated at the beginning of this Chapter, there are other advantages from allowing the inverters to regulate their active and reactive powers: they can support the voltage and frequency regulations of the grid, improve the power quality and increse the hosting capacity of the grid [1, 5, 6, 37]. In this section, some voltage and frequency support techniques are described to understand their potentiality and possible issues.

Voltage regulation support

PV generators do not have any rotating parts, unlike conventional generators, and thus they do not have inertia. This can cause some problems when the solar irradiance at the PV panel changes rapidly, for instance due to cloud movements, because also the output power of the inverter changes rapidly. Fast power changes can cause voltage sags or dips and, in these situations, injecting reactive power can help mitigate the voltage variations [38, 39]. Inverters can regulate the voltage together with the conventional devices of a radial distribution system, that are load-tap-changing transformers at substations, line-voltage regulators or switched capacitors on feeders [37].

The local reactive power injection can pursue two different goals: the reduction of the voltage drop along the electric line and the minimization of the distribution losses. However, these two objectives are in competition and a trade-off has to be done [39]. For inductive connection it is possible to regulate the voltage amplitude of the DER node by injecting reactive power, as seen with the power dependencies in Sec. 1.1.2. Secondary level controls provide minimization of the distribution losses, as described in Sec. 1.1.4, however the minimum for the line power losses and the minimum for the voltage amplitude drop are achieved for different values of reactive power injection by the inverter.

One of the simplest voltage support techniques consists of injecting negative

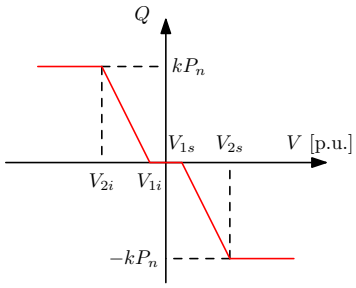

Figure 1.9: Q/V droop characteristic for inverters with rated power larger than $6\,\mathrm{kW}$ according to Italian standard ($k \simeq 0.5$) [7]

reactive power as the local voltage amplitude increases and generating a positive reactive power when it decreases [37, 39]. This technique has already been regulated and imposed by some country level standards, such as for instance the Italian [7] and the German ones, [40] and references therein. Reffering to the Italian standard [7], each PV inverter with rated power larger than $6\,\mathrm{kW}$ has to generate reactive power according to the Q/V droop characteristic shown in Fig. 1.9. Many existing standards require this type of regulation, however many connection rules do not specify any particular requirements on their dynamic response [40]. For example, the standard [7] only provides an upper bound on the transient time for this regulation: it states that the reactive power has to reach the steady-state value within $10\,\mathrm{s}$. Q/V droop control for voltage support has been studied by different works, in order to limit the voltage rise on the feeder and to reduce the voltage fluctuations due to cloud movements [38, 40–45].

Frequency regulation support

The national standards for PV DERs connected to the grid have different fixed cutoff frequencies: if the grid frequency rises above these thresholds, the DERs have to be disconnected. For example, these frequencies for LV grids are $50.3\,\mathrm{Hz}$ in Italy and Denmark and $50.2\,\mathrm{Hz}$ in Germany [5, 7]. In an area with a large penetration of PV DERs, an over-frequency event can cause a sudden loss of a large part of generation capacity. In turn, this can cause severe under-frequencies and even rolling blackouts [5]. This has driven the standards to let the PV units to provide frequency support and smoother responses to frequency

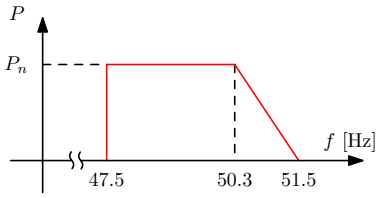

Figure 1.10: P/f droop characteristic for inverter according to Italian standard [7]

transients. Different country level standards now state that the PV DERs have not to disconnect suddenly when the grid frequency increases above the threshold, but they have to reduce the power generation gradually, providing smoother responses. For example, the Italian standard provides the P/f droop curve that is shown in Fig. 1.10 and the German one is similar [5].

Also some papers propose P/f droop characteristics for the PV inverters to support the frequency regulation of the grid: a survey is in [46]. Usually PV systems are operated at the Maximum Power Point (MPP) to generate all the available power and so only a reduction of the injected power is possible, by moving away from the MPP. To obtain a PV inverter fully dispatchable, i.e. with the possibility to increase and decrease the generated power, it has to be operated below the MPP. For example, realizations of such controllers together with the implementation of P/f droop regulation are described in [47, 48] with analyses on how the stability of the grid can be improved after severe transients.

It should be stressed that the P/f and Q/V regulation described in Sec. 1.1.2 and Sec. 1.1.3 have completely different purposes, even if they are both called P/f and Q/V droop. The one of Sec. 1.1.2 applies to a grid-forming device, which measures its output active and reactive powers and, based on the P/f and Q/V droop characteristics, it sets the frequency and the amplitude references for output voltage. This kind of regulation is used in islanded mode, since the DERs have to impose and regulate the voltage and to share the load power among DERs. On the other hand, the P/f and Q/V regulation described in this section applies to grid-following devices, and it is already regulated by some standards for PV connection. So it is used in grid-connected operation, where the frequency and the voltage are strictly imposed by the mains. For this reason, this droop control consists of measuring the output voltage and frequency of the

DER which injects an active and a reactive power determined by these measurements and P/f and Q/V characteristics. The objectives are to exploit the DERs as supporting devices to the frequency and voltage regulations done in the grid. The paper [10] refers to this second control scheme as *current-source-based grid-supporting* function.

1.1.4 Secondary and tertiary control

Local control techniques, which can be classified as primary controllers, can measure and act only on local quantities, without requiring additional communication or coordination infrastructures. This usually makes them more robust, but, on the other hand, local schemes act based on few information and so optimal operation in general could not be achieved.

The secondary control, usually working as centralized or distributed controller, restores the voltage and frequency in the microgrid and compensate for the deviations caused by the primary control. The secondary control can also improve the power quality of the grid, for instance blancing the voltages on the phases and keeping satisfied the voltage constraints at the grid nodes [49]. Other improvements that can be pursued with the secondary controller are the reduction of distribution losses, which is achieved with a communication infrastructure and centralized computation capabilities in [50, 51]. A similar objective is pursued in [52] with a distributed controller, which requires local communication and local knowledge of the network topology and state. The optimization of the network losses and voltage profile are usually achieved regulating the powers injected by DERs [53].

Tertiary control is the higher control level and also the slowest. It considers economical concerns in the optimal operation of the microgrid, and manages the power flow between microgrid and main grid. Tertiary control optimization is usually based on economic criteria, considering the relationship between the demand and the energy supply balance, together with the marginal generation cost of each DER. This optimization relies on short-term load prediction, generation forecast, and energy storage capability estimation, as well as the specific demands set by the transmission and distribution system operators and the prize

signals provided by the electrical market [10].

1.2 Potential instabilities with DG

Power electronics interfaces can help improve the performance, efficiency, and reliability of the interfaced devices, but on the other hand their active control introduces complex and fast dynamics, such as nonlinear and time-varying behaviors, which can worsen the system stability when several devices interact. This has driven the study and the analysis of such systems as a whole, considering the important interactions among different interconnected units, rather than limiting the analysis to the single device stability [54, 55].

Nowadays, powerful computation capabilities allow to simulate very complex and extended scenarios. These capabilities have pushed different works to address instability concerns in the distribution grid through detailed simulations. Several papers propose simulation analyzes of distribution grids, both for islanded operation and grid-connected operation [56].

Grid-connected operation has been considered in [57], which studies the impacts of DERs that are interfaced to the distribution grid via rotating generators and inverters. Oscillations appear depending on the interface device and the DG penetration level. Inverter-interfaced DG can lead to a reduction of stability, which is mainly due to the reduction of the total inertia, caused by the substitution of rotating generators with inverter interfaced generators [58]. Simulation details can be very precise and sophisticated, considering a transmission grid with PV DERs interfaced by inverters, also the effects of Maximum Power Point Tracking (MPPT) algorithms can be accounted [59]. Some example results for a transmission grid with traditional synchronous generators and inverter interfaced PV generators are in Fig. 1.11, where the frequency and the voltage deviations at one node of the grid increase as the DG penetration increases [56].

These results show that instabilities could arise in the interconnected grid if each DER is only designed as a stable standalone device: component-wise stability does not ensure stability of the system as a whole [60]. This marks the

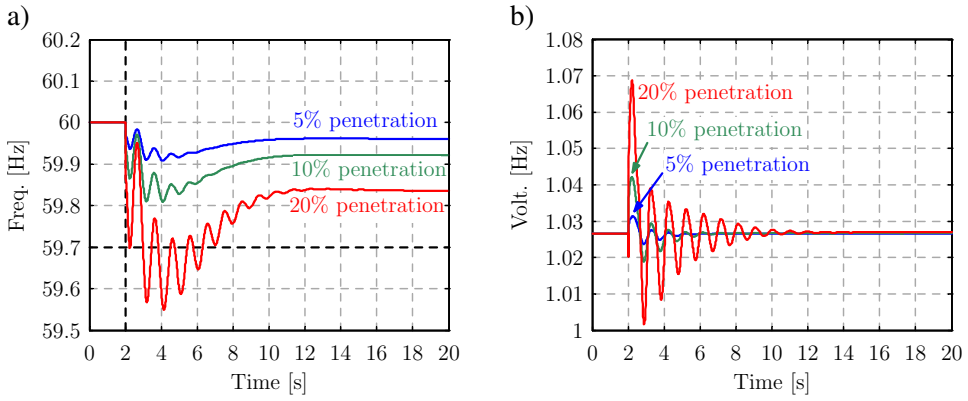

Figure 1.11: Simulation results: a) the frequency and b) the voltage transients when a PV plant is disconnected; different results for different DG penetration levels [59]

importance of studying the dynamic characteristics of a grid instead of focusing on a single device, in particular when DER units are more and more numerous.

To study the stability of complex systems there are two main approaches: one that is simulation-based and another based on analytic models. While simulation is quite direct and straightforward to address very complex scenarios, even with Real-Time (RT) simulators [61, 62], analytic approaches can provide more details and insights on the instability causes of the system. Analytic approaches that account for large system usually introduce approximations [15, 56], while others keep a detailed description, for instance addressing the stability of the interactions of two interconnected subsystems.

Considering the stability analysis approaches that address the interaction of two equivalent subsystems, that are *source* and *load*, a standard technique is the impedance-based approach. This method is interesting also because it enables an experimental based procedure to obtain the mathematical model. The first example of these analyses is provided by Middlebrook in [63], who addresses the interactions of DC systems, in particular between DC-DC converters and their input filters. This kind of system is usually time-varying, due to the switching behavior of power electronics, and nonlinear, for example because of cross-product terms (e.g. with the duty-cycle). The approach in [63] bases on averaging methods at switching period to eliminate the time-varying behavior and on linearization approaches to obtain small-signal models. The

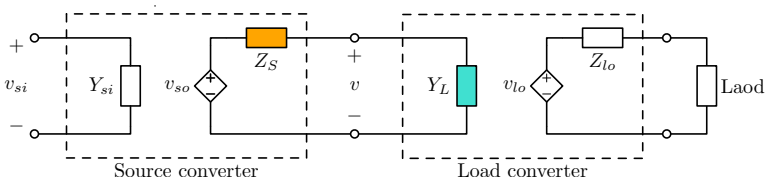

Figure 1.12: Schematic representation of the DC-DC source-load system

resulting models, one for the source and one for the load, can be described by their input and output impedances and the system stability can be addressed by the Nyquist stability criterion applied to the ratio of the impedances (Fig. 1.12) [54, 63, 64].

Impedance-based analysis is not directly applicable to AC systems, as traditionally microgrids and in particular distribution grids are, because of their sinusoidal behavior. Time-varying and nonlinear characteristics due to the switches can be addressed again via averaged-modeling at the switching frequency of the power converters. However, the resulting averaged model can be still time-varying and nonlinear: time-varying can be due to the sinusoidal inputs of AC grids and nonlinearity can be due to the controllers (e.g. cross-product terms). These nonlinearities can not be removed immediately with standard linearization processes because a well-defined operating point can not be easily identified (almost all quantities have periodically time-varying trajectories). The paper [54] provides a survey of small-signal methods for AC power systems.

Small-signal stability in three-phase AC systems has been studied in terms of source and load impedances (Fig. 1.13) exploiting the dq or *Park transformation* [55, 65]. First, consider the transformation rule from the abc phase components to the stationary reference frame $\alpha\beta$:

$$\mathbf{x}_{\alpha\beta}(t) = \frac{2}{3}\left[x_a(t) + x_b(t)\, e^{j\frac{2}{3}\pi} + x_c(t)\, e^{j\frac{4}{3}\pi}\right] \tag{1.9}$$

for a set of three-phase quantities $x_a(t)$, $x_b(t)$ and $x_c(t)$ and the following relation to obtain the space vector in the dq rotating reference frame, i.e. Park transformation:

$$\mathbf{x}_{dq}(t) = x_d(t) + jx_q(t) = \mathbf{x}_{\alpha\beta}(t)\, e^{-j\omega_o t} \tag{1.10}$$

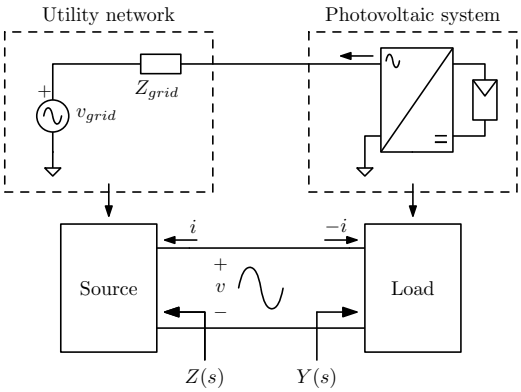

Figure 1.13: Schematic representation of the source-load system for an AC system

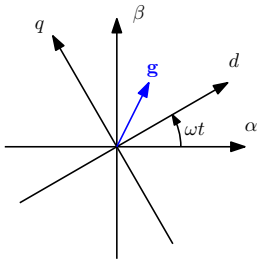

Figure 1.14: dq transformation at ωt

where the transformation is performed at the nominal line frequency ω_o of the grid. The transformation is shown in Fig. 1.14. If the three-phase system (3-wire or 4-wire) has no negative-sequence and it has constant zero-sequence with low harmonic distortion, each voltage and current of the system in the dq reference frame, that is with (1.10), is constant [55, 65]. Thus, this approach allows to identify a steady-state operation and a small-signal analysis can be performed in terms of dq space vectors: each voltage and current is described by two variables, namely d and q components, and so at a two-terminal electric interface four impedances in the dq frame can be identified (combining two currents and two voltages) [55].

A similar approach to [63] can be still applied to the resulting small-signal model of the balanced three-phase system considering the Generalized Nyquist stability Criterion (GNC) for Multiple-Input Multiple-Output (MIMO) systems [66]. As example, the dq impedances of a three-phase voltage source converter synchronized with a PLL are analytically derived and the stability is studied

with eigenvalue analyzes in [67]. An alternative to the dq transformation comes from [68], that addresses the sinusoidal time-varying behavior of three-phase AC systems via the harmonic linearization approach, introducing some approximations.

Balanced and symmetric three-phase AC power systems have been studied and analyzed and well-established techniques for their stability analysis exist. On the other side, single-phase AC system studies are more difficult because the identification of a precise operating point where to perform a linearization is not straightforward: for instance the dq transformation is not easily defined for them. For this reason, different points on the single-phase AC stability analysis are still open and they are beckoning the interests of the research community. These studies are interesting because they allow to address stability issues in LV microgrids, that usually include single-phase connected DERs, and other applications as in the railway system [69].

1.3 Unintentional islanded operation

New European standards state the reference technical rules for the connection of active users to the grid and for their behavior during temporary voltage and frequency variations [70–72]. These standards together with some country-level ones are imposing the participation of DERs to the voltage and frequency regulation, through the P/f and Q/V droop characteristics (Sec. 1.1.3). One of the most relevant modifications is the extension of the frequency range that is allowed during normal operation of DERs from the traditional thresholds $49.7\,\mathrm{Hz}$ and $50.3\,\mathrm{Hz}$ to the less stringent values $47.5\,\mathrm{Hz}$ and $51.5\,\mathrm{Hz}$, and the extension of the voltage levels to the range $\pm 15\%$ of the rated voltage [7, 73]. Transient and steady-state voltage and frequency allowed ranges are depicted in Fig. 1.15 for the Italian standard [7].

The power electronic interfaces introduce fast dynamics into the grid and could continue to energize a portion of the electric network also when the main grid disconnects, even if the islanded mode is not explicitly pursued and implemented. Thus, undesired islanded portions of the grid can be still oper-

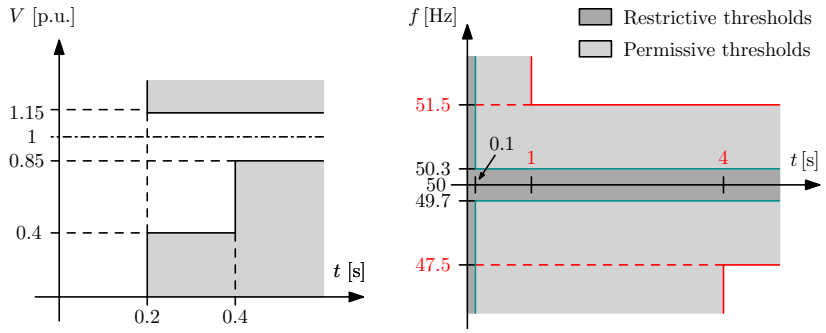

Figure 1.15: Voltage and frequency thresholds imposed by the Italian standard [7, 74]

ating [75, 76], even if currently the distribution grid is not designed for such operation: this operation is called *unintentional* or *uncontrolled* islanded operation [73]. Unintentional islands can make damages on the electric equipment of the grid when these parts of the grid have to be reconnected to the mains, since auto-reclosing switches and rotating generators/loads may not be designed to sustain such transient conditions [75, 77].

Different anti-islanding techniques have been proposed so far and implemented in the interface inverters for DG applications. Anti-islanding schemes are usually divided in passive, active, hybrid, and communication-based approaches [78–84]. Passive techniques consist of measuring a certain system parameter, such as frequency or voltage, and comparing it with a predetermined threshold. The islanding detection happens if this parameter is out of this predetermined range. In active methods, the control of the inverter tries to drift some parameters, such as frequency or voltage, or to inject disturbances, as negative sequence components, in order to move the system parameters far from the nominal ones or to destabilize the system itself when the islanding happens. Communication-based methods send and receive signals between different devices in order to detect the transition. Active methods are quite attractive because they are less expensive compared to communication-based approaches and they are more effective compared to passive methods. Recently, hybrid passive-active methods can combine advantages of both approaches [85].

Performance evaluation of anti-islanding schemes are usually based on two characteristics [76, 86]:

- speed of detection, which is the time interval between the actual islanding instant and the islanding detection instant
- Non-Detection Zone (NDZ), which is a region specified by the system parameters, in which islanding detection fails

Standard [87] suggests the use of a parallel RLC load with a resonance frequency equal to the line frequency to test the anti-islanding technique effectiveness, because it can provide higher stabilization of the islanded system. Some interesting studies on the determination of NDZ can be found in [82,85,88,89].

However, when there is a large number of DERs, the behavior of all these provisions, being different from each manufacturer and not specified by standards, is unpredictable and in some cases these techniques can lack to detect the operating mode and so the disconnection of the inverter may not happen [90]. Moreover, in some countries such anti-islanding provisions are not mandatory on MV connections.

In order to address the unintentional islanding issue, the problem can be separated in two sub-problems: the *permanent* and *temporary* unintentional islanded operations. The risk of permanent islanding operation is the risk of a steady-state Unintentional Islanded Operation (UIO). With other words, permanent islanding means that the steady-state frequency and voltage of the islanded system remain within the allowed thresholds, for instance those in Fig. 1.15. In particular to maintain this operation, the stability of the islanded system is required [8,73].

The UIO may be dangerous especially in presence of *automatic reclosing procedure*. This automatic procedure is adopted in some distribution networks of European countries and has the purpose of a fast localization and separation of the faulted line segment of an MV distribution network [7,91]. It consists of opening and reclosing the breaker of an MV line for established time intervals in order to extinguish faults, for instance single phase to earth faults. This procedure can introduce additional risks for the equipment when UIO happens, because of possible out of phase reconnections. In Fig. 1.16 there is an illustration of the automatic reclosing procedure for the Italian distribution network [91]: observe that the first opening of the breaker lasts for $600\,\mathrm{ms}$.

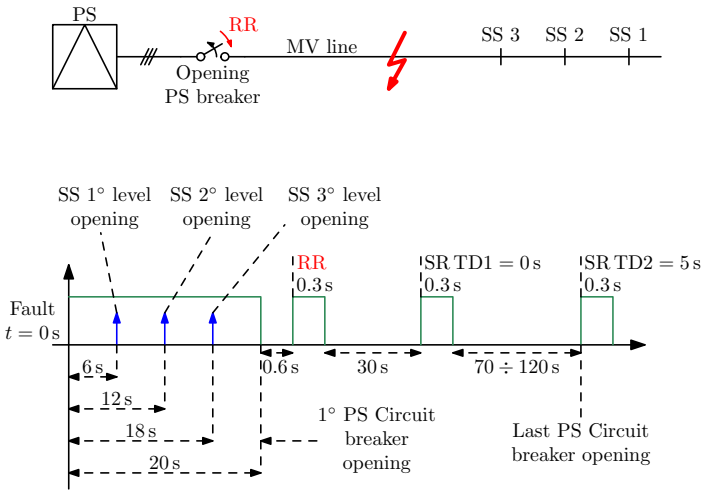

Figure 1.16: Automatic reclosing procedure for fault extinguishing [91]

To address the automatic reclosing procedure issue, the temporary islanding problem has to be considered, as the operation in islanded condition for a short time interval after the disconnection [73]. The study of this problem consists of to understand if the disconnecting transient, i.e. the voltage and the frequency transients, fulfills the thresholds defined by the standards, e.g. those of Fig. 1.15. The considered time interval should be those of the automatic procedure, e.g. 600 ms.

The risk of unintentional islanding should be studied in detail and properly reduced in a distribution grid scenario with more and more DERs. Furthermore, the impact of new standards for DER connection should be evaluated in relation to the unintentional islanding risk, in particular considering the effect of the introduction of P/f and Q/V droop characteristics, which *may* stabilize the islanded operation leading to an increase of this risk [7, 70–72].

1.4 Summary

This Chapter shows that distribution grid scenario is very complex and varied, because of the presence of different devices that work simultaneously and with different aims and time scale characteristics. The fast dynamics introduced by power electronics converters can be from one point of view beneficial, im-

proving the performances of the grid or providing new functionalities and operations, as for instance intentional islanded operation. On the other side, power electronics converters may introduce concerns and issues if they are not properly controlled. In this Chapter, attentions are payed to UIO and instability risks due to the interconnections of several devices in the distribution grids.

These main topics are tackled in the remainder of this Thesis: in particular Chapter 2 focuses on unintentional islanding risk considering the effect of P/f and Q/V droop control stated by new standards for PV connection, Chapter 3 proposes and analyzes a local controller for DERs to operate a microgrid in both grid-connected and islanded operating modes and during the transition, avoiding the use of time-critical communication, Chapter 4 describes and validates an experimental method to address the stability of the interactions between devices in single-phase AC distribution grids or microgrids, and Chapter 5 proposes an automatable and scalable approach to study the dynamics and the stability of distribution grids of generic size. Finally, Chapter 6 outlines the conclusions of this Thesis.

Chapter 2

Risk of unintentional islanded operation

The risk of UIO in distribution grids is of increasing interest because of the large penetration of RES and the new requirements for PV connections, as anticipated in Sec. 1.3. DER anti-islanding protections, if present, may fail to detect the grid transition and so UIO may appear, increasing the hazards for the electric network operation and for the grid equipment. For these reasons, in this Chapter the increasing risk of UIO is analyzed, in particular in presence of DER support functions with P/f and Q/V droop (Sec. 1.1.3).

To analyze the UIO, this Chapter defines the unintentional islanding problems, permanent and temporary, in Sec. 2.1. Then, in Sec. 2.2 the permanent islanding issue is first considered from a static point of view in terms of intersection of the generation and load characteristics, to understand the possible steady-state operation of the islanded system. A small-signal dynamic model for stability analysis is hence presented in order to understand if a permanent islanding is really likely to happen in Sec. 2.3. The quantification of unintentional islanding risk is given in terms of NDZ.

The temporary islanded operation (e.g. below $600\,\mathrm{ms}$) due to the automatic reclosing procedure is then considered in Sec. 2.4. A small-signal model of the islanded system is first proposed to check if the frequency and voltage transients fulfill the standard thresholds. The effects of P/f and Q/V droop characteristics

of generators and their response times are accounted, showing that the risk of unintentional islanding increases introducing droop regulation, in Sec. 2.5. Furthermore, non-simultaneous P/f and Q/V droop regulation is investigated and a control method for inverters based on it is described and validated in order to reduce this unintentional islanding risk: this algorithm and its validation are in Sec. 2.5.

2.1 System description and area of uncontrolled islanding

The scenario considered in this Chapter consists of an LV inverter connected to the main grid at the PCC and having in parallel some local loads, as proposed in [8,73]. In Fig. 2.1, there is a representation of such scenario for a three-phase connection, but similar conclusions can also be done for the single-phase case. The grid-feeding inverter is equipped with internal current/voltage feedbacks and PLL to ensure the desired generation of active and reactive powers. As anticipated in Sec. 1.1.1, grid-feeding inverters are the mostly used for grid-connected operation, and this test-case represents the normal configuration used in PV systems.

Regarding the generated power references $p_{G,ref}$ and $q_{G,ref}$, four Cases are considered [74]:

- *Case I* of a DER with constant active and reactive power references;
- *Case II* of a DER with only Q/V droop characteristic as in Fig. 2.2;
- *Case III* of a DER with only P/f droop characteristic as in Fig. 2.2;
- *Case IV* of a DER with both Q/V and P/f droop characteristics as in Fig. 2.2.

Later, the Chapter shows that the risk of islanding increases for the last three Cases (II-IV) compared to Case I: while in Case I the UIO can be formed due to the regulation characteristics of the load, i.e. the dependencies of the active and reactive load powers to the frequency and the amplitude of the voltage; in the

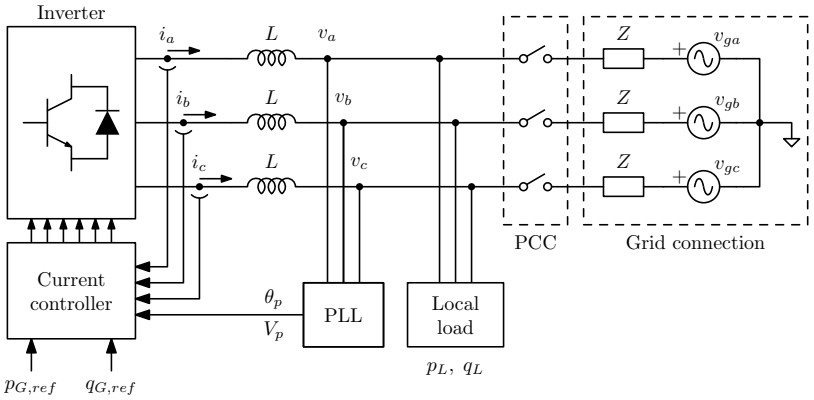

Figure 2.1: Considered scenario (θ_p is the PLL phase in abc domain)

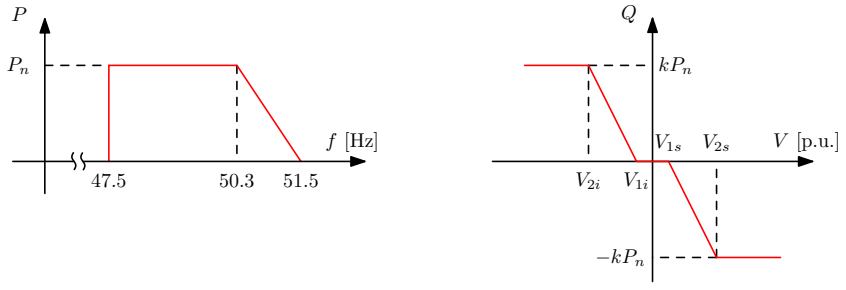

Figure 2.2: P/f and Q/V droop control of the generator as in [7] where k is a constant factor (here $k = 0.4$)

other cases the risk is increased due to the droop characteristics of the inverter-interfaced generator, as described for several papers dealing with P/f and Q/V droop (Sec. 1.1.2).

After the transition from grid-connected to islanded operation, the active and reactive powers p_G and q_G generated by the inverter have to balance those absorbed by the load p_L and q_L, i.e.

$$\begin{cases} p_L(f,\, V) &= p_G(f) \\ q_L(f,\, V) &= q_G(V) \end{cases} \tag{2.1}$$

where it is assumed that the load is described with its active p_L and reactive q_L powers as function of the frequency f and the voltage amplitude V, as some papers on load modeling have done so far [92]. In (2.1) the generator active power p_G is a function of the frequency f and the generator reactive power q_G is a function of the voltage amplitude V, in order to consider the droop characteristics (Fig. 2.2). Notice that this choice is general and it can be done also for the case of an inverter with constant power references. After the disconnection and the power balancing, a new steady-state solution $(f_{ss},\, V_{ss})$ for the system (2.1) can potentially be reached: this is denoted as *static analysis* [8, 73]. If f_{ss} and V_{ss} do not trigger the DER protections, for instance those in Fig. 1.15, then an unintentional islanding is possible. Here the permissive allowed rages of [7] are considered, as shown in Fig. 1.15, and they are

$$\begin{array}{rcccl} V & \in & [\, V_{min},\, V_{max}\,] & = & [\, 0.85,\, 1.15\,] \text{ p.u.} \\ f & \in & [\, f_{min},\, f_{max}\,] & = & [\, 47.5,\, 51.5\,] \text{ Hz} \end{array} \tag{2.2}$$

Taking into account the variability of the power source and the load components in terms of grid-connected active and reactive powers, a *set* of solutions is found that defines the NDZ, i.e. an *area* representing the power mismatch $\Delta P \triangleq p_G\,(f_o) - p_L\,(f_o,\, V_o)$ versus $\Delta Q \triangleq q_G\,(V_o) - q_L\,(f_o,\, V_o)$ at the PCC where the islanding condition is possible, where f_o and V_o are respectively the nominal frequency and nominal voltage amplitude. If for a certain $(\Delta P,\, \Delta Q)$

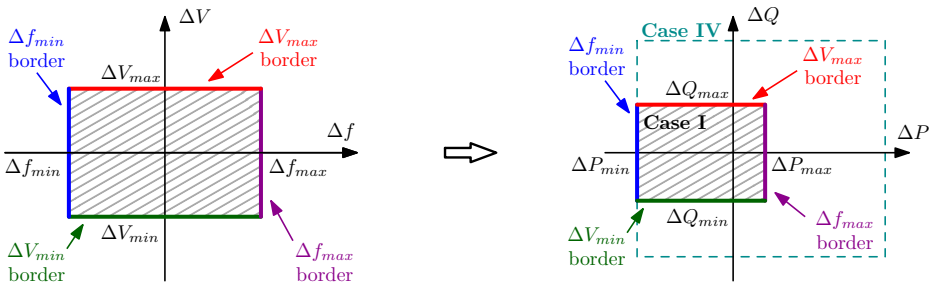

Figure 2.3: Mapping of the Δf_{max}, Δf_{min}, ΔV_{max}, and ΔV_{min} borders from $\Delta f - \Delta V$ plane to $\Delta P - \Delta Q$ plane [74]

the corresponding steady-state solution $(f_{ss},\, V_{ss})$ is within the voltage and frequency thresholds *and* if such operating point is stable, then a *permanent* islanded operation can be maintained, i.e. $(\Delta P,\, \Delta Q)$ belongs to the NDZ.

The frequency and voltage thresholds of (2.2) identify a rectangular area on the plane of allowed deviation of voltage amplitude $\Delta V \triangleq V - V_o$ versus deviation of frequency $\Delta f \triangleq f - f_o$. The borders of this region

$$\Delta V_{min} \triangleq V_{min} - V_o \tag{2.3a}$$
$$\Delta V_{max} \triangleq V_{max} - V_o \tag{2.3b}$$
$$\Delta f_{min} \triangleq f_{min} - f_o \tag{2.3c}$$
$$\Delta f_{max} \triangleq f_{max} - f_o \tag{2.3d}$$

are mapped from the $\Delta f - \Delta V$ plane to the $\Delta P - \Delta Q$ plane. In this reference frame, other four borders are identified and thus the NDZ of unintentional islanding, as shown schematically in Fig. 2.3. In this figure, it is anticipated that the area widens passing from Case I to Case IV: this is described in detail hereafter.

The *temporary* islanding problem is introduced as the problem of stating if the voltage V and frequency f of the islanded system fulfill the standard thresholds for a precise time interval or transient after the grid transition [93]. The regulation of the active and reactive powers of the generator according to P/f and Q/V droop curves (Case IV) increases the NDZ in the plane $\Delta P - \Delta Q$ with respect to Case I for the permanent islanded operation, as shown later. Thus,

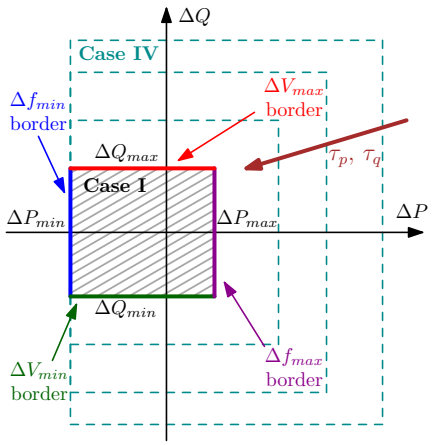

Figure 2.4: Qualitative example of NDZ extension in the plane $\Delta P - \Delta Q$ due to the P/f and Q/V droop characteristics, depending on the embedded inverter power control scheme [93]

in Fig. 2.3 the border of the NDZ of Case IV is wider than the NDZ of Case I. However, for temporary islanding the voltage and frequency need to be within the thresholds within an established time, and so the response times of the P/f and Q/V droop regulation (respectively τ_p and τ_q) play a relevant role on the $\Delta P - \Delta Q$ region shaping: potentially the larger the time constants, the smaller the NDZ, as in Fig. 2.4. Observe that considering the temporary islanded operation during the automatic reclosing time, only the voltage protection may trip within the intervention time, set to $600\,\mathrm{ms}$ (see Fig. 1.15).

2.2 Permanent unintentional islanded operation

This section describes an analytic approach to derive the static $\Delta P - \Delta Q$ region, as presented in [74]. Considering a fixed load, that is fixed power dependencies $p_L(f,\, u)$ and $q_L(f,\, u)$, to draw the NDZ regions (for each different Case) the following procedure can be used:

1. the load powers $p_{L,ss}$ and $q_{L,ss}$ is evaluated for a precise point $(f_{ss},\, V_{ss})$ on the $\Delta f - \Delta V$ border (for the potential islanded solution);
2. in islanded operation $p_{L,ss}$ and $q_{L,ss}$ must be equal to the inverter active and reactive powers, $p_{G,ss}$ and $q_{G,ss}$, for $(f_{ss},\, V_{ss})$, thus knowing the particular Case and the droop characteristics of the inverter, the active and

Table 2.1: Load parameters: base power is the active load power at $(f_o,\, V_o)$

R_1	=	$17\,\Omega$	=	$0.873\,\text{p.u.}$
R_2	=	$82.5\,\Omega$	=	$0.180\,\text{p.u.}$
L_1	=	$87.5\,\text{mH}$	=	$0.551\,\text{p.u.}$
C_1	=	$14.4\,\mu\text{F}$	=	$0.067\,\text{p.u.}$
C_2	=	$60\,\mu\text{F}$	=	$0.280\,\text{p.u.}$

reactive powers $p_G\,(f_o)$ and $q_G\,(V_o)$ in grid-connected mode can be calculated;

3. the $(\Delta P,\, \Delta Q)$ point on the NDZ border (Fig. 2.3) is derived from the grid-connected powers of the inverter and of the load, $p_L\,(f_o,\, V_o)$ and $q_L\,(f_o,\, V_o)$, which are known;
4. the previous points 1-3 are the repeated for all the border in the $\Delta f - \Delta V$ plane of Fig. 2.3.

In this analysis, the grid-connected operating point is $(f_o,\, V_o)$ regardless the power absorbed or generated by the main grid, meaning that the small voltage drop due to the output impedance of the grid is neglected. This approximation is verified in Sec. 2.5.2.

This analysis is general and it can be applied for a generic local load whose active and reactive power dependencies are known, $p_L(f,\, V)$ and $q_L(f,\, V)$. For instance, it can be used with standard modeling choices of load, such as residential, agricultural, and industrial of [92]. However, in the first part of analysis and validation, a local load consisting of a set of passive components is considered: it is a parallel connection of a resistor R_1, an inductor L_1, a capacitor C_1, and a resistive-capacitive series (R_2 and C_2), whose values are in Tab. 2.1 and whose power dependencies $p_L\,(f,\, V)$ and $q_L\,(f,\, V)$ are shown in Fig. 2.5. This choice is done for sake of experimental validation and of simplicity: the power dependency $p_L(f,\, V)$ has in particular a positive slope with respect to the frequency that prevents multiple intersections with the P/f droop curve, and so it prevents multiple steady-state operations within the allowed thresholds.

For such load the NDZs, evaluated with the method described at the begin-

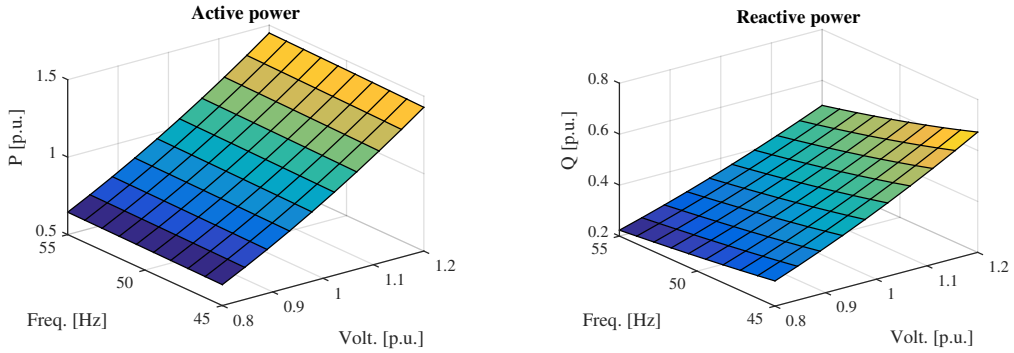

Figure 2.5: Active p_L and reactive q_L powers of the load as function of frequency f and voltage V: powers are normalized to the active power of the load at nominal frequency f_o and nominal voltage V_o [74]

Table 2.2: Areas of NDZ: values are normalized to the area of Case I [74]

Case I	1
Case II	1.16
Case III	8.41
Case IV	45.9

ning of this section, are reported in Fig. 2.6: Fig. 2.6.a refers to the Case I. Fig. 2.6.b shows that including the Q/V droop control (Case II) causes a slight widening of the unintentional islanding region, while the introduction of only the P/f droop control (Case III) leads to a larger area widening (Fig. 2.6.c). Finally, in Fig. 2.6.d for Case IV, the islanding risk is maximum since the region is the largest. Notice that introducing the P/f droop causes a potential unbounded area; however in a real application this area is limited by the rated power of the inverter. To quantify the area enlargement, the areas of the regions of Fig. 2.6 limited to the axis ranges $\Delta P \in [-0.5,\ 1]$ p.u. and $\Delta Q \in [-0.8,\ 0.8]$ p.u., are evaluated and reported in Tab. 2.2.

The regions of this section refer only to the static analysis of the system (2.1), i.e. a *possible* steady-state solution, while to obtain a real permanent islanded operation also the stability of the islanded system is necessary [8]. So in order to complete the analysis of this section, in Sec. 2.3 a small-signal stability analysis is described. Later, in Sec. 2.5.2 the NDZs are drawn experimentally

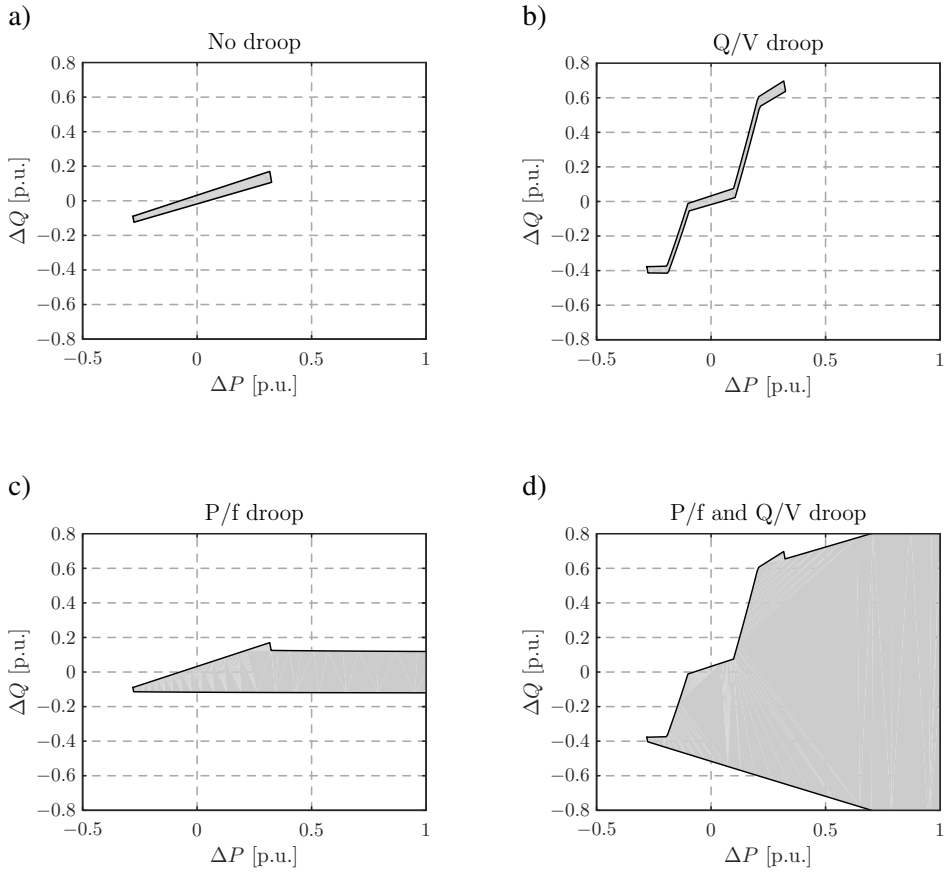

Figure 2.6: $\Delta P - \Delta Q$ area of *possible* permanent unintentional islanding when the inverter operates with droop characteristics according to [7]: a) no droop, b) only Q/V droop, c) only P/f droop, and d) both Q/V and P/f droop [74]

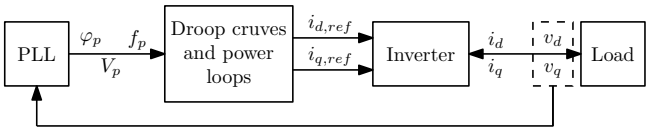

Figure 2.7: Schematic representation for the mathematical model [8]

to validate the results of this section and the stability of the islanded system is also investigated with experiments.

2.3 Small-signal stability analysis for permanent islanding

In order to analyze if the operating point in the NDZ is stable, a simple small-signal model of the islanded system in Fig. 2.1 is derived in this section, extending [8]. This system is divided into two main parts: one for the PV inverter and its PLL and another for the load, both represented in the dq synchronous reference frame at the nominal line angular frequency $\omega_o = 2\pi f_o$ (Sec. 1.2). In this representation, $\mathbf{v} = v_d + jv_q = Ve^{j\varphi_v} \in \mathbb{C}$ refers to the space vector of the inverter output voltage, equal to the load voltage. Term $\mathbf{v}_p = V_p e^{j\varphi_p} \in \mathbb{C}$ indicates the voltage generated by the PLL, and $\mathbf{i} = i_d + ji_q = Ie^{j\varphi_i} \in \mathbb{C}$ is the output current of the inverter, which is equal to the absorbed load current.

Fig. 2.7 shows a block diagram representation of the mathematical model, where the contribution of the PLL is highlighted. The PLL synchronizes the current controlled inverter to the voltage waveform, generating the amplitude V_p, the frequency f_p, and the phase φ_p of the inverter voltage, where the p subscript indicates that these quantities are generated by the PLL and used to evaluate the current reference for the inverter. In the following two subsections, the two models are analytically derived.

2.3.1 Small-signal model of the inverter

The system is usually dominated by different time-scale dynamics: the faster dynamics that are related to the current regulator of the inverter and the slower ones that are related to the PLL (that usually has a much lower closed-loop bandwidth [94]) and to the load. In this scenario, the following stability analysis focuses on the interactions between the slower dynamics, considering the current regulator in steady-state conditions (i.e. the inverter output current equal to the corresponding reference value $\mathbf{i}_{ref} \simeq \mathbf{i}$). Moreover, the dynamics of the active and reactive power loops, if present, are here neglected.

A power controlled inverter with a reference signal $\mathbf{s}_{G,ref}$ is considered:

$$\mathbf{s}_{G,ref} = p_{G,ref} + jq_{G,ref} = \frac{3}{2}\,\mathbf{v}_p\,\mathbf{i}^*_{ref} = \frac{3}{2}\,\mathbf{v}_p\,\mathbf{i}^* \tag{2.4}$$

where the $3/2$ factor derives from the scaling used in the dq transformation. Notice that in (2.4), the voltage $\mathbf{v}_p$ is generated by the PLL. Dividing (2.4) in its real and imaginary parts, it follows:

$$p_{G,ref} = \frac{3}{2}\,V_p\,I\cos\left(\varphi_p - \varphi_i\right) \tag{2.5a}$$

$$q_{G,ref} = \frac{3}{2}\,V_p\,I\sin\left(\varphi_p - \varphi_i\right) \tag{2.5b}$$

In order to include also the more general case of Fig. 2.2, the following expressions for the power references are considered:

$$p_{G,ref} = P_{G0} - k_p f_p \tag{2.6a}$$

$$q_{G,ref} = Q_{G0} - k_q V_p \tag{2.6b}$$

This is a linear approximation of the P/f and Q/V droop functions of Fig. 2.2 that can address all the four Cases described in Sec. 2.1 in a small-signal description: for instance Case I is achieved by setting k_p and k_q equal to zero.

Substituting (2.6) in (2.5), evaluating I and φ_i, and then linearizing the

resulting expressions, it results:

$$\Delta\varphi_i = \Delta\varphi_p + \left.\frac{\partial\varphi_i}{\partial f_p}\right|_Q \Delta f_p + \left.\frac{\partial\varphi_i}{\partial V_p}\right|_Q \Delta V_p \tag{2.7a}$$

$$\Delta I = \left.\frac{\partial I}{\partial f_p}\right|_Q \Delta f_p + \left.\frac{\partial I}{\partial V_p}\right|_Q \Delta V_p \tag{2.7b}$$

where the symbol Δ indicates a small-signal perturbation around the operating point Q. The details of the partial derivatives in (2.7) are not reported here explicitly.

As far as the PLL is concerned, a Synchronous-Reference-Frame PLL (SRF-PLL) is considered [20, 94, 95] and, just for the sake of explanation, here approximated as a first-order model, i.e.:

$$\frac{\Phi_p(s)}{\Phi_v(s)} \simeq \frac{1}{1+\frac{s}{\omega_c}} \tag{2.8}$$

where $\Phi_p(s)$ and $\Phi_v(s)$ are respectively the Laplace transform $\mathfrak{L}$ of $\Delta\varphi_p$ and $\Delta\varphi_v$, ω_c is the closed-loop bandwidth of the SRF-PLL, and s is the complex variable of the Laplace transform. Equation (2.8) is also derived in the time-domain, considering that the time derivative of $\Delta\varphi_p$ is equal to $2\pi\Delta f_p$, i.e.:

$$\frac{\mathrm{d}}{\mathrm{d}t}\Delta\varphi_p = -\omega_c\Delta\varphi_p + \omega_c\Delta\varphi_v \quad \Rightarrow \quad \Delta f_p = -\frac{\omega_c}{2\pi}\Delta\varphi_p + \frac{\omega_c}{2\pi}\Delta\varphi_v \tag{2.9}$$

A more precise PLL model can be easily included in this analysis, if needed.

Respect to the voltage amplitude, in the small-signal model for the PLL, it is assumed:

$$\Delta V_p = \Delta V \tag{2.10}$$

although different implementations on the PLL amplitude control exist. From (2.7), (2.9) and (2.10), the state-space model of the inverter and its PLL can be written as:

$$\begin{cases} \dfrac{\mathrm{d}}{\mathrm{d}t}\Delta\varphi_p &= A_i\Delta\varphi_p + B_i\Delta g \\ \Delta y &= C_i\Delta\varphi_p + D_i\Delta g \end{cases} \tag{2.11}$$

where $\Delta\varphi_p$ is the state of the model, $\Delta g \triangleq [\,\Delta\varphi_v \;\; \Delta V\,]^T \in \mathbb{R}^{2\times 1}$ is its input and $\Delta y \triangleq [\,\Delta\varphi_i \;\; \Delta I\,]^T \in \mathbb{R}^{2\times 1}$ is its output. The four matrices of (2.11) result:

$$A_i = -\omega_c \in \mathbb{R}^{1\times 1} \qquad B_i = \begin{bmatrix}\omega_c & 0\end{bmatrix} \in \mathbb{R}^{1\times 2} \tag{2.12a}$$

$$C_i = \begin{bmatrix} 1 - \frac{\omega_c}{2\pi}\frac{\partial\varphi_i}{\partial f_p}\Big|_Q \\ -\frac{\omega_c}{2\pi}\frac{\partial I}{\partial f_p}\Big|_Q \end{bmatrix} \in \mathbb{R}^{2\times 1} \qquad D_i = \begin{bmatrix} \frac{\omega_c}{2\pi}\frac{\partial\varphi_i}{\partial f_p}\Big|_Q & \frac{\partial\varphi_i}{\partial V_p}\Big|_Q \\ \frac{\omega_c}{2\pi}\frac{\partial I}{\partial f_p}\Big|_Q & \frac{\partial I}{\partial V_p}\Big|_Q \end{bmatrix} \in \mathbb{R}^{2\times 2} \tag{2.12b}$$

2.3.2 Small-signal model of the load

The analysis of this section consider a generic local load whose active and reactive power dependencies are known, $p_L(f,\, V)$ and $q_L(f,\, V)$. This is a general apprach to model aggregated loads, such as residential, agricultural, and industrial feeders [92]. While combination of different types of load can lead to different model complexities, here one type of load is considered just for the purpose of explanation. The approach can be then easily extended to other types of load (static, dynamic, etc.). The work in [92] describes static and dynamic load characteristics, where the active p_L and the reactive q_L load powers depend both on the frequency and the amplitude of the voltage waveform. Furthermore, a dynamic description of the loads can be added [96–98]:

$$p_L\,(f,\, V) = P_0\,(1 + k_{pf}a)\,\left(\frac{b + V_o}{V_o}\right)^{k_{pu}} \tag{2.13a}$$

$$q_L\,(f,\, V) = Q_0\,(1 + k_{qf}a)\,\left(\frac{b + V_o}{V_o}\right)^{k_{qu}} \tag{2.13b}$$

where:

$$a \triangleq \mathfrak{L}^{-1}\left[\frac{1}{1+sT_1}\mathfrak{L}\,[\Delta f]\right] \tag{2.14a}$$

$$b \triangleq \mathfrak{L}^{-1}\left[\frac{1}{1+sT_1}\mathfrak{L}\,[\Delta V]\right] \tag{2.14b}$$

and where P_o and Q_o are the active and reactive powers that are absorbed at nominal frequency f_o and nominal voltage amplitude V_o, and $\mathfrak{L}^{-1}$ is the Laplace

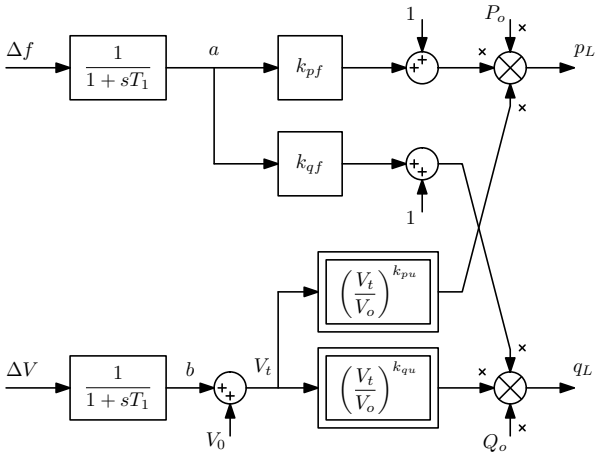

Figure 2.8: Dynamic load model [97]

anti-transform. Moreover, k_{pf}, k_{pu}, k_{qf}, and k_{qu} are constant parameters which depend on the nature of the aggregated load [92]. Finally, the voltage and frequency deviations from their nominal parameters are denoted as $\Delta V = V - V_o$ and $\Delta f = (f - f_o)/f_o$, respectively. A schematic representation of the load model is in Fig. 2.8.

The load powers p_L and q_L can be expressed in terms of the space vectors of voltage $\mathbf{v}$ and current $\mathbf{i}$ of the load itself and two real relations similar to those in (2.5) can be obtained. Substituting these two equations in (2.13), evaluating φ_i and I, the system can be linearized similarly as done in Sec. 2.3.1, leading to:

$$\begin{cases} \dfrac{\mathrm{d}}{\mathrm{d}t}\Delta a &= -\dfrac{1}{T_1}\Delta a + \dfrac{1}{T_1}\Delta f \\ \dfrac{\mathrm{d}}{\mathrm{d}t}\Delta b &= -\dfrac{1}{T_1}\Delta b + \dfrac{1}{T_1}\Delta V \\ \Delta\varphi_i &= \Delta\varphi_v + \left.\dfrac{\partial\varphi_i}{\partial a}\right|_Q \Delta a + \left.\dfrac{\partial\varphi_i}{\partial b}\right|_Q \Delta b \\ \Delta I &= \left.\dfrac{\partial I}{\partial V}\right|_Q \Delta V + \left.\dfrac{\partial I}{\partial a}\right|_Q \Delta a + \left.\dfrac{\partial I}{\partial b}\right|_Q \Delta b \end{cases} \tag{2.15}$$

Considering that Δf is equal to the time derivative of $\Delta\varphi_v$ divided by 2π and substituting this relation in the first equation of (2.15), the system (2.15)

can be written with a new state:

$$\Delta c \triangleq \Delta a - \frac{1}{2\pi T_1}\Delta\varphi_v \tag{2.16}$$

With this transformation, the final state-space model for the load results:

$$\begin{cases} \dfrac{\mathrm{d}}{\mathrm{d}t}\Delta z &= A_l\Delta z + B_l\Delta g \\ \Delta y &= C_l\Delta z + D_l\Delta g \end{cases} \tag{2.17}$$

where $\Delta z \triangleq [\,\Delta c \;\; \Delta b\,]^T \in \mathbb{R}^{2\times 1}$ is the state of the model, and the input vector Δg and the output vector Δy are defined as in Sec. 2.3.1. The four matrices result:

$$A_l = -\frac{1}{T_1}\begin{bmatrix} 1 & 0 \\ 0 & 1 \end{bmatrix} \qquad B_l = \frac{1}{T_1}\begin{bmatrix} -\frac{1}{2\pi T_1} & 0 \\ 0 & 1 \end{bmatrix} \tag{2.18a}$$

$$C_l = \begin{bmatrix} \frac{\partial\varphi_i}{\partial a} & \frac{\partial\varphi_i}{\partial b} \\ \frac{\partial I}{\partial a} & \frac{\partial I}{\partial b} \end{bmatrix} \qquad D_l = \begin{bmatrix} 1+\frac{1}{2\pi T_1}\frac{\partial\varphi_i}{\partial a} & 0 \\ \frac{1}{2\pi T_1}\frac{\partial I}{\partial a} & \frac{\partial I}{\partial V} \end{bmatrix} \tag{2.18b}$$

where $A_l,\ B_l,\ C_l,\ D_l \in \mathbb{R}^{2\times 2}$.

2.3.3 Overall small-signal model

The models of load and inverter, which have the same input vector Δg and the same output vector Δy, have to be linked in order to study the stability of the overall system. For the purpose of explanation, consider that

$$H \triangleq (D_i - D_l) \quad \text{is} \quad \text{invertible.} \tag{2.19}$$

In this case, the model of the whole system can by found by putting together

the two models (2.11) and (2.17):

$$\frac{\mathrm{d}}{\mathrm{d}t}\begin{bmatrix}\Delta\varphi_p\\ \Delta z\end{bmatrix} = \underbrace{\begin{bmatrix}A_i - B_i H^{-1} C_i & B_i H^{-1} C_l\\ -B_l H^{-1} C_i & A_l + B_l H^{-1} C_l\end{bmatrix}}_{\triangleq F}\begin{bmatrix}\Delta\varphi_p\\ \Delta z\end{bmatrix} \tag{2.20}$$

To study the dynamic behavior of the system close to a particular operating point Q, the eigenvalues of the matrix F can be evaluated. Some results of this model can be found in [8].

2.4 Temporary unintentional islanded operation

In this section, the test-case of Fig. 2.1 in islanded operation is modeled to analytically describe the area modifications introduced with Fig. 2.4, as in [93]. With other words, this section extends the work done in Sec. 2.3 and in particular it applies the derived models in order to analytically draw the NDZs.

The power inverter of Fig. 2.1 is controlled with a multiple loop structure, as shown in Fig. 2.9 (θ_p is the PLL phase in the abc domain). It includes an inner current regulation loop that ensures the tracking of two current references (in phase and orthogonal with respect to the voltage) which come from outer power loops that track power references from the P/f and Q/V droop regulators of [7]. An SRF-PLL, as in [94, 99], is used to synchronize the current regulation loop to the voltage waveform. Furthermore, the PLL gives the voltage amplitude and frequency measurements to the droop regulation scheme. In this Chapter, the active power loop of the inverter is an abstraction to simplify the analysis and to describe the behavior of a real PV inverter (more details are in Sec. 2.5.1).

2.4.1 Modeling for a generator with constant active and reactive powers

First, a dynamic model for Case I is described to predict the temporary NDZ and then a possible extension to account the droop regulations of Cases II-IV is proposed. This analysis is based on the observation that the predominant

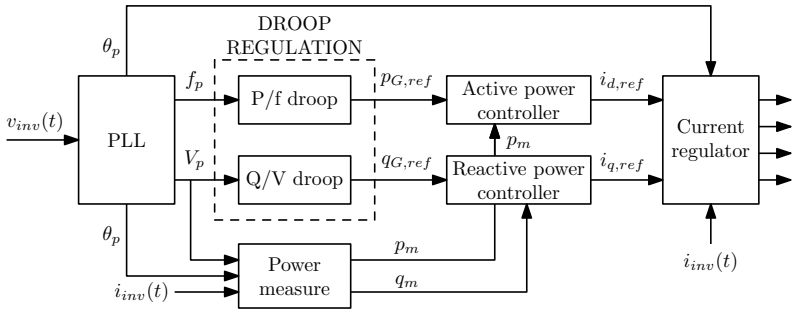

Figure 2.9: Inverter control architecture with active and reactive power loops and P/f and Q/V droop regulation [93]

dynamic during the islanded operation for Case I is due to the PLL, while the current loop and power loop dynamics are faster and not essential for the prediction of the voltage within the reclosing time of $600\,\mathrm{ms}$. This drives to provide only a static description of the current and power regulation loops, while all the dynamic contribution of the model is related to the PLL. These assumptions are later evaluated with simulations.

Considering an SRF-PLL synchronized to the q axis as in [99], the d voltage component is used as measured voltage amplitude and the phase detection process considers the q component of the voltage:

$$v_d = V\cos\xi \triangleq V_p \tag{2.21a}$$

$$v_q = V\sin\xi \tag{2.21b}$$

where ξ is the phase shift between the actual voltage space vector (phase φ_v in dq frame) and the reference frame of the PLL (phase φ_p) and V is the actual voltage amplitude at the inverter output (as in Sec. 2.3).

Neglecting the current and power loop dynamics, the feedback powers are always equal to their power references:

$$\mathbf{s}_{G,ref} = p_{G,ref} + jq_{G,ref} = \frac{3}{2}V_p\left[\frac{Ve^{j\xi}}{\mathbf{Z}_L(f)}\right]^* = \frac{3}{2}\frac{V^2\cos\xi e^{-j\xi}}{\mathbf{Z}_L(f)^*} \tag{2.22}$$

where the argument of the complex conjugation * is the inverter current space vector in the reference frame of the PLL. Evaluating the absolute value and the

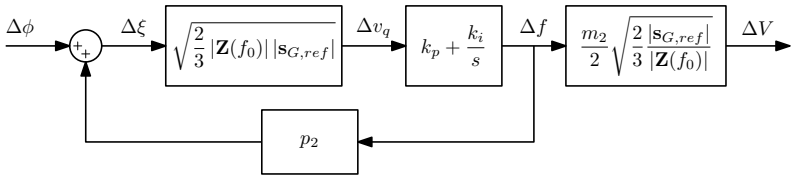

Figure 2.10: Small-signal model for constant power inverter (Case I) [93]

argument of (2.22), it results:

$$V = \sqrt{\frac{2\,|\mathbf{Z}_L(f)|\,|\mathbf{s}_{G,ref}|}{3\,|\cos\xi|}} \tag{2.23a}$$

$$\xi = \arg\mathbf{Z}_L(f) - \arg\mathbf{s}_{G,ref} \tag{2.23b}$$

V and ξ of (2.23) can be substituted into (2.21) for v_d and v_q components. The resulting equations (not explicitly written here) can be linearized in the grid-connected operating point, which is the steady-state solution just before the grid disconnection: $\xi = 0$ because the PLL is synchronized ($v_q = 0$) and $f = f_o$ because the frequency of the mains is supposed to be equal to the nominal frequency f_o.

This small-signal analysis leads to the model that is represented in Fig. 2.10 that relates the deviations of the corresponding quantities, indicated with Δ, from the steady-state values. In such diagram, m_2 and p_2 are respectively the derivatives of the absolute value and of the phase of load impedance with respect to the frequency f. The relation $\Delta\xi = p_2\Delta f$ comes from the (2.23b).

The input $\Delta\phi$ of such model is a phase perturbation that triggers the PLL transient and it is due to the new regime that is established just after the disconnection: it is caused by the sudden cancellation of the grid current. This is a fast transient due to load, current regulator, and power regulator dynamics that is evaluated imposing the inverter power $\mathbf{s}_{G,ref}$ equal to the load power in the reference plane of the PLL just before the disconnection.

The overall Laplace transfer functions $H_{\phi f}(s)$ from the input $\Delta\phi$ to the

output Δf and $H_{\phi V}(s)$ from the input $\Delta\phi$ to the output ΔV are:

$$H_{\phi f}(s) = -\frac{1}{p_2} \cdot \frac{1 + s\frac{k_p}{k_i}}{1 + s\frac{hp_2k_p - 1}{hp_2k_i}} \tag{2.24a}$$

$$H_{\phi V}(s) = \frac{m_2}{2}\sqrt{\frac{2}{3}\frac{|\mathbf{s}_{G,ref}|}{|\mathbf{Z}(f_o)|}} \cdot H_{\phi f}(s) \tag{2.24b}$$

where $h \triangleq \sqrt{2\,|\mathbf{Z}(f_o)|\,|\mathbf{s}_{G,ref}|\,/3}$. With (2.24), the PLL frequency and the voltage amplitude of the inverter can be evaluated in terms of step response (Laplace anti-transform) for a certain time $\bar{t}$ after the grid disconnection or to predict the whole transient after the disconnection.

2.4.2 Extension for P/f and Q/V droop

Now a possible extension of the model described in Sec. 2.4.1 is introduced to address the Cases II-IV. Starting from Case IV, the P/f and Q/V droop controllers change the active and reactive power references $\mathbf{s}_{G,ref} = p_{G,ref} + jq_{G,ref}$ in (2.22) and so (2.23) has now to be differentiated also with respect to $p_{G,ref}$ and $q_{G,ref}$, leading to:

$$\Delta V = \frac{\partial V}{\partial f}\Delta f + \frac{\partial V}{\partial p_{G,ref}}\Delta p_{G,ref} + \frac{\partial V}{\partial q_{G,ref}}\Delta q_{G,ref} \tag{2.25a}$$

$$\Delta \xi = \frac{\partial \xi}{\partial f}\Delta f + \frac{\partial \xi}{\partial p_{G,ref}}\Delta p_{G,ref} + \frac{\partial \xi}{\partial q_{G,ref}}\Delta q_{G,ref} \tag{2.25b}$$

Starting from Fig. 2.10 and including (2.25), a new small-signal diagram can represent the model of the Case IV: it is shown in Fig. 2.11. In this diagram, there are two linear approximations of the droop curves (the slopes k_{pf} and k_{qu}) and their response times (τ_p and τ_q). For a first approximation, the response times of the P/f and Q/V curves together with the dynamic of the power loops can for instance be modeled with two low-pass filters. From the small-signal model of Fig. 2.11, it is also possible to obtain a description for the Case II and III: this can be done by setting k_{pf} or k_{qv} equal to zero respectively, in order to disable the P/f or Q/V curve.

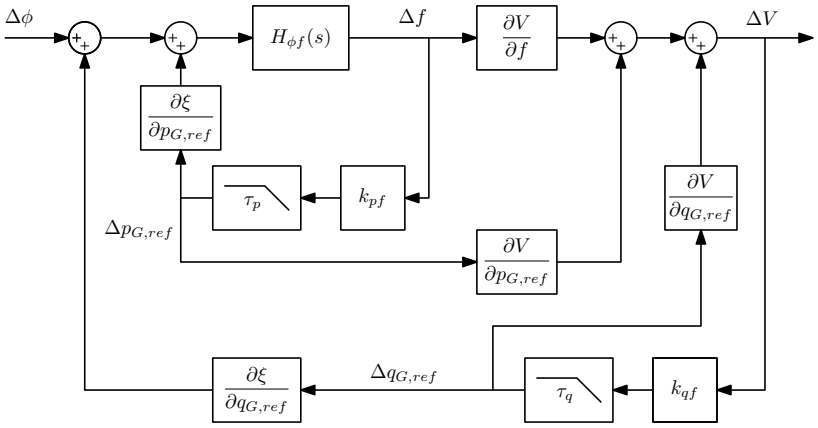

Figure 2.11: Small-signal model for Cases II-IV [93]

The model described in this section is used in Sec. 2.5.3 to analytically draw the NDZ for the Case I: these results are also validated with simulations. Moreover, in Sec. 2.5.3 the NDZ shaping due to P/f and Q/V droop control and in particular due to their speed is addressed via simulation-based analyses considering all the four Cases. In the same section, these results are also shown with experimental tests.

2.5 Results

In this section, the results for permanent and temporary unintentional islanding risks are reported and validated. First in Sec. 2.5.1 the test-case used for all the following results is described. Then in Sec. 2.5.2 the analytic results for permanent islanding described in Sec. 2.2 are validated experimentally showing an increase of the NDZ, and so of UIO risk, introducing droop control. Finally Sec. 2.5.3 extends these results also for the temporary islanding issue, using the dynamic model of Sec. 2.4 and exploiting simulations and the experimental validations.

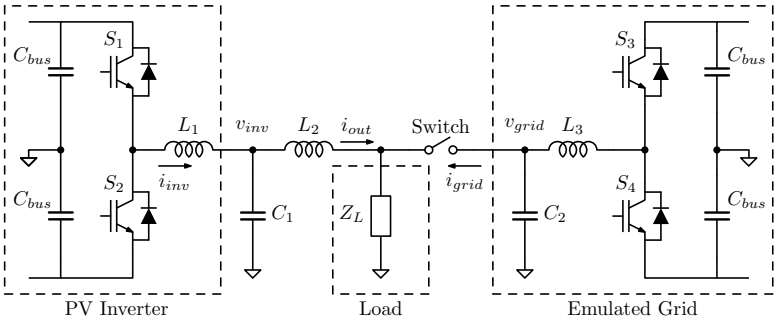

Figure 2.12: Test-bed configuration [74]

2.5.1 Test-case for simulation and experiments

A lab-scale prototype has been implemented in order to perform preliminary experimental validations and its configuration is shown in Fig. 2.12: a switch allows the islanded operation by isolating the PV inverter and the passive load Z_L from the main grid [74, 93]. Here, the same load structure described in Sec. 2.2 is adopted: its parameters are in Tab. 2.1. This test-case is used for all the following results, i.e. analytic, simulation, and experimental ones. The analyses on this test-case, and in particular the experimental results, were carried out in collaboration and with the coordination of the activities done by Mr. Riccardo Sgarbossa during his Ph.D. program.

The PV inverter is equipped with closed-loop controllers to ensure that the active and reactive power references are properly tracked (Fig. 2.13). An SRF-PLL is used to synchronize the current controller of the inverter to the grid voltage and to get the frequency and amplitude measurements for the P/f and Q/V droop control. If one of the droop characteristics is disabled, the corresponding power reference will be constant regardless the frequency or the voltage amplitude. The outputs of the PLL together with the output current measurement of the inverter are used to evaluate the output active and reactive powers of the inverter: these are feedback variables for the power regulator. The power regulator changes the PPT reference of the DC-DC converter to meet the active power request $p_{G,ref}$, while the reactive power request is met changing the reactive current reference of the current controller. Moreover, the current controller sets the inverter active current reference to keep the regulation of the DC link

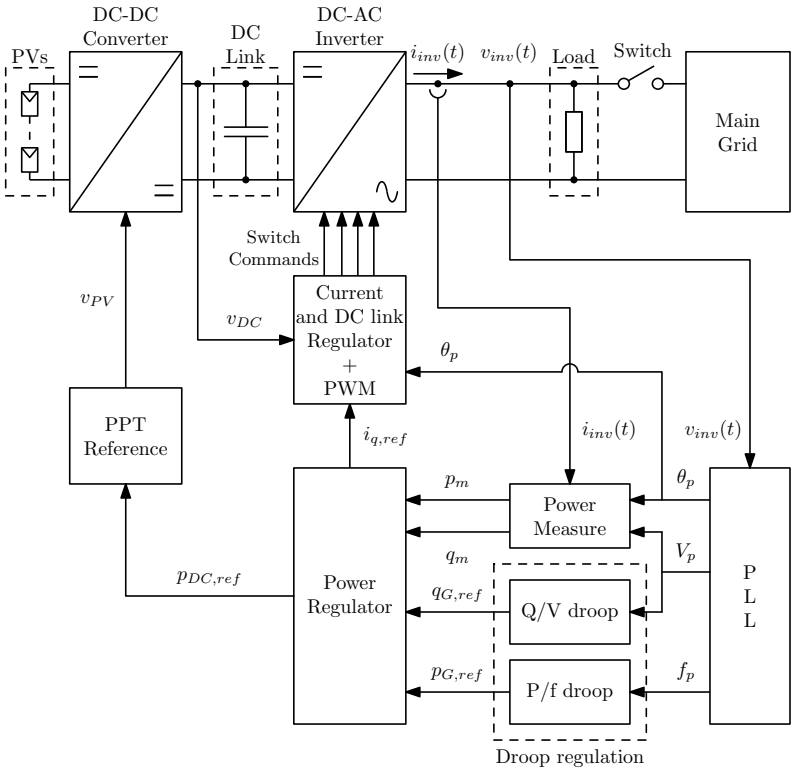

Figure 2.13: Inverter control architecture with active and reactive power loops and P/f and Q/V droop regulation [74]

voltage, that is it injects all the available active power that is provided by the first DC-DC stage [74].

2.5.2 Permanent islanding

In Sec. 2.2, the analysis of permanent islanding shows that the static NDZ increases introducing droop control and here these results are validated experimentally. The test-case of Sec. 2.5.1 is used with a nominal phase voltage of $182\,\mathrm{V_{rms}}$ and the nominal line frequency is $f_o = 50\,\mathrm{Hz}$. Experimental results confirm the static analysis done previously: in particular Fig. 2.14.a refers to Case II, Fig. 2.14.b to Case III, and 2.14.c to Case IV. In these figures, there is a good agreement between static analysis of Sec. 2.2 reported again in Fig. 2.14 with dashed lines and experimental results, i.e. circles and asterisks. All the results indicate that the risk of UIO increases introducing inverter droop control

with respect to the case of a constant power inverter and that such risk is higher introducing both P/f and Q/V droop control. It is also possible to notice that the effect of the P/f droop is stronger in terms of area change than the Q/V droop one.

All the islanded points inside the NDZs of Fig. 2.14 result to be permanent islanded operations; this means that the islanded operating points in terms of frequency and voltage amplitude do not trigger the protections of Fig. 1.15: some examples are in Fig. 2.15. In such figures, the Test 20 of Fig. 2.14 is considered: it exhibits a frequency value out of the thresholds for the Case II ($64.8\,\mathrm{Hz}$) in Fig. 2.15.a, a voltage close to the minimum voltage threshold $182 \cdot 0.85 = 154.7\,\mathrm{V_{rms}}$ for Case III ($158.7\,\mathrm{V_{rms}}$) in Fig. 2.15.b, and frequency and voltage values within the thresholds for Case IV ($50.59\,\mathrm{Hz}$ and $173.5\,\mathrm{V_{rms}}$) in Fig. 2.15.c.

In the experimental results for permanent islanding considerations, the protections defined with Fig. 1.15 are never triggered in steady-state operation. However the stability of the operating point can sometimes be poor presenting oscillating behaviors: an example of this aspect is the Test 31 for Case IV in Fig. 2.16. Anyway, such instability does not trigger the DER protections and so a permanent islanded operation is still achieved. This phenomenon can be further investigated, for example applying the stability analysis described in Sec. 2.3.

Another cause that can trigger the DER protections is the initial transient due to the grid disconnection, when the frequency and the voltage can exhibit some oscillations bringing those quantities outside the thresholds of Fig. 1.15. However, all the Tests within the NDZ considered in this section do not trip the protections during the transient, even if this phenomenon should be analyzed and understood in detail, because different results can be achieved with different points in the $\Delta P - \Delta Q$ plane. To these aims, the analysis presented for temporary islanding issue in Sec. 2.4 can help analytically describe the disconnecting transient: some results are given in Sec. 2.5.3 together with simulation-based and experimental results.

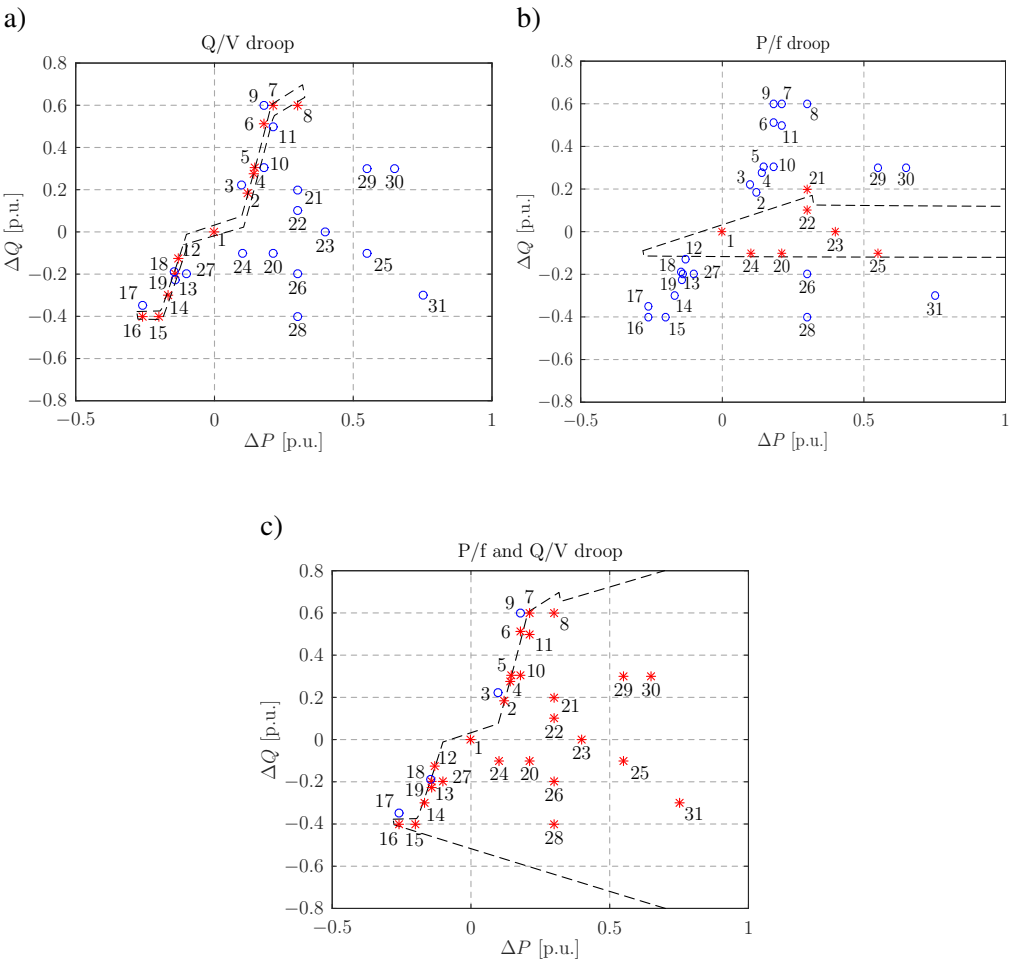

Figure 2.14: Experimental results of $\Delta P - \Delta Q$ area of permanent unintentional islanding: a) Case II, b) Case III, and c) Case IV; circles refer to an islanded operation out of the protection thresholds of Fig. 1.15, asterisks refer to an islanded operation within the protection thresholds; dashed lines are evaluated analytically as in Sec. 2.2 [74]

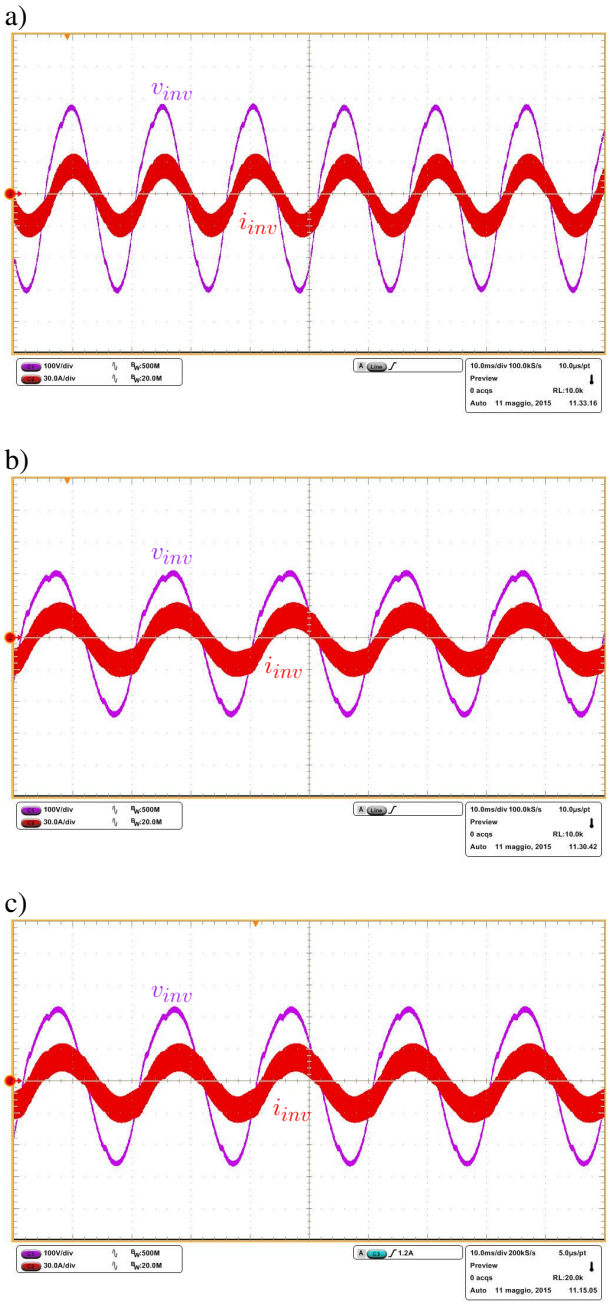

Figure 2.15: Experimental results of inverter output voltage v_{inv} ($100\,\mathrm{V/div}$) and current i_{inv} ($30\,\mathrm{A/div}$) for Test 20 of Fig. 2.14: a) Case II where the frequency is $64.8\,\mathrm{Hz}$ and the voltage $203.6\,\mathrm{V_{rms}}$, b) Case III where the frequency is $50.62\,\mathrm{Hz}$ and the voltage $158.7\,\mathrm{V_{rms}}$, and c) Case IV where the frequency is $50.59\,\mathrm{Hz}$ and the voltage $173.5\,\mathrm{V_{rms}}$; time with $10\,\mathrm{ms/div}$ scale [74]

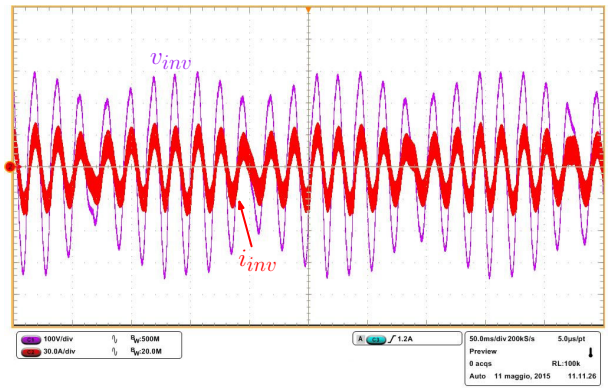

Figure 2.16: Experimental results of inverter output voltage v_{inv} ($100\,\mathrm{V/div}$) and current i_{inv} ($30\,\mathrm{A/div}$) for Case IV for Test 31 of Fig. 2.14; time with $50\,\mathrm{ms/div}$ scale [74]

Table 2.3: Load parameters: base impedance is at f_o ($14.36\,\Omega$)

R_1	=	$18\,\Omega$	=	$0.798\,\mathrm{p.u.}$
R_2	=	$82.5\,\Omega$	=	$0.174\,\mathrm{p.u.}$
L_1	=	$87.5\,\mathrm{mH}$	=	$0.534\,\mathrm{p.u.}$
C_1	=	$14.4\,\mu\mathrm{F}$	=	$0.065\,\mathrm{p.u.}$
C_2	=	$60\,\mu\mathrm{F}$	=	$0.271\,\mathrm{p.u.}$

2.5.3 Temporary islanding

Now a comparison between the results of the small-signal model of Sec. 2.4.1 and a detailed time-domain simulation (in Matlab/Simulink), that considers the full architecture of Figs. 2.1 and 2.9, is shown [93]. The nominal voltage amplitude is now $V_o = 90\,\mathrm{V_{RMS}}$ (phase to neutral). The PLL that is used is an SRF-PLL with a closed-loop bandwidth of $5\,\mathrm{Hz}$, while the external power loops have a closed-loop bandwidth of $7\,\mathrm{Hz}$ for the active power and of $5\,\mathrm{Hz}$ for the reactive power. The parameters of the load are now those reported in Tab. 2.3.

Fig. 2.17 shows the frequency f measured by the PLL and the voltage amplitude V of the inverter after a grid disconnection when $\Delta P = 0.2\,\mathrm{p.u.}$ and $\Delta Q = 0.4\,\mathrm{p.u.}$ (base power is the apparent load power, here $570\,\mathrm{VA}$ per phase). The voltage transient consists of a fast variation (less than $50\,\mathrm{ms}$) due to the load, the current and power loop dynamics and a slower one due to the PLL. The mathematical model described in Sec. 2.4 predicts the frequency and

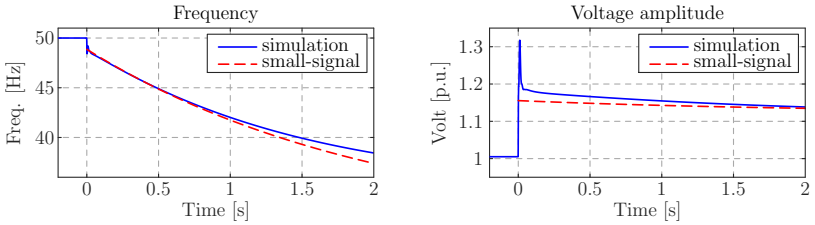

Figure 2.17: Comparison between the small-signal model results and a detailed simulation: the frequency measured by the PLL and the actual voltage amplitude for a grid disconnection with $\Delta P = 0.2\,\text{p.u.}$ and $\Delta Q = 0.4\,\text{p.u.}$ for Case I [93]

the voltage transients, except for the fast initial voltage variation, and it can estimate their values during the first $600\,\text{ms}$: observe that the transient in the first $200\,\text{ms}$ is not important since there is no voltage limit (Fig. 1.15).

With the Laplace anti-transform of $H_{\phi V}(s) \cdot \Delta\phi$ (Sec. 2.4), the voltage, for instance, at $\bar{t} = 600\,\text{ms}$ can be set equal to the higher or lower threshold of Fig. 1.15. Doing this, the resulting system can be solved backward to find the amplitude of the step $\Delta\phi$ and then back to the active ΔP and reactive ΔQ power unbalances in grid-connected operation: this $\Delta P - \Delta Q$ point belongs to the NDZ border. This enables to find the borders in the $\Delta P - \Delta Q$ plane that contain the temporary unintentional islanding region. An example of such results is shown in Fig. 2.18, for the constant power inverter (Case I) where the solid lines delimit the uncontrolled $\Delta P - \Delta Q$ islanding region. In these results, the described approach is applied three times: at $\bar{t} = 200\,\text{ms}$ to set the voltage within $0.4 \div 1.15\,\text{p.u.}$, at $\bar{t} = 400\,\text{ms}$ and $\bar{t} = 600\,\text{ms}$ to set the voltage within $0.85 \div 1.15\,\text{p.u.}$. This is an approximation because such method can only be applied for a finite number of $\bar{t}$, instead the protections defined in Fig. 1.15 are valid for the whole interval $0 \div 600\,\text{ms}$. Moreover, the standard [7] defines the intervention times of the protections, i.e. the time interval while the voltage has to remain outside the thresholds of Fig. 1.15 to trigger the inverter disconnection. On the other hand, here the worst-case scenario is considered because such intervention times are all zero, for analytic, simulation, and experimental results.

In Fig. 2.18 the small-signal based results are compared with simulation-based results for region drawing. Dots indicate an UIO that is verified with

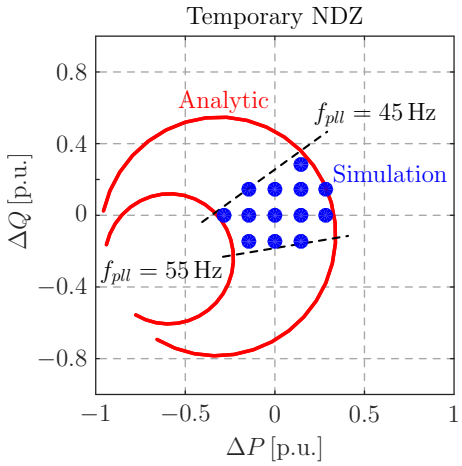

Figure 2.18: Analytic and simulation NDZ below 600 ms for Case I (powers normalized to the nominal load power) [93]

a detailed simulation of the system of Figs. 2.1 and 2.9 checking the voltage level of Fig. 1.15 for all the interval $0 \div 600$ ms. In the simulation results also frequency limits are considered to maintain the islanded operation; such limits are $45 \div 55$ Hz. The comparison shows that the analytic approach allows to draw the NDZ with a good approximation, considering that it is a worst case scenario. Furthermore, the region that is missing within the analytic borders is due to the frequency limits, that are tested analytically, while the voltage thresholds are well approximated.

Now, some simulation results show how the uncontrolled islanding areas change with the speed of P/f and Q/V droop characteristics for the system of Figs. 2.1 and 2.9. The architecture and the control of the system are the same described previously in this section, with the same parameters. Also the NDZs are obtained with the same method described previously.

In Fig. 2.19, there are three NDZs for an inverter with P/f and Q/V droop characteristics for different rise times of the active τ_p and reactive τ_q power loops (Case IV). These response times may be due to the frequency and voltage measurements of droop controllers, some particular filtering structures, the power loop response times themselves or some time requirements of droop control imposed by the standard [7]: here they are all accounted in τ_p and τ_q.

From the results of Fig. 2.19, it follows that the risk of unintentional is-

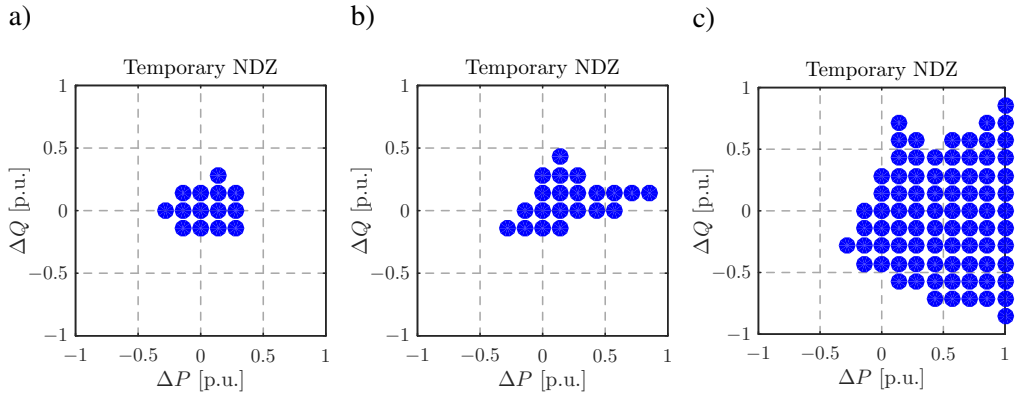

Figure 2.19: Simulation results for $\Delta P - \Delta Q$ area of unintentional islanding (for a 600 ms time) when the inverter operates with droop characteristics according to [7] for different power response times (Case IV): a) with $\tau_p = 5\,\mathrm{s}$ and $\tau_q = 5.8\,\mathrm{s}$; b) with $\tau_p = 1\,\mathrm{s}$ and $\tau_q = 1.5\,\mathrm{s}$ and c) with $\tau_p = 0.24\,\mathrm{s}$ and $\tau_q = 0.35\,\mathrm{s}$ (ΔP and ΔQ are normalized to the nominal load power) [93]

landing with droop controlled inverter is potentially higher than with constant power inverter, because these regions are larger (the results for Case I are in Fig. 2.18). The qualitative consideration described with Fig. 2.4 can also be seen here, since the $\Delta P - \Delta Q$ area widens for faster P/f and Q/V droop regulations (i.e. for smaller τ_p and τ_q). This means that the unintentional islanding risk increases with faster systems. However, it has to be remarked that this is not generally true because in some cases fast droop regulation may destabilize the islanded system, leading to a reduction of the risk of temporary islanding, as shown afterwards.

In Fig. 2.20 there are some examples of time-domain simulations for the disconnecting transient in terms of the grid voltage and PLL frequency. They are done for the same $\Delta P = 0.29\,\mathrm{p.u.}$ and $\Delta Q = -0.14\,\mathrm{p.u.}$, for different rise times τ_p and τ_q. Such results start showing that faster droop control does not always guarantee islanding condition: in Fig. 2.20.a the voltage does not trigger the DER protections, while they trip in 2.20.b for faster droop regulation. However, if the droop speed is increased more the $\Delta P - \Delta Q$ point returns inside the NDZ: in 2.20.c the voltage fulfills the thresholds of Fig. 1.15.

Results from the experimental setup, described in Sec. 2.5.1, are reported in the plane $\Delta P - \Delta Q$ in Fig. 2.21 (now the PLL has a closed-loop bandwidth

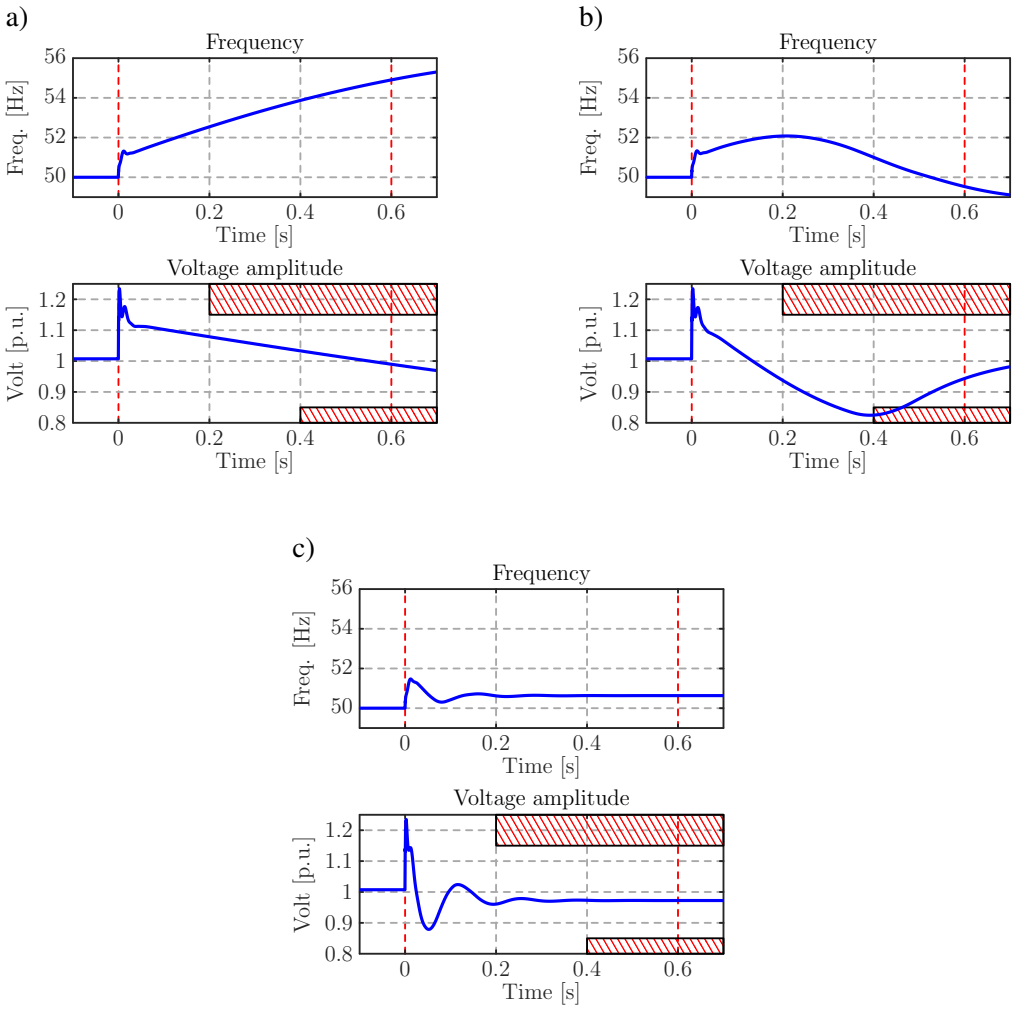

Figure 2.20: Test of Fig. 2.19 for $\Delta P = 0.29\,\text{p.u.}$ and $\Delta Q = -0.14\,\text{p.u.}$: example of temporary islanded operation (simulation results) a) with $\tau_p = 5\,\text{s}$ and $\tau_q = 5.8\,\text{s}$; b) with $\tau_p = 1\,\text{s}$ and $\tau_q = 1.5\,\text{s}$ and c) with $\tau_p = 0.24\,\text{s}$ and $\tau_q = 0.35\,\text{s}$ (ΔP and ΔQ are normalized to the nominal load power) [93]

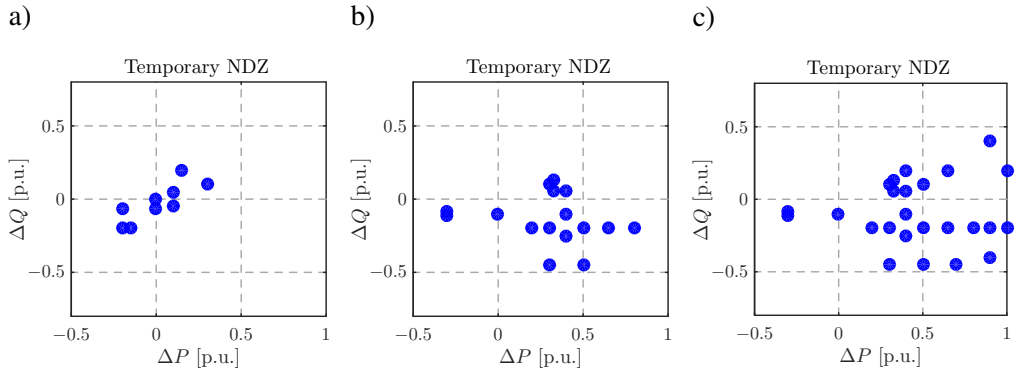

Figure 2.21: Experimental test results are reported in the plane $\Delta P - \Delta Q$ with different response times of the droop characteristics: a) for constant power references, b) for droop regulation with $\tau_p = 5\,\mathrm{s}$ and $\tau_q = 7.5\,\mathrm{s}$ and c) for droop regulation with $\tau_p = 2\,\mathrm{s}$ and $\tau_q = 3.5\,\mathrm{s}$; dot tests allow temporary islanded operations [93]

of $4\,\mathrm{Hz}$). Tests indicated with a dot represent UIO within $600\,\mathrm{ms}$. Each test is performed with different response times of the P/f and Q/V droop characteristics. Also some experimental result examples in the time domain are provided in Fig. 2.22 for $\Delta P = 0.9\,\mathrm{p.u.}$ and $\Delta Q = -0.2\,\mathrm{p.u.}$ for the three conditions of Fig. 2.21. All these results show again that the risk of UIO increases introducing droop control with respect to the case of a constant power inverter and that faster time responses on the active and reactive droop controllers, i.e. smaller τ_p and τ_q, lead to wider NDZs.

It is important to remark that so far a *potential* increase of the unintentional islanding risk due to fast droop regulation has been shown in a particular situation. This phenomenon can sometimes not appear indeed, for example because faster droop controllers may destabilize the islanded system, leading to a reduction of the NDZ. This can be due to several aspects from different PV installations in the distribution grid, for example for different control implementation details, bandwidths of the inner inverter regulators, local load structure, etc. The experimental region in Fig. 2.23 highlights this phenomenon because a reduction of the NDZ appears compared to the NDZs of Fig. 2.21: the same experimental setup used for Fig. 2.21 now includes faster droop regulators with $\tau_p = 0.6\,\mathrm{s}$ and $\tau_q = 1.4\,\mathrm{s}$. Fig. 2.24, for $\Delta P = 0.9\,\mathrm{p.u.}$ and $\Delta Q = -0.2\,\mathrm{p.u.}$, shows that this happens because such response times make the system less sta-

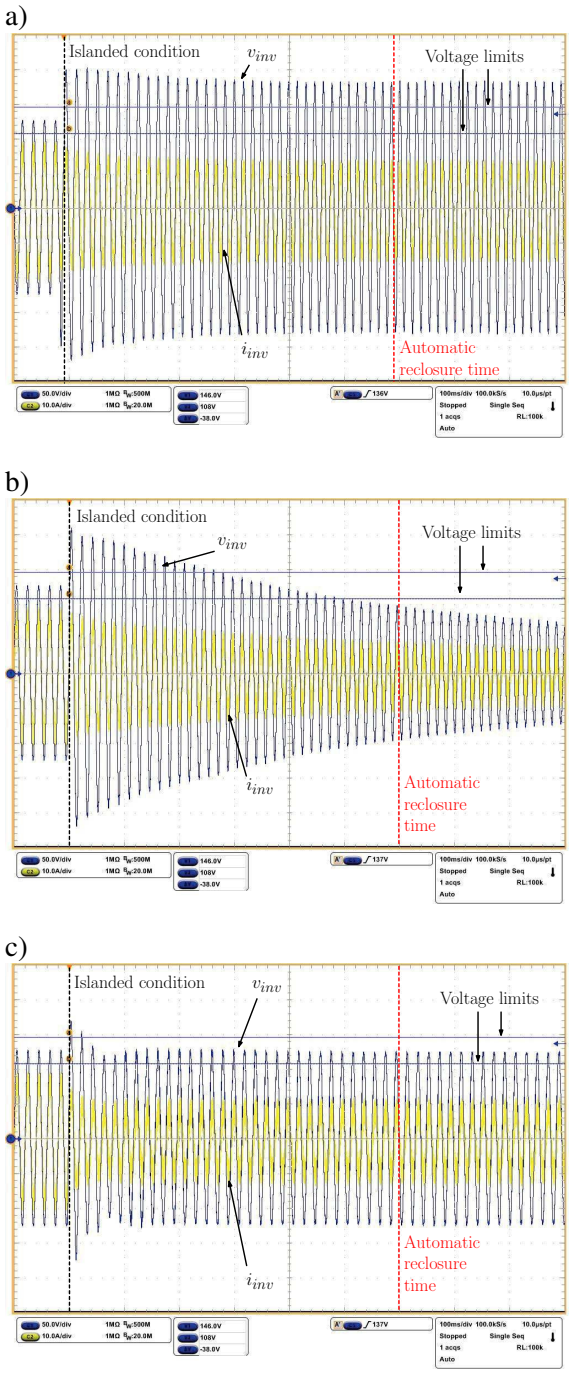

Figure 2.22: Test with $\Delta P = 0.9\,\text{p.u.}$ and $\Delta Q = -0.2\,\text{p.u.}$ of Fig. 2.21: example of temporary islanded operation (experimental results) a) for constant power inverter, b) for droop control with $\tau_p = 5\,\text{s}$ and $\tau_q = 7.5\,\text{s}$ and c) for $\tau_p = 2\,\text{s}$ and $\tau_q = 3.5\,\text{s}$; $v(t) \rightarrow 50\,\text{V/div}$, $i(t) \rightarrow 10\ \text{A/div}$, time $\rightarrow 100\,\text{ms/div}$ [93]

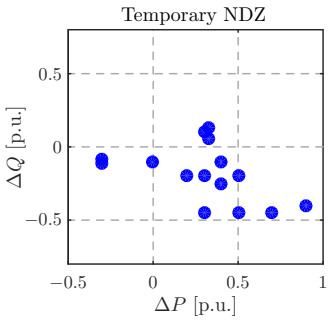

Figure 2.23: Experimental test results are reported in the plane $\Delta P - \Delta Q$ for droop regulation with $\tau_p = 0.6\,\mathrm{s}$ and $\tau_q = 1.4\,\mathrm{s}$ response times: dot tests allow temporary islanded operations [93]

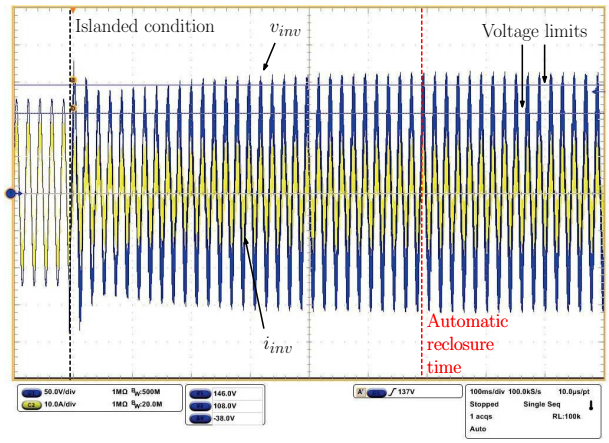

Figure 2.24: Test with $\Delta P = 0.9\,\mathrm{p.u.}$ and $\Delta Q = -0.2\,\mathrm{p.u.}$ for Fig. 2.23: example of temporary islanded operation (experimental results) for $\tau_p = 0.6\,\mathrm{s}$ and $\tau_q = 1.4\,\mathrm{s}$; $v(t) \to 50\,\mathrm{V/div}$, $i(t) \to 10\ \mathrm{A/div}$, time $\to 100\,\mathrm{ms/div}$ [93]

ble.

2.6 Possible standard modifications

In this section, an algorithm to reduce the $\Delta P - \Delta Q$ region and so the risk of UIO of Case IV is described and then tested with simulations and experiments. The main idea of this technique comes from observing that the NDZs of simultaneous droop functions (Fig. 2.19) are larger than those of non-simultaneous cases (Case II and III), reported in Fig. 2.25.

So considering the case of an inverter that is controlled with both P/f and Q/V droop functions to support the voltage and the frequency regulations in grid-connected mode as the standard [7] imposes, it is possible to shrink the NDZ by disabling the P/f or Q/V droop during particular transients. For example, here this technique is tested:

- during standard operation, usually at frequency and voltage close to the nominal values, both P/f and Q/V remain enabled;
- when the frequency of the grid grows above $50.3\,\mathrm{Hz}$ for more than a specified time interval (here $100\,\mathrm{ms}$), the Q/V droop curve is disabled and the inverter continues to inject the reactive power of the nominal voltage point.

Notice that using this technique does not reduce the capabilities of voltage and frequency regulation support of the PV inverter during grid-connected operation.

In Fig. 2.26 there are some simulation results that test this algorithm: comparing these NDZs with those of the Case IV in Fig. 2.19, it follows that the unintentional islanding risk is reduced. In particular the reduction is larger for faster droop controllers.

Other figures obtained through experiments are reported to test the behavior of non-simultaneous droop controllers and of the proposed algorithm to reduce the NDZ. Fig. 2.27 shows the NDZs for Cases II and III for two different speeds of the power loops, i.e. τ_p and τ_q, while in Fig. 2.28 there are the results for the proposed on-line method for NDZ reduction. It is possible to notice also experimentally a reduction of the $\Delta P - \Delta Q$ region with the controller of this section: this reduction is more visible for faster droop controllers, i.e. 2.28.b.

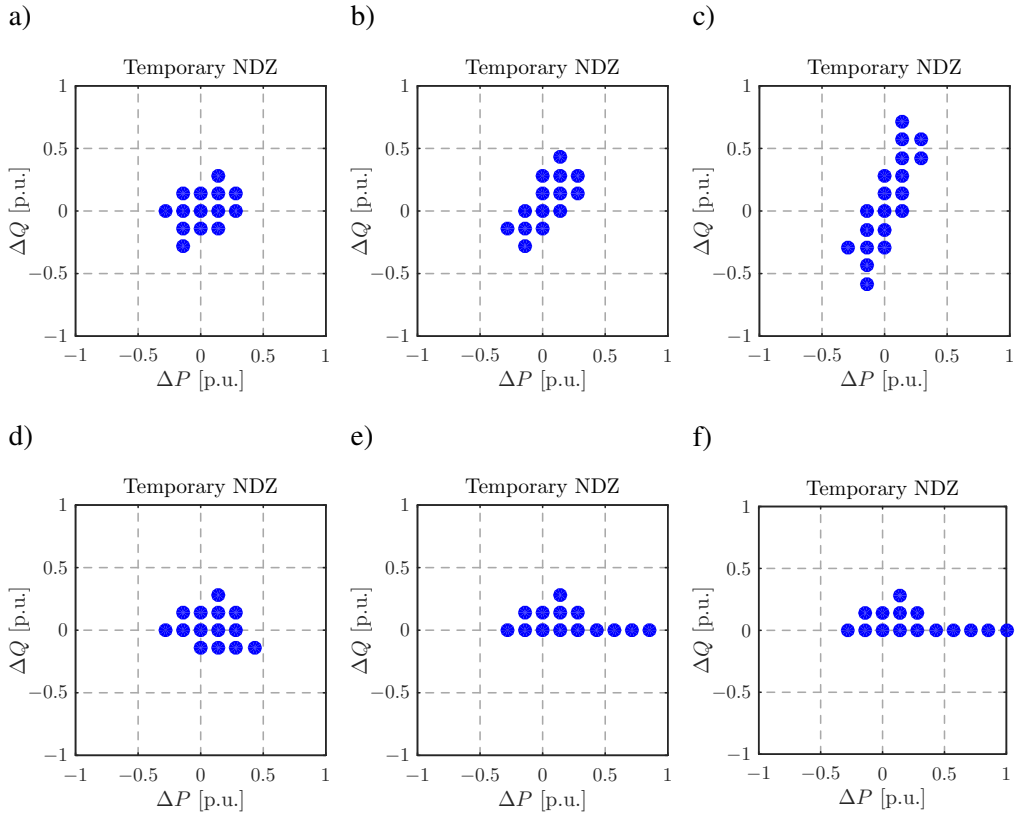

Figure 2.25: Simulation results for $\Delta P - \Delta Q$ area of unintentional islanding (for a 600 ms time) when the inverter operates with non-simultaneous droop characteristics: a), b), and c) for Case II and d), e), and f) for Case III; for different power response times: a) and d) with $\tau_p = 5\,\text{s}$ and $\tau_q = 5.8\,\text{s}$; b) and e) with $\tau_p = 1\,\text{s}$ and $\tau_q = 1.5\,\text{s}$ and c) and f) with $\tau_p = 0.24\,\text{s}$ and $\tau_q = 0.35\,\text{s}$ (ΔP and ΔQ are normalized to the nominal load power)

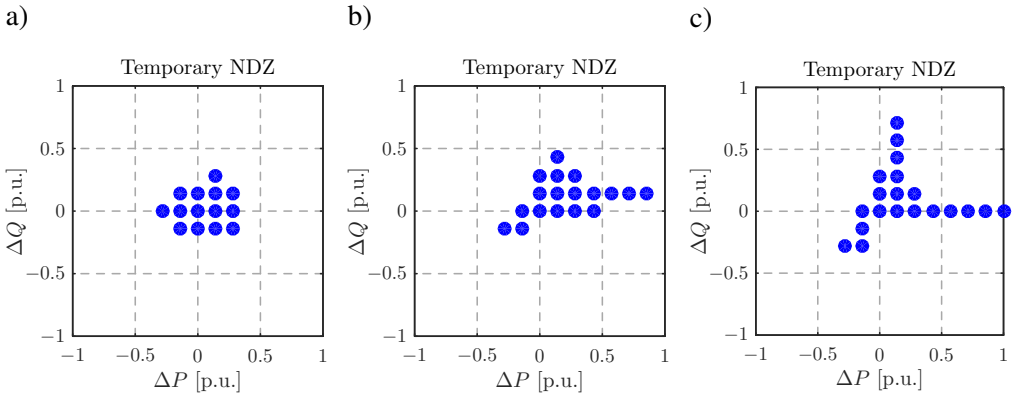

Figure 2.26: Simulation results for $\Delta P - \Delta Q$ area of unintentional islanding (for a 600 ms time) when the inverter operates with droop characteristics according to [7] (Case IV) and it is used the algorithm proposed in Sec. 2.6; for different power response times: a) with $\tau_p = 5\,\text{s}$ and $\tau_q = 5.8\,\text{s}$; b) with $\tau_p = 1\,\text{s}$ and $\tau_q = 1.5\,\text{s}$ and c) with $\tau_p = 0.24\,\text{s}$ and $\tau_q = 0.35\,\text{s}$ (ΔP and ΔQ are normalized to the nominal load power)

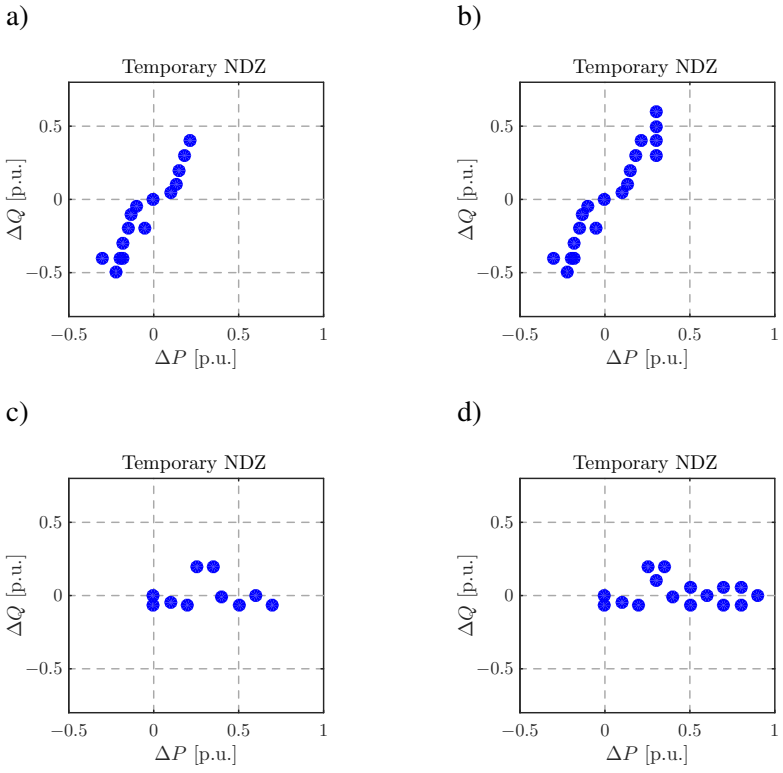

Figure 2.27: Experimental test results for non-simultaneous droop controllers are reported in the plane $\Delta P - \Delta Q$ with different response times: a) and b) for Case II and c) and d) for Case III; a) and c) with $\tau_p = 5\,\text{s}$ and $\tau_q = 7.5\,\text{s}$, and b) and d) with $\tau_p = 2\,\text{s}$ and $\tau_q = 3.5\,\text{s}$; dot tests allow temporary islanded operations

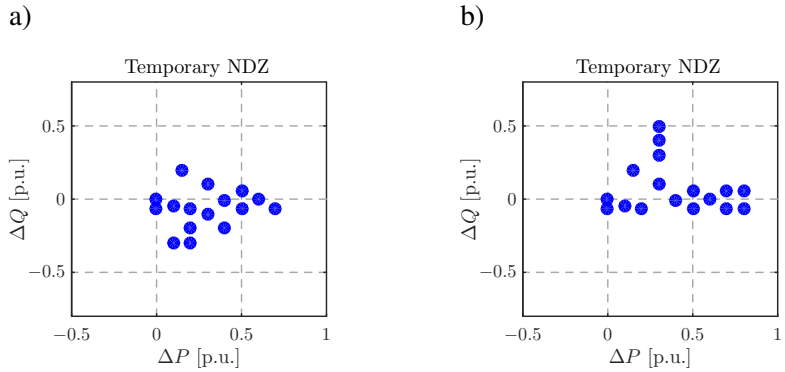

Figure 2.28: Experimental test results for the proposed control technique in order to reduce the NDZ in the plane $\Delta P - \Delta Q$ with different response times: a) with $\tau_p = 5\,\mathrm{s}$ and $\tau_q = 7.5\,\mathrm{s}$ and b) with $\tau_p = 2\,\mathrm{s}$ and $\tau_q = 3.5\,\mathrm{s}$; dot tests allow temporary islanded operations

2.7 Summary

This Chapter reports an assessment of the $\Delta P - \Delta Q$ area where permanent and temporary unintentional islanding can occur. In particular, temporary unintentional islanding is investigated for automatic reclosing procedures (under $600\,\mathrm{ms}$). The load and source dependencies of active and reactive powers to the voltage and frequency of the grid play an important role for sustaining islanded conditions, while the P/f and Q/V droop curves of the inverter can increase such risk.

For the permanent islanding, the proposed investigation shows that the risk of UIO increases introducing P/f or Q/V droop regulation to the control of DERs and that the $\Delta P - \Delta Q$ area widens more including both the P/f and Q/V droop regulations, rather than only one of them.

Also for the temporary islanding issue, the simultaneous case of droop control increases more the NDZ compared to the non-simultaneous cases. Furthermore, the speed of response of the P/f and Q/V droop functions enlarges the $\Delta P - \Delta Q$ area: the faster the time responses, potentially the larger the risk of temporary islanding.

Thus, the non-simultaneous operation of P/f and Q/V seems to be an effective approach to reduce the NDZ. An online method based on disabling the Q/V function under over-frequency operation is proposed and validated to reduce the

NDZ enlargement and to maintain the regulation support with droop functions during steady-state operation, as imposed by the standards.

All the results of this Chapter are given in terms of small-signal modeling, simulations and experimental verifications. In future generation of distribution grids with large penetration of RES, these kinds of analysis together with the understanding of the stabilizing effects of droop control in islanded operation are of paramount importance in order to provide insights on design criteria for DER connections and on settings of P/f and Q/V droop functions on future standards.

Chapter 3

Intentional islanded operation with grid transition

This Chapter describes a local controller for DERs to manage a microgrid during grid-connected and autonomous opearting modes as presented in [100]. It is based on the P/f and Q/V droop control described in Sec. 1.1.2: during grid-connected operation, the controller tracks active and reactive power references and, during islanded mode, it exploits the droop control properties to share the load among the DERs. The key point is to use the saturation of the active and reactive power controllers to enable a smooth transition from grid-connected to islanded mode without communication among the microgrid supervisor, the disconnecting switch, and DERs. The proposed analysis describes the controller in Sec. 3.2, including a design procedure in Sec. 3.3 with small-signal analyses. A Field Programmable Gate Array-based (FPGA) implementation of the controller is also realized and used to validate the results of this Chapter through a detailed Hardware-In-the-Loop (HIL) and RT simulation approach.

3.1 State of the art

Basic droop control as described in Sec. 1.1.2 can be used effectively only in the islanded operating mode and droop control in the form of (1.8) can not be used directly in grid-connected operation. The reason is that in grid-connected

mode the voltage amplitude and the frequency at the PCC are strictly imposed by the main grid and equations (1.8) with constant p_s and q_s do not ensure the desired DER active and reactive power generation.

To overcome this issue, different control techniques are proposed to manage separately DERs in the islanded and grid-connected modes and to handle the commutation between them [20]. One possible solution is to have two different controllers for the two operating modes and, basing on communication or islanding detection techniques, identify the operating mode in order to switch on the correct controller [101–104]. Other approaches exploit communication with the PCC for the grid-connected operation [21, 105] or use completly local controller but losing in terms of precision of the injected power regulation for grid-connected mode [106, 107].

So far only few approaches that operate in the same manner in both operating modes have been proposed. Examples are local regulators without the capability of managing the parallel connection of different inverters in islanded mode [108, 109] or central controllers based on time-critical communication which could reduce the reliability of the grid [110–113]. Another cause of reduced robustness is the lack of redundancy: for example, only one DER is critical for the operation of the whole microgrid in the master-slave approach of [114, 115].

The paper [116] proposes a universal regulator to manage the microgrid in both the operating modes, basing on P/f and Q/V droop control and without requiring communication in the microgrid. It exploits saturation of the external active and reactive power controllers to enable a smooth transition from grid-connected to islanded mode, where only inner droop controllers are enabled. In Fig. 3.1 there is a schematic representation of such local controller for DERs: $K_p(s)$ and $K_q(s)$ control ω_p and V_q respectively to track an active p_{ref} and a reactive q_{ref} power reference in grid-connected mode. The regulators $K_p(s)$ and $K_q(s)$ saturate in islanded operation enabling inner droop controllers in order to set ω_{ref} and V_{ref}.

In the continuation of this Chapter, an analysis that extends the work reported in [116] in terms of controller design procedure, detailed RT simulation

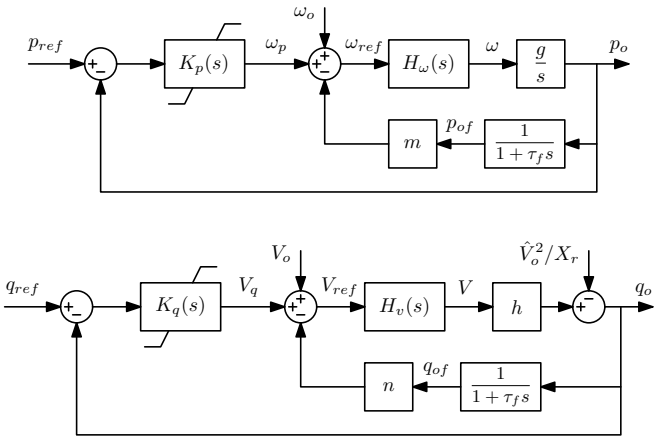

Figure 3.1: Controller proposed in [116]

and small-signal analysis is presented.

3.2 Control structure

The considered controller enables a seamless transition from grid-connected to islanded mode without requiring communication capabilities within the microgrid. However, a non-critical communication channel is needed for the resynchronization of the microgrid, i.e. the transition from autonomous to grid-connected mode. The application scenario could be a microgrid having few grid-forming DERs equipped with this controller and several loads and other DERs, for example PVs, acting as grid-following devices, e.g. as in Fig. 1.3.

The proposed regulator acts on a grid-forming device (Sec. 1.1.1) both in islanded and grid-connected operating modes. In describing this extension for droop controller, the electric cables of the microgrid are supposed to have a dominant inductive behavior, even if in LV microgrids this is usually not true. This assumption is done in order to exploit the basic P/f and Q/V droop control (1.8) as a starting point to manage the islanded operation. In Sec. 3.6 this aspect is investigated considering what happens if the grid has cables with low reactance to resistance ratio.

The extension of the basic droop control consists of two outer regulation loops that set p_s and q_s values in (1.8) to track the DER active and reactive

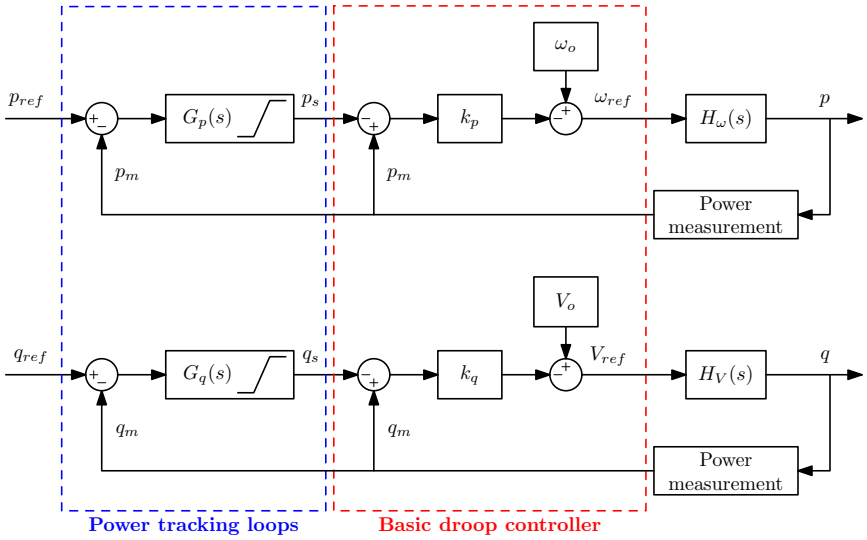

Figure 3.2: Schematic of the proposed extension for the basic droop regulator [100]

power references in grid-connected mode [116]. The solution is depicted in Fig. 3.2: $H_\omega(s)$ indicates generically the transfer function between the frequency reference ω_{ref} of the inverter and its output active power p, and $H_V(s)$ between the voltage amplitude reference V_{ref} and the output reactive power q. In grid-connected mode, as the frequency is imposed by the main grid, $G_p(s)$ varies p_s to move the P/f droop characteristic (1.8a) to ensure $p_m = p_{ref}$ under steady-state conditions. Similarly, $G_q(s)$ varies q_s to move the Q/V droop characteristic defined in (1.8b) to ensure $q_m = q_{ref}$.

In islanded mode, the DER active and reactive powers do not match the reference terms, i.e. $p_m \neq p_{ref}$ and $q_m \neq q_{ref}$, since a power balance has to exist. Then, the outputs of the external power regulators $G_p(s)$ and $G_q(s)$ reach their limits $p_{s,max}$ or $p_{s,min}$ and $q_{s,max}$ or $q_{s,min}$. Being p_s and q_s constant, the controller exploits all the properties of the basic droop control to share the active and reactive load power in islanded mode, as seen in Sec. 1.1.2.

3.3 Controller design

The main controller parameters are:

1. k_p and k_q of the basic droop regulation scheme
2. saturation levels $p_{s,max}$, $p_{s,min}$, $q_{s,max}$, and $q_{s,min}$
3. power controllers $G_p(s)$ and $G_q(s)$

3.3.1 Basic droop regulation scheme

When the grid works in islanded operation, the external controllers have saturated outputs. Thus, the controller scheme is reduced to a basic droop regulator and the droop coefficients, k_p and k_q, can be designed using different procedures proposed in literature [18, 19]. However, several works that study droop control for intentional islanded operation lack of a rigorous approach to the system stability problem, in particular for grid with several DERs. Mathematical models of the system are sometimes too detailed to design controllers [117, 118], or too difficult to be created [27] or too simplified to analyze the interaction of several DERs within the same microgrid [35, 105]. So one open-issue in droop control with a large number of DERs is the microgrid stability [27, 119].

For these reasons, Appendix A describes a generalized method to model a grid with a generic number of inverters without increasing the complexity of the analysis. This method enables a powerful tool for the design of droop controllers in networks of arbitrary complexity and size. In this Chapter, this method is exploited in order to design the coefficients k_p and k_q of the inner droop controller, even though the microgrid herein considered is limited in size for sake of validation.

3.3.2 Saturation levels

Define $S_{nom} > 0$ as the maximum active power that the inverter can generate or absorb (i.e. $p_{max} = S_{nom}$, $p_{min} = -S_{nom}$). In the case there is not any energy storage elements in the DER, the following analysis can be rearranged using $p_{min} = 0$. From (1.8a) and for constant p_s, the angular frequency variation ω_d along the droop characteristic (1.8a) can be written as:

$$\omega_d \triangleq \omega_{ref}\Big|_{p_m=-S_{nom}} - \omega_{ref}\Big|_{p_m=S_{nom}} = 2k_pS_{nom} \tag{3.1}$$

For simplicity, assume that the angular frequency of the mains can vary in the symmetric range

$$\omega_{grid} \in \left[\omega_o - \frac{\omega_g}{2}, \omega_o + \frac{\omega_g}{2}\right] \tag{3.2}$$

with respect to the nominal line frequency ω_o and define x_p as:

$$x_p \triangleq \frac{\omega_d}{\omega_g} \tag{3.3}$$

Notice that this analysis can be extended also for an asymmetric frequency range, instead of (3.2). Thus, from (3.1) and (3.3), x_p is given by:

$$x_p = \frac{2k_p S_{nom}}{\omega_g} \tag{3.4}$$

In grid-connected operation, the steady-state frequency is imposed by the main grid, i.e. $\omega_{ref} = \omega_{grid}$ supposing null tracking error in the regulator. Evaluating p_s from (1.8a) and considering that p_s is maximum at maximum generated active power, i.e. $p_m = S_{nom}$, and for maximum grid-connected angular frequency $\omega_{ref} = \omega_o + \omega_g/2$, it follows:

$$p_{s,max} = S_{nom} + \frac{\omega_g}{2k_p} \tag{3.5}$$

Similarly, the minimum for p_s is:

$$p_{s,min} = -S_{nom} - \frac{\omega_g}{2k_p} \tag{3.6}$$

From (3.1), (3.5) and (3.6), it follows that:

$$p_{s,max} = -p_{s,min} = S_{nom}\left(1 + \frac{1}{x_p}\right) \tag{3.7}$$

Equation (3.7) shows how to tune the saturation levels for the proposed power regulator for the P/f loop. This range of p_s is required to track an active power reference that is included between $-S_{nom}$ and S_{nom} in the whole interval of allowed frequencies (3.2) of the main grid.

Observing (1.8a), the minimum frequency reference is obtained for $p_m = S_{nom}$ and $p_s = p_{s,min}$ and the maximum frequency reference for $p_m = -S_{nom}$ and $p_s = p_{s,max}$. Subtracting these two frequency values, the total frequency reference variation ω_t is:

$$\omega_t = \omega_g + 2x_p\omega_g = \omega_g\left(1 + 2x_p\right) > \omega_g \tag{3.8}$$

The design of $q_{s,max}$, and $q_{s,min}$ is obtained with a similar reasoning on the Q/V loop and with analogous definitions:

$$V_d \triangleq 2k_q S_{nom} \tag{3.9a}$$

$$x_q \triangleq \frac{2k_q S_{nom}}{V_g} \tag{3.9b}$$

With this range of voltage amplitude for grid connected operation

$$V_{grid} \in \left[V_o - \frac{V_g}{2},\, V_o + \frac{V_g}{2}\right] \tag{3.10}$$

it results:

$$q_{s,max} = -q_{s,min} = S_{nom}\left(1 + \frac{1}{x_q}\right) \tag{3.11}$$

and the total amplitude reference variation V_t is:

$$V_t = V_g + 2x_q V_g = V_g\left(1 + 2x_q\right) > V_g \tag{3.12}$$

However, the analysis for the Q/V loop is not as precise as that of the P/f loop, because the voltage amplitude is not constant in all the nodes of the microgrid [20]. For this reason, it could be necessary to increase the saturation levels in (3.11).

3.3.3 Power controllers

In order to design $G_p(s)$ and $G_q(s)$ which determine the dynamic response of the system in grid-connected mode, a simplified small-signal stability analysis is used. In general terms, the dynamic model of a microgrid with several

DERs is complex due to the potential interactions among DERs. In order to simplify the approach, assume that the PCC short circuit power of the utility grid is high (for example, greater than $15 \div 20$ times the DER rated power), so that the grid frequency and the amplitude is dominantly imposed by the utility grid. Under this assumption, the dynamic behavior of different DERs is decoupled by the PCC and the design of the external power loops can be performed assuming one DER connected at the PCC. A detailed simulation of the microgrid with several DERs is then needed to verify the system dynamic behavior.

The active p and reactive q power flow equations for a generic line are described in (1.3). Supposing that the DER is connected at the node with voltage $\mathbf{v}_1$ and the PCC is at the node with voltage $\mathbf{v}_2$, equations (1.3) can be linearized in function of φ and V_1 (the voltage $\mathbf{v}_2$ imposed by the mains is supposed to be fixed). The linearization gives:

$$\begin{bmatrix} \Delta p \\ \Delta q \end{bmatrix} = \underbrace{\begin{bmatrix} \frac{V_1 V_2}{2Z} \sin(\varphi + \theta) & \frac{V_1}{Z} \cos\theta - \frac{V_2}{2Z} \cos(\varphi + \theta) \\ -\frac{V_1 V_2}{2Z} \cos(\varphi + \theta) & \frac{V_1}{Z} \sin\theta - \frac{V_2}{2Z} \sin(\varphi + \theta) \end{bmatrix}}_{\triangleq L} \begin{bmatrix} \Delta\varphi \\ \Delta V \end{bmatrix} \tag{3.13}$$

where in the matrix $L \in \mathbb{R}^{2\times 2}$ there are the operating point quantities.

In Fig. 3.2, a low-pass filtering action is required to evaluate the inverter output powers p_m and q_m. Following [13, 19, 117], a first-order filter is adopted to model both active and reactive power measurements:

$$\frac{\mathrm{d}}{\mathrm{d}t} \begin{bmatrix} \Delta p_m \\ \Delta q_m \end{bmatrix} = -\omega_c \begin{bmatrix} \Delta p_m \\ \Delta q_m \end{bmatrix} + \omega_c \begin{bmatrix} \Delta p \\ \Delta q \end{bmatrix} \tag{3.14}$$

where ω_c is the bandwidth of the first-order filters.

Neglecting the dynamics of the inner voltage and current loops, the inverter is approximated as an ideal generator that precisely tracks its references, i.e.:

$$\frac{\mathrm{d}}{\mathrm{d}t}\Delta\varphi = \Delta\omega_{ref} \tag{3.15a}$$

$$\Delta V = \Delta V_{ref} \tag{3.15b}$$

Merging (3.13)-(3.15), the following state-space model is obtained:

$$\frac{\mathrm{d}}{\mathrm{d}t}\begin{bmatrix}\Delta p_m\\ \Delta q_m\\ \Delta\varphi\end{bmatrix} = \omega_c \left[\begin{array}{cc|c} -1 & 0 & L_1 \\ 0 & -1 & \\ \hline 0 & 0 & 0 \end{array}\right] \begin{bmatrix}\Delta p_m\\ \Delta q_m\\ \Delta\varphi\end{bmatrix} + \left[\begin{array}{c|c} 0 & \omega_c L_2 \\ 0 & \\ \hline 1 & 0 \end{array}\right] \begin{bmatrix}\Delta\omega_{ref}\\ \Delta V_{ref}\end{bmatrix} \tag{3.16}$$

where $L_1\,, L_2 \in \mathbb{R}^{2\times 1}$ are respectively the first and the second column of the matrix L in (3.13). In (3.16), Δp_m and Δq_m are the outputs of the state-space model and $\Delta\omega_{ref}$ and ΔV_{ref} are the two inputs.

Once the dynamic model of the process to be controlled is available, several textbook methods can be used to design $G_p(s)$ and $G_q(s)$ parameters and structures. For the purpose of explanation, pure integrators are here considered, i.e.:

$$G_p(s) = \frac{h_p}{s} \tag{3.17a}$$

$$G_q(s) = \frac{h_q}{s} \tag{3.17b}$$

This analysis can be extended to other types of more well-performing controllers such those reported in [116, 120].

Including (1.8) and (3.17), the following state-space model, which has two states Δp_s and Δq_s, two inputs Δp_m and Δq_m, and two outputs $\Delta\omega_{ref}$ and ΔV_{ref}, is obtained:

$$\begin{cases} \dfrac{\mathrm{d}}{\mathrm{d}t}\Delta p_s &= -h_p\Delta p_m \\ \dfrac{\mathrm{d}}{\mathrm{d}t}\Delta q_s &= -h_q\Delta q_m \\ \Delta\omega_{ref} &= -k_p\Delta p_m + k_p\Delta p_s \\ \Delta V_{ref} &= -k_q\Delta q_m + k_q\Delta q_s \end{cases} \tag{3.18}$$

Merging the model (3.16) and the regulator model (3.18), the state-space model of the entire controlled system can be obtained and its stability can be analyzed,

for example, using the eigenvalue analysis.

It is worth highlighting this analysis is carried out in grid-connected operation, enabling the determination of the speed of response and system damping in this operating mode. However, the power loop controllers operate also during the transients in islanded operation and in these conditions their dynamic behavior changes. Thus, time domain simulations are needed to verify the performances during the transition to the islanded mode.

3.3.4 Power sharing in islanded condition

The power sharing in islanded condition can be achieved only if the external controllers of the inverters saturate at the same level or, with other words, the droop characteristics do not have a relative offset. In order to analyze this phenomenon, consider two DERs that have the same saturation levels of the external controllers and the same power rating S_{nom} and focus this analysis on the P/f loop. This analysis considers the steady-state solution in islanded mode, where the generated powers of inverter 1 p_1 and inverter 2 p_2 balance the load power p_L, i.e. $p_1 + p_2 = p_L$. Inverter 1 is also identified as the one with the smaller active power reference p_{ref1} and inverter 2 as that with the larger one p_{ref2} ($p_{ref1} < p_{ref2}$), with no loss of generality. From Fig. 3.2, define the input error of the external regulator as $\varepsilon_p \triangleq p_{ref} - p_m$.

In islanded operation only one of these four conditions is verified:

1. the external controllers of the two inverters are saturated at different levels, for instance $p_{s,1} = p_{s,min}$ and $p_{s,2} = p_{s,max}$
2. the two external controllers are not saturated, that is $p_{s,min} < p_{s,1} < p_{s,max}$ and $p_{s,min} < p_{s,2} < p_{s,max}$
3. the two external controllers are saturated at the same level, that is $p_{s,1} = p_{s,2} = p_{s,min}$ or $p_{s,1} = p_{s,2} = p_{s,max}$
4. one external regulator is saturated while the other is not

Condition 1 can never occur, since in this situation the intersection of the droop characteristics is not compatible with the power ratings of the two inverters.

Condition 2 is highly unlikely to occur, because in this situation the two input errors $\varepsilon_{p,1}$ and $\varepsilon_{p,2}$ for the external controllers have to be zero, that means that $p_{ref1} = p_1$ and $p_{ref2} = p_2$. Thus, this condition can be maintained only if $p_{ref1} + p_{ref2} = p_L$.

When condition 3 is true, the droop characteristics (1.8a) of the two inverters are equal, and so in this situation the active power sharing is achieved, i.e. $p_1 = p_2$. Since input error ε_p is positive when the controller saturates at $p_{s,max}$ and negative when it saturates at $p_{s,min}$, it is possible to show that:

$$\frac{p_L}{2} \leq p_{ref1} < p_{ref2} \quad \vee \quad p_{ref1} < p_{ref2} \leq \frac{p_L}{2} \tag{3.19}$$

In condition 4, one of the two errors $\varepsilon_{p,1}$ and $\varepsilon_{p,2}$ is zero. If, for instance, $\varepsilon_{p,1} = 0$, then inverter 2 is saturated at either $p_{s,max}$ or $p_{s,min}$. If saturated at $p_{s,max}$, it is possible to show that:

$$p_{ref1} < \frac{p_L}{2} < p_{ref2} \tag{3.20}$$

The saturation at $p_{s,min}$ is instead impossible as it would imply $p_{ref1} > p_{ref2}$, which is a contradiction with the initial hypothesis.

Summarizing this analysis, condition 3 implies (3.19) and condition 4 implies (3.20). With (3.19) the power sharing is achieved, while with (3.20) one external controller works in the linear operating mode tracking its power reference, while the other has a saturated output p_s and then its inverter supplies the remaining part of the load power.

The analysis of this section is for the P/f loop, but similar considerations can be done for the Q/V loop. In this case, however, the analysis is less accurate since the voltage amplitude is not the same for the two DERs.

3.4 Application example

The test-case of Fig. 3.3 is considered to show the design procedure and to validate the analysis via an HIL-RT simulation approach. This test-case is single-phase with nominal voltage $V_o = 230\sqrt{2}\,\mathrm{V}$ and nominal frequency

Table 3.1: Test-case parameters

L_o	=	$1.2\,\mathrm{mH}$	C_o	=	$10\,\mu\mathrm{F}$
R_{L1}	=	$152\,\mathrm{m}\Omega$	$L_{C1}+L_{L1}$	=	$2.8\,\mathrm{mH}$
R_{L2}	=	$106\,\mathrm{m}\Omega$	$L_{C2}+L_{L2}$	=	$1.9\,\mathrm{mH}$
R_G	=	$24.9\,\mathrm{m}\Omega$	L_G	=	$556\,\mu\mathrm{H}$
L_L	=	$4\,\mathrm{mH}$	C_L	=	$10\,\mu\mathrm{F}$
R_L	=	$22\,\Omega$	ω_c	=	$2\pi 5\,\mathrm{rad/s}$
k_p	=	$1.6\cdot 10^{-4}$	k_q	=	$2.2\cdot 10^{-3}$
h_p	=	3	h_q	=	15
$p_{s,max}$	=	$23\cdot 10^3$	$q_{s,max}$	=	$18\cdot 10^3$

$f_o = \omega_o/(2\pi) = 50\,\mathrm{Hz}$, where there are two DERs with a rated power of $S_{nom} = 3\,\mathrm{kVA}$ that can provide or absorb an active power up to S_{nom}. Table 3.1 summarizes the main parameters of the test-case.

The droop coefficients of the two inverters are set to be equal, i.e.:

$$k_{p1} = k_{p2} \triangleq k_p \tag{3.21a}$$

$$k_{q1} = k_{q2} \triangleq k_q \tag{3.21b}$$

thus allowing 1:1 load power sharing in islanded mode of operation (Sec. 1.1.2). Parameters (3.21) can be designed taking into account the maximum frequency ω_g and voltage amplitude V_g variations, as in [18, 117], and the desired system damping. In the case here considered, the second condition is the more restrictive one and, using the small-signal stability analysis of Appendix A, coefficients (3.21) are chosen to impose a damping factor for the complex eigenvalues of $\xi = 0.84$, obtaining $k_p = 1.6\cdot 10^{-4}$ and $k_q = 2.2\cdot 10^{-3}$. Moreover, the slowest poles are a complex-conjugate eigenvalue couple with a resonance frequency of $\omega_n = 18.5\,\mathrm{rad/s}$ and a damping factor of $\xi = 0.84$. The resulting eigenvalues in islanded mode are shown in Fig. 3.4.

Assuming that the frequency and the amplitude of grid voltage vary in the

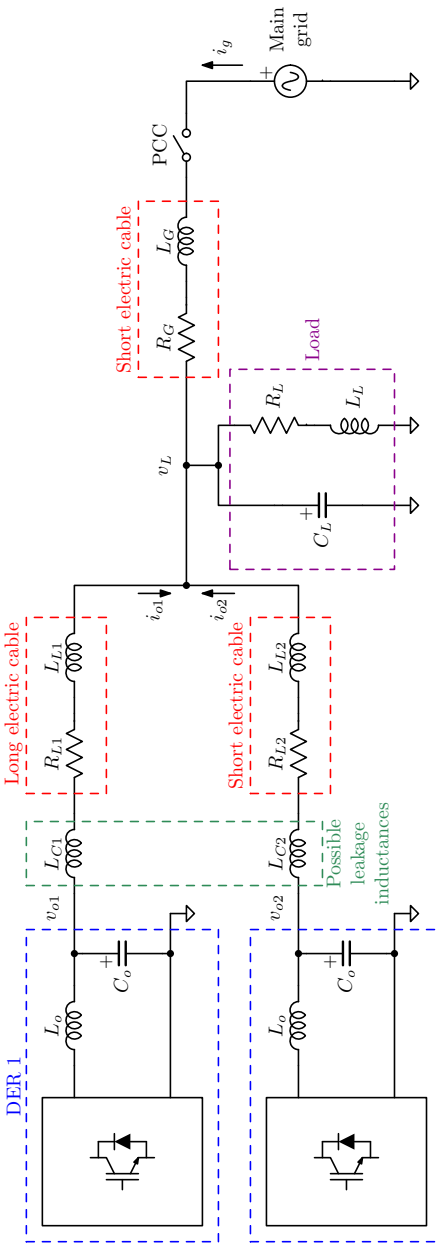

Figure 3.3: Considered test-case [100]

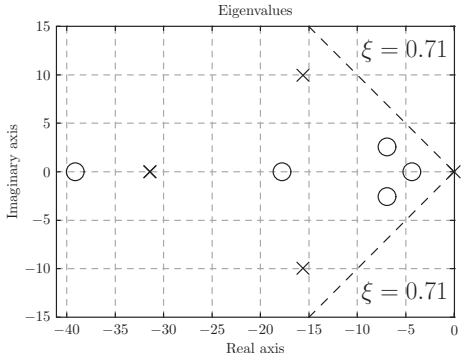

Figure 3.4: Eigenvalues of the system in islanded operation (crosses) and in grid-connected operation (circles)

following ranges:

$$f_{grid} : \quad (1 \pm 1\%)\, f_o \quad \Rightarrow \; 49.5\,\mathrm{Hz} \div 50.5\,\mathrm{Hz} \tag{3.22a}$$

$$V_{grid} : \quad (1 \pm 10\%)\, V_o \; \Rightarrow \; 292.7\,\mathrm{V} \div 357.8\,\mathrm{V} \tag{3.22b}$$

the saturation levels can be determined using the approach of Sec. 3.3.2, obtaining $p_{s,max} = -p_{s,min} = 23\,\mathrm{kW}$ and $q_{s,max} = -q_{s,min} = 18\,\mathrm{kVAR}$.

Finally, the external regulators (3.17) of the two DERs are set equal for both active and reactive power control loops, i.e.:

$$h_{p1} = h_{p2} \triangleq h_p \tag{3.23a}$$

$$h_{q1} = h_{q2} \triangleq h_q \tag{3.23b}$$

since the two inverters are equal. Using the small-signal stability analysis described in Sec. 3.3.3, parameters h_p and h_q can be chosen as a trade-off between stability margin and speed of response in grid-connected mode, obtaining $h_p = 3$ and $h_q = 15$. The eigenvalues of the system in grid-connected mode are shown in Fig. 3.4: the slowest real pole has a frequency of $4.36\,\mathrm{rad/s}$ and then there is a couple of complex-conjugate poles with resonance frequency of $\omega_n = 7.4\,\mathrm{rad/s}$ and damping factor of $\xi = 0.94$.

3.5 Real-time simulation results

The first phase of design and validation of the controller was done using Matlab/Simulink, while HIL-RT approach was used to develop the final regulator and to validate its operation in a more realistic situation. An accurate model of the inverters and of the grid is simulated in the FPGA target of a National Instruments (NI) cRIO 9014 platform [121]. This model is a discrete time description of the output LC filters of the inverters, the RL power lines, the load, and the grid-connection, as Fig. 3.5 shows. The discretization time is $100\,\mathrm{ns}$. The Pulse-Width Modulation (PWM), the inverter current and voltage regulators, and the proposed droop controllers are implemented in the FPGA targets of two NI GPICs [121]. NI cRIO and NI GPICs can interact because NI cRIO has some analog output ports that generate the signals that correspond to the inductor currents, the output voltages, and the output currents of the inverters. These analog quantities are sampled by the input analog ports of the NI GPIC which calculates the gate commands to modulate the inverters. Gate commands are given by the NI GPIC thanks to its output digital ports and they are read by the input digital ports of the NI cRIO platform. The basic scheme of the RT simulation setup is shown in Fig. 3.5. More details on this modeling and validation approach are in [62].

Figs. 3.6-3.9 report the RT simulation results for grid-connected operation and Fig. 3.10 the corresponding operating points of these simulations on the static droop characteristics. The operating point is indicated by the same letter in the Figs. 3.6-3.9 and Fig. 3.10. These figures show that the regulator can track its active and reactive power references in the range of frequency that is selected in the design phase, i.e. (3.22a). Figs. 3.6 and 3.7 show two DERs tracking null active and reactive power references at the minimum and maximum frequencies of the grid voltage respectively, i.e. $49.5\,\mathrm{Hz}$ and $50.5\,\mathrm{Hz}$. These two cases validate the choice of the saturation levels of the regulator $G_p(s)$. It is possible to observe that the output current of inverter 1 is almost zero in both cases.

The simulations of step variations of the active and reactive power references of the inverter 1 are reported in Figs. 3.8 (active power reference variation

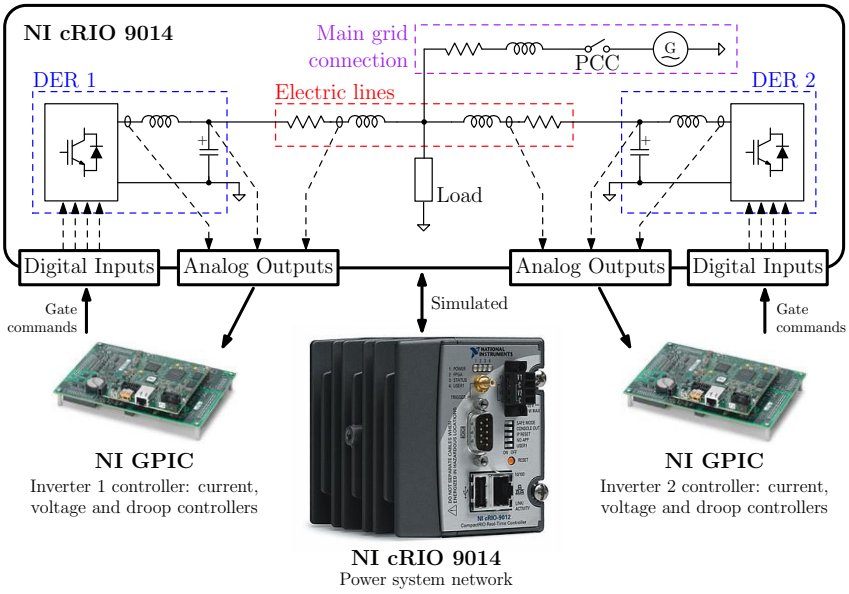

Figure 3.5: RT-HIL platform organization [100]

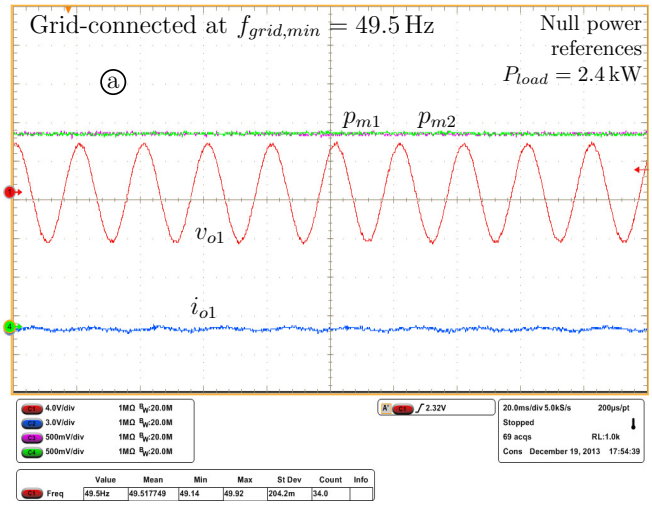

Figure 3.6: RT simulation results of steady-state grid-connected operating mode at $f_{grid,min}$: output voltage of inverter 1, v_{o1}, in CH1 (256 V/div); output current of inverter 1, i_{o1}, in CH2 (12 A/div); measured active power of inverter 1, p_{m1}, in CH3 (1024 W/div) and measured active power of inverter 2, p_{m2}, in CH4 (1024 W/div); time with 20 ms/div [100]

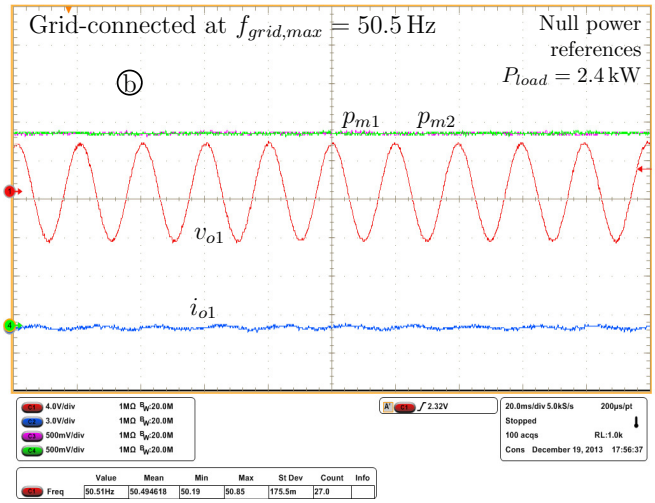

Figure 3.7: RT simulation results of steady-state grid-connected operating mode at $f_{grid,max}$: output voltage of inverter 1, v_{o1}, in CH1 (256 V/div); output current of inverter 1, i_{o1}, in CH2 (12 A/div); measured active power of inverter 1, p_{m1}, in CH3 (1024 W/div) and measured active power of inverter 2, p_{m2}, in CH4 (1024 W/div); time with 20 ms/div [100]

from 0 W to 2 kW) and 3.9 (reactive power reference variation from 0 VAR to 1 kVAR). The rise time is about 210 ms for both transients of Figs. 3.8 and 3.9. In all these cases, the resistive load R_L has a nominal power of 2.4 kW.

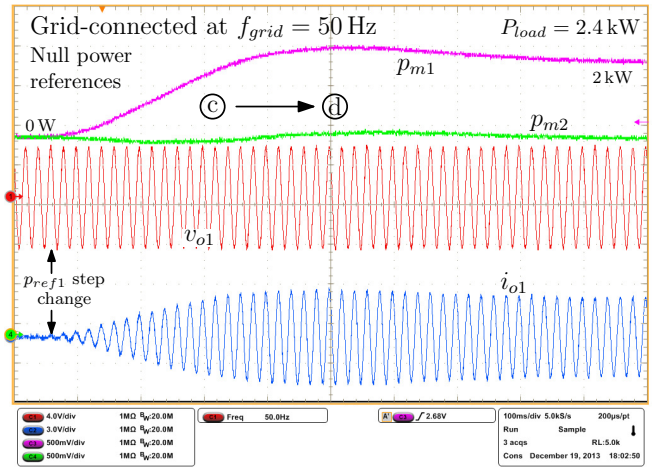

Figure 3.8: RT simulation results of p_{ref1} step variation in grid-connected operating mode: output voltage of inverter 1, v_{o1}, in CH1 ($256\,\mathrm{V/div}$); output current of inverter 1, i_{o1}, in CH2 ($12\,\mathrm{A/div}$); measured active power of inverter 1, p_{m1}, in CH3 ($1024\,\mathrm{W/div}$) and measured active power of inverter 2, p_{m2}, in CH4 ($1024\,\mathrm{W/div}$); time with $100\,\mathrm{ms/div}$ [100]

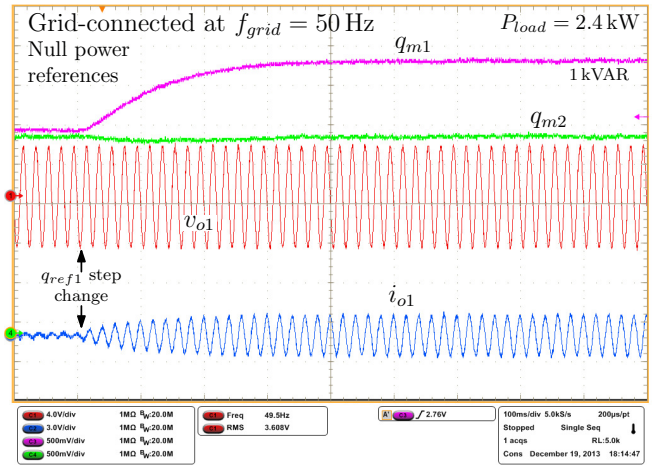

Figure 3.9: RT simulation results of q_{ref1} step variation in grid-connected operating mode: output voltage of inverter 1, v_{o1}, in CH1 ($256\,\mathrm{V/div}$); output current of inverter 1, i_{o1}, in CH2 ($12\,\mathrm{A/div}$); measured reactive power of inverter 1, q_{m1}, in CH3 ($512\,\mathrm{VAR/div}$) and measured reactive power of inverter 2, q_{m2}, in CH4 ($512\,\mathrm{W/div}$); time with $100\,\mathrm{ms/div}$ [100]

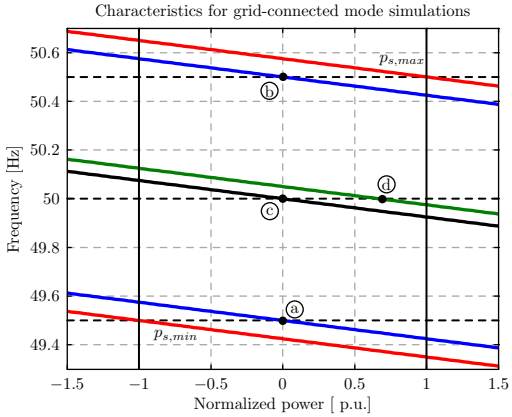

Figure 3.10: Static characteristics of grid-connected mode simulations [100]

Figs. 3.11-3.14 show the results for islanded operation and for the disconnection of the main grid and Fig. 3.15 the operating points of the corresponding conditions on the static droop characteristics. The same operating point is indicated by the same letter in Figs. 3.11-3.14 and in Fig. 3.15. The transition from grid-connected to islanded operation is shown in Fig. 3.11. Zero active and reactive powers are generated by the two inverters before the disconnection and, after the transient, the load power is shared between the two energy sources, because (3.19) is satisfied. It is possible to observe that the controller can achieve a smooth transition and that the frequency of the microgrid varies during this transient because the integral controllers saturate at $p_{s,min}$. A step variation of the load resistance in islanded mode is reported in Fig. 3.12, showing the transient time of about $70\,\mathrm{ms}$. In Fig. 3.13 there is a similar simulation that shows the power sharing failure. In this case, the relation (3.20) is satisfied after the transient and the two inverters do not share the load properly, but one inverter is still tracking its power reference. In Fig. 3.14, the failure of the power sharing is shown in a different way: the two inverters are working in grid-connected mode with opposite power references ($\pm 3\,\mathrm{kW}$) and then a main grid disconnection occurs. In this case, one inverter is absorbing an active power up to its rated power in order to show the worst case where the power sharing is not achieved. Indeed, in islanded operation the two inverters continue to provide active powers that are close to their references: inverter 1 is still tracking its reference, while inverter 2 is balancing the power that is required by the load.

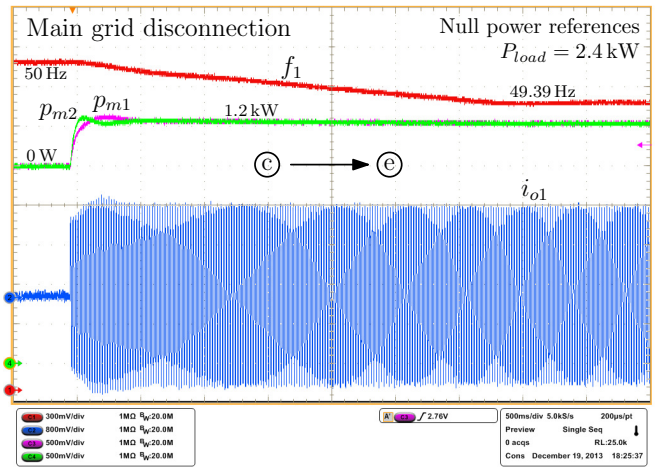

Figure 3.11: RT simulation results of grid transition: frequency of the output voltage of inverter 1 v_{o1}, f_1, in CH1 ($0.6\,\mathrm{Hz/div}$); output current of inverter 1, i_{o1}, in CH2 ($3.2\,\mathrm{A/div}$); measured active power of inverter 1, p_{m1}, in CH3 ($1024\,\mathrm{W/div}$); measured active power of inverter 2, p_{m2}, in CH4 ($1024\,\mathrm{W/div}$); time with $500\,\mathrm{ms/div}$ [100]

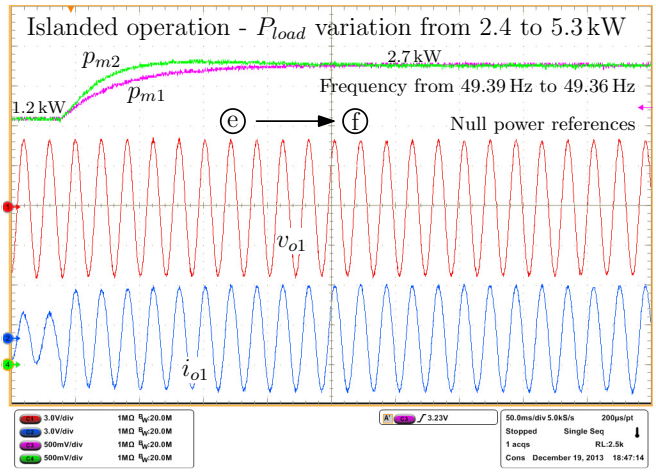

Figure 3.12: RT simulation results of load step variation in islanded operating mode: output voltage of inverter 1, v_{o1}, in CH1 ($192\,\mathrm{V/div}$); output current of inverter 1, i_{o1}, in CH2 ($12\,\mathrm{A/div}$); measured active power of inverter 1, p_{m1}, in CH3 ($1024\,\mathrm{W/div}$); measured active power of inverter 2, p_{m2}, in CH4 ($1024\,\mathrm{W/div}$); time with $50\,\mathrm{ms/div}$ [100]

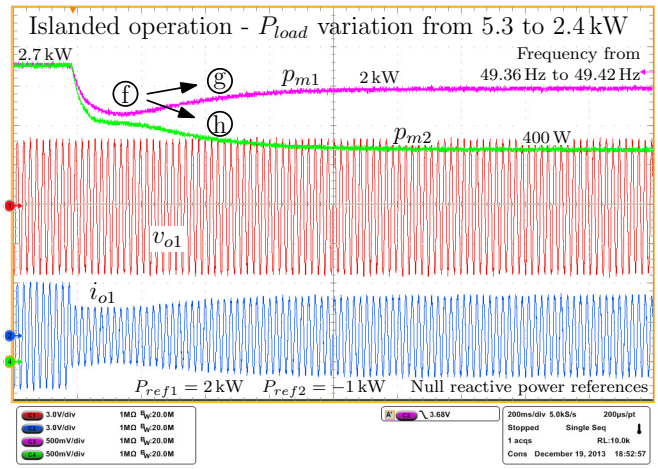

Figure 3.13: RT simulation results of load step variation in islanded operating mode: output voltage of inverter 1, v_{o1}, in CH1 (192 V/div); output current of inverter 1, i_{o1}, in CH2 (12 A/div); measured active power of inverter 1, p_{m1}, in CH3 (1024 W/div); measured active power of inverter 2, p_{m2}, in CH4 (1024 W/div); time with 200 ms/div [100]

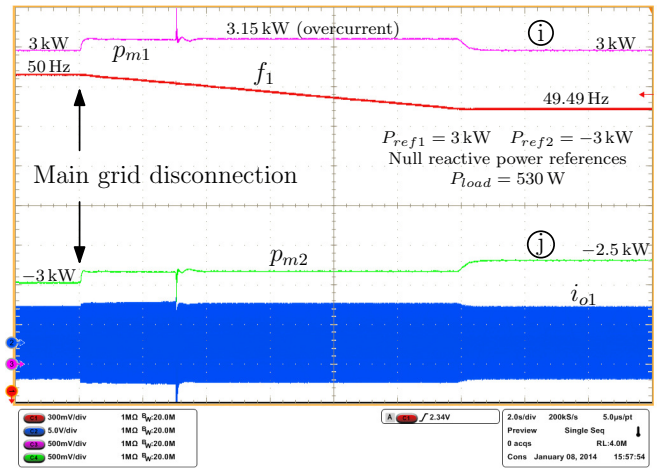

Figure 3.14: RT simulation results of grid transition: frequency of the output voltage of inverter 1 v_{o1}, f_1, in CH1 (0.6 Hz/div); output current of inverter 1, i_{o1}, in CH2 (20 A/div); measured active power of inverter 1, p_{m1}, in CH3 (1024 W/div); measured active power of inverter 2, p_{m2}, in CH4 (1024 W/div); time with 2 s/div [100]

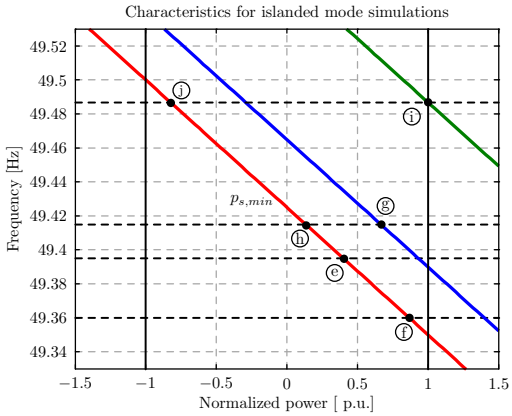

Figure 3.15: Static characteristics of islanded mode simulations [100]

3.6 Further investigations

This section describes the operation of the regulator in some critical conditions, as sudden disconnections of load or sources or the operation in a microgrid with network impedances having low reactance to resistance ratio X/R. The following results are obtained with Matlab/Simulink simulations of the system of Fig. 3.3.

Figs. 3.16-3.19 show the performances of the controller when sudden disconnections of the load or of one inverter occur. In all these four figures, the inverters have null reactive power references and inverter 1 receives an active power reference of $3\,\mathrm{kW}$, while inverter 2 of $-3\,\mathrm{kW}$. This is the worst case for the power sharing, as also tested in Fig. 3.14. The parameters of the RLC load and cables are reported in Tab. 3.1. Fig. 3.16 shows a simulation of a disconnection of the entire RLC load in grid-connected mode, while Fig. 3.17 shows the same simulation in islanded operation. Fig. 3.18 shows a simulation of the disconnection of inverter 2 in grid-connected mode and Fig. 3.19 shows the same simulation in islanded operating mode. These results show that the controller can manage also sudden disconnections of load and of one of the two inverters without significant worsening of system performances.

So far, a microgrid with network impedances that are mainly inductive is considered even if in LV microgrids the ratio X/R is usually small, as seen in Sec. 1.1.2. In this situation, active and reactive powers depend on both voltage amplitude drop and phase shift along the electric lines and the droop control (1.8) may suffer poor performances and potential instabilities [20,30,31]. Some previous works on droop control propose some solutions for this problem (Sec. 1.1.2) and in this section the behavior of the proposed controller is tested in a microgrid with $X/R = 0.5$, using the virtual output impedance technique of [32] (the aim of this Chapter is not proposing a new technique to address this issue). According to [32], the voltage reference of the voltage loop is subtracted by a quantity that is proportional to the time derivative of the output current of the inverter, emulating a virtual output inductance. The sum of the virtual inductance and the actual inductance of the cable has to dominate its resistive component to decouple the power flow dependencies, i.e. the active power flow

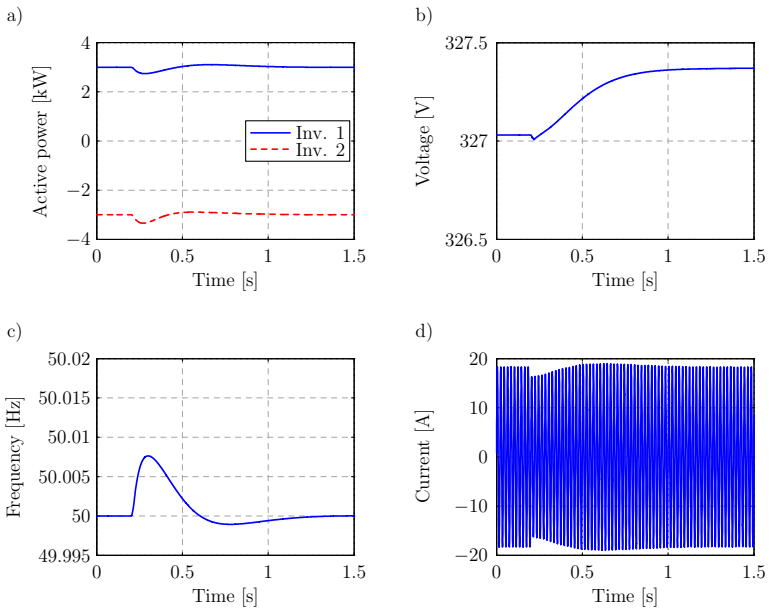

Figure 3.16: Simulation of sudden disconnection of the RLC load in grid-connected mode: a) measurements of output active powers, b) output voltage amplitude of inverter 1, c) frequency reference of the inverter 1, and d) output current of inverter 1

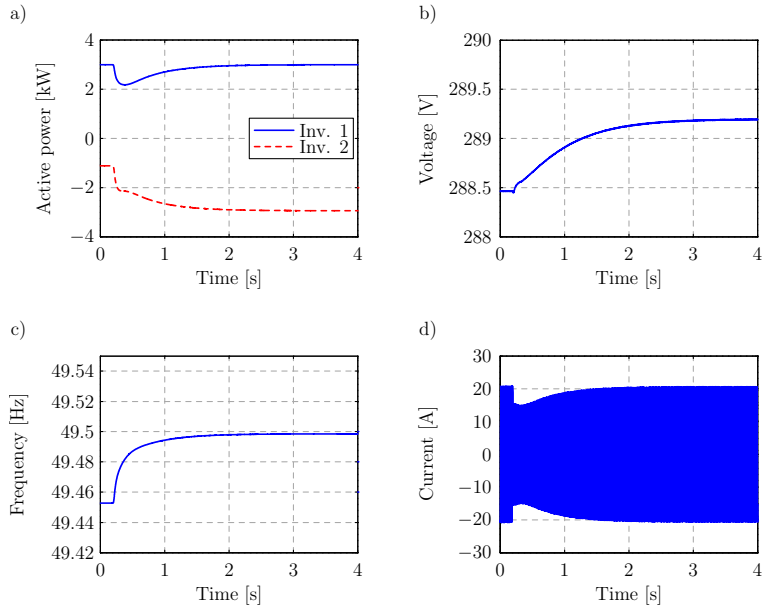

Figure 3.17: Simulation of sudden disconnection of the RLC load in islanded mode: a) measurements of output active powers, b) output voltage amplitude of inverter 1, c) frequency reference of the inverter 1, and d) output current of inverter 1

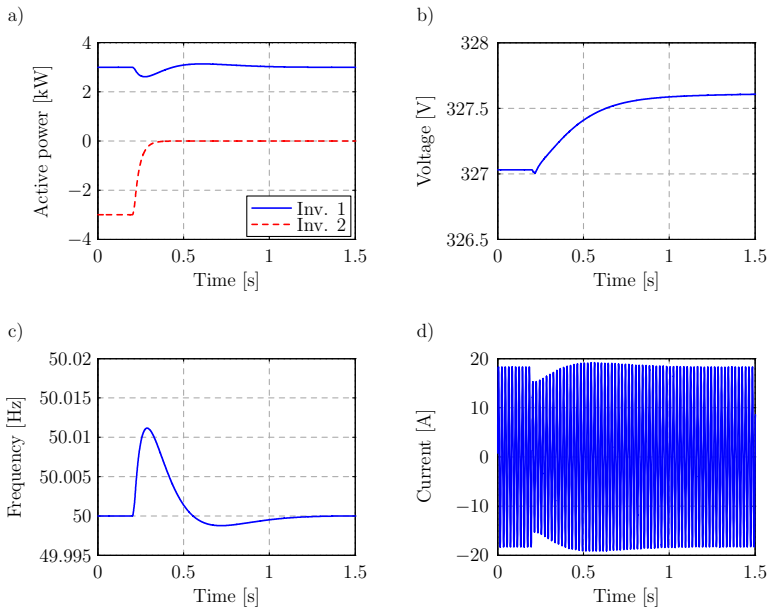

Figure 3.18: Simulation of sudden disconnection of the inverter 2 in grid-connected mode: a) measurements of output active powers, b) output voltage amplitude of inverter 1, c) frequency reference of the inverter 1, and d) output current of inverter 1

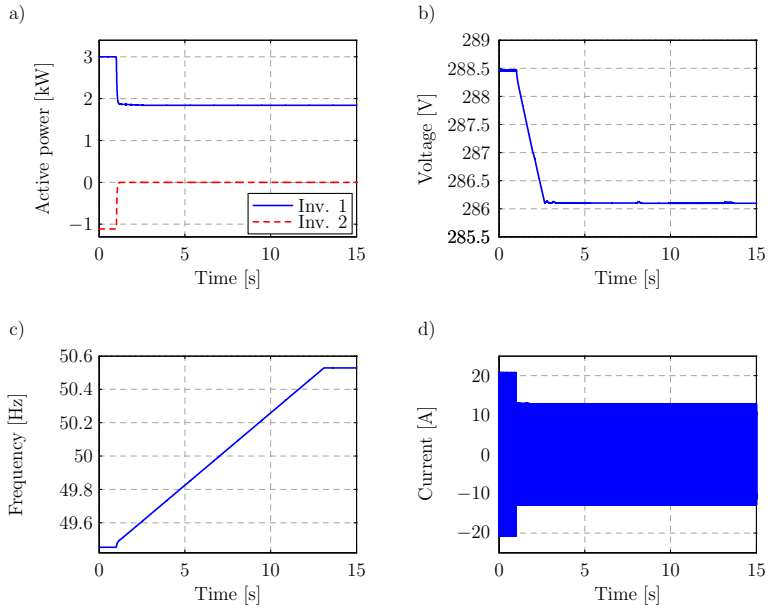

Figure 3.19: Simulation of sudden disconnection of the inverter 2 in islanded mode: a) measurements of output active powers, b) output voltage amplitude of inverter 1, c) frequency reference of the inverter 1, and d) output current of inverter 1

Table 3.2: New parameters for the validations in a microgrid with low X/R

$L_{C1} + L_{L1}$	=	$242\,\mu\mathrm{H}$	$L_{C2} + L_{L2}$	=	$169\ \mu\mathrm{H}$
L_{V1}	=	$2.6\,\mathrm{mH}$	L_{V2}	=	$1.7\,\mathrm{mH}$

still depends on the phase shift and the reactive power flow still depends on the voltage amplitude droop, as for the inductive case of Sec. 1.1.2.

In the following results, two reduced values of $L_{C1}+L_{L1}$ and $L_{C2}+L_{L2}$ are considered to get a X/R ratio of 0.5 for the cables and two virtual inductors for the two inverters (L_{V1} and L_{V2}) are emulated. The new values for the test-case of Fig. 3.3 are reported in Tab. 3.2: all the other parameters of Tab. 3.1 are not changed.

Figs. 3.20-3.23 show the simulation results for the microgrid with the reduced X/R. The simulation starts with zero reactive power references for the two inverters and with an active power reference of $2\,\mathrm{kW}$ for inverter 1 and of $-3\,\mathrm{kW}$ for inverter 2. The parameters of the load are reported in Tab. 3.1, except for the initial value of the load resistance that is $R_L = 100\,\Omega$ ($P_L = 530\,\mathrm{W}$). An active power reference variation is shown in Fig. 3.20: the active power reference of inverter 1 is changed from $2\,\mathrm{kW}$ to $3\,\mathrm{kW}$. After this, a simulation of the transition from grid-connected to islanded operation is presented in Fig. 3.21. Fig. 3.22 shows the step variation of the load resistance from $R_L = 100\,\Omega$ ($P_L = 530\,\mathrm{W}$) to $R_L = 22\,\Omega$ ($P_L = 2.4\,\mathrm{kW}$) in islanded operation. Finally, the sudden disconnection of the entire RLC load is shown in Fig. 3.23. These results show that the proposed controller can also manage a microgrid with low X/R ratio, thanks to the use of the virtual output inductance described in [32], and no particular degradation of the performances of the controller occurs.

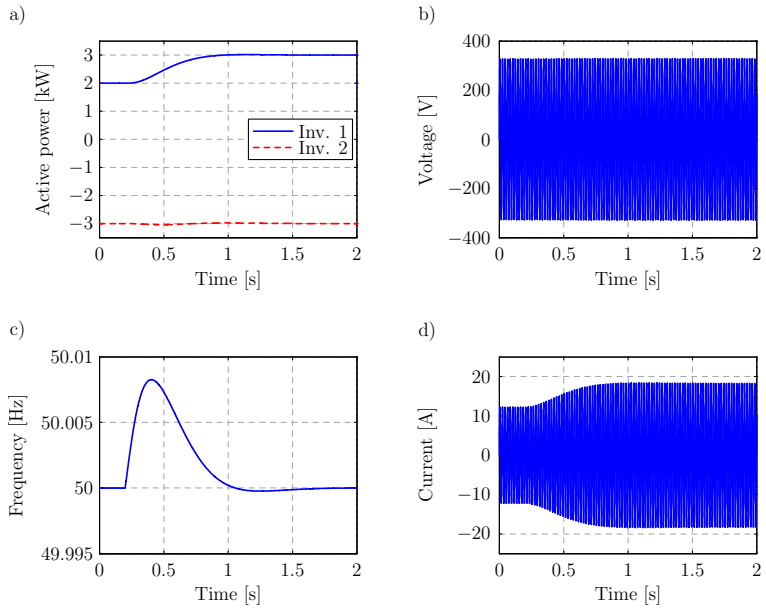

Figure 3.20: Simulation of step variation of the inverter 1 active power reference (from 2 kW to 3 kW) in grid-connected mode for a microgrid with $X/R = 0.5$ cables and virtual output inductance technique [32]: a) measurements of output active powers of the two inverters, b) output voltage of inverter 1, c) frequency reference of the inverter 1, and d) output current of inverter 1

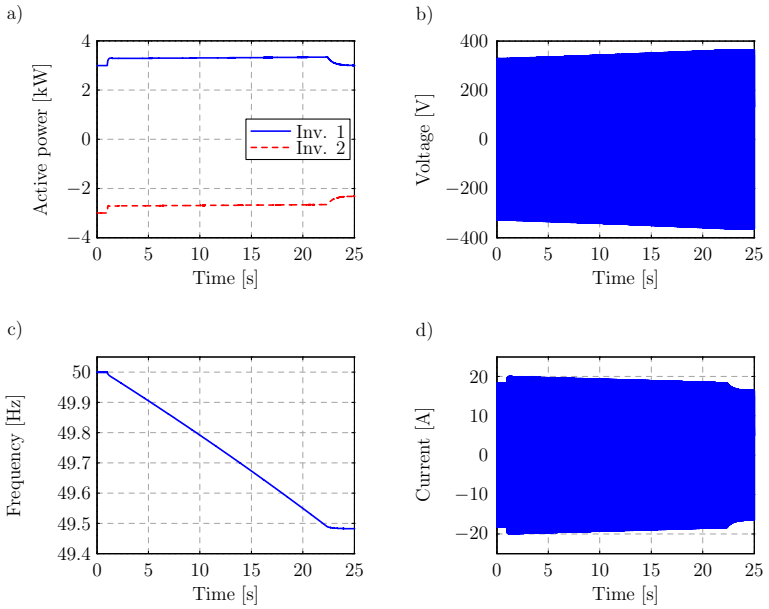

Figure 3.21: Simulation of transition from grid-connected to islanded mode for a microgrid with $X/R = 0.5$ cables and virtual output inductance technique [32]: a) measurements of output active powers of the two inverters, b) output voltage of inverter 1, c) frequency reference of the inverter 1, and d) output current of inverter 1

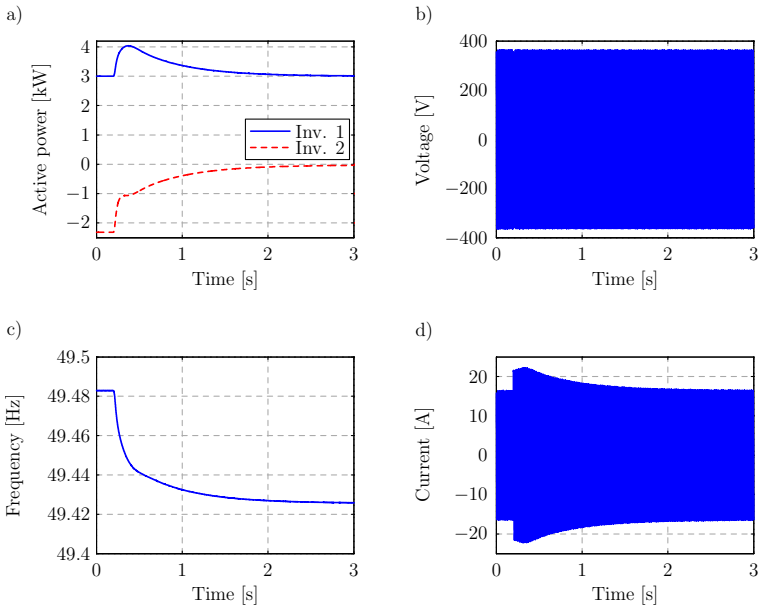

Figure 3.22: Simulation of load variation from $R_L = 100\,\Omega$ ($P_L = 530\,\mathrm{W}$) to $R_L = 22\,\Omega$ ($P_L = 2.4\,\mathrm{kW}$) in islanded mode for a microgrid with $X/R = 0.5$ cables and virtual output inductance technique [32]: a) measurements of output active powers of the two inverters, b) output voltage of inverter 1, c) frequency reference of the inverter 1, and d) output current of inverter 1

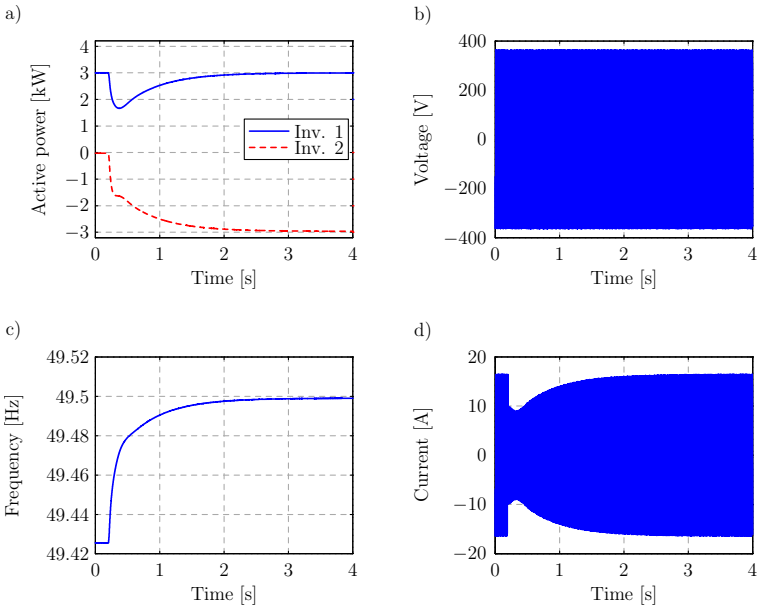

Figure 3.23: Simulation of sudden disconnection of the RLC load in islanded mode for a microgrid with $X/R = 0.5$ cables and virtual output inductance technique [32]: a) measurements of output active powers of the two inverters, b) output voltage of inverter 1, c) frequency reference of the inverter 1, and d) output current of inverter 1

3.7 Summary

A local regulator for electronically interfaced DERs is analyzed to manage a microgrid in both islanded and grid-connected modes in this Chapter in order to improve the reliability of the grid when the mains disconnect. The most relevant feature is the seamless microgrid transition from grid-connected to autonomous mode without any time-critical communication, even if multiple DERs are connected to the microgrid. The controller exploits P/f and Q/V droop control to share the load power in islanded operation and feedback control to track power references in grid-connected operation. The proposed analysis includes the design of saturation levels and a small-signal model to design the power loop controllers. Finally, the solution is implemented in an FPGA device and extensively tested via Hardware-In-the-Loop and Real-Time simulation approaches, verifying the main properties and performances.

Chapter 4

Stability analysis for single-phase AC grids

The interactions of more and more power electronics-interfaced power systems can worsen the power quality and the system stability in distribution networks, as anticipated in Sec. 1.2. System stability can be addressed by analyzing the source and load impedances at the interacting section and well-established approaches exist for DC and three-phase AC networks. Some papers focused also on single-phase AC systems, whose study is generally more difficult due to their time-varying characteristics.

The aims of this Chapter are to describe a method to address the stability of single-phase AC systems and to experimentally verify it, as done in [122]. Sec. 4.1 reviews the state of the art for single-phase system stability analysis. Then, the presented approach is in Sec. 4.2: it bases on dynamic phasors in order to identify a steady-state operation for a single-phase system; then a linearization allows to obtain a small-signal model that is written in terms of 2-dimensional source and load impedances. The system stability is then evaluated using the GNC. Secs. 4.3 and 4.4 describe how to apply this method to a real setup, in terms of system perturbation and measurement. Experimental validations are provided in Sec. 4.6 to verify the feasibility of this approach. In particular, the considered test-case includes a current-controlled inverter synchronized to the grid via a PLL. Sec. 4.5 describes the equivalence of the proposed approach

with the dq impedanced-based method of [55, 65] for balanced three-phase AC systems.

4.1 State of the art

Single-phase AC system studies are more difficult compared to DC and balanced three-phase AC system analyzes because the identification of a precise operating point where to perform a linearization is not straightforward (Sec. 1.2). To study these systems some approximations can be introduced, such as reduced order models (e.g. neglect of DC link dynamics) and harmonic linearization [123–125]. In particular, harmonic linearization provides small-signal description in terms of one-dimensional impedances as for DC systems, rather than MIMO analysis for three-phase AC systems [125, 126].

A completely different approach considers the single-phase AC system as a part of an artificial three-phase system [127, 128]. This enables the use of the dq transformation theory and other analytic frameworks used for three-phase AC systems, for example those in [55,65], also for single-phase systems. Also [129] exploits the dq transformation for single-phase analysis.

Single-phase system stability has been studied so far also for railway system applications [69, 130–133]. The propulsion system in a train consists of a single-phase grid, a single-phase line-connected converter, and a three-phase inverter, so the model includes time-varying and nonlinear terms [131, 132]. In particular, the input admittance criterion (one-dimensional approach), which considers systems that are linear and time-invariant, is studied in [130, 131]. Some methods to address the time-varying behavior of single-phase systems are described in [69], such as linearization along a sinusoidal trajectory (Linear Time Periodic control system theory), Lifting Techniques, etc. Low-frequency instability of railway system is addressed by [132] with some approximations and with a simulation approach in [133].

Linearization along a periodic trajectory is perform in [69, 134, 135] for AC electric systems, exploiting the Linear Time Periodic modeling [136]. This consists of describing the single-phase or three-phase system with a linear state-

space model, whose matrices are periodic, considering that the steady-state operation is AC. This observation enables the use of mathematical tools first developed in [136]: a dynamic model that relates all the Fourier coefficients of a periodic signal to all the coefficients of another one is provided. An example can be the relation between the coefficients of a current signal to the coefficients of a voltage signal at an electric port. This mathematical description is given with a matrix (potentially double infinite-dimensional) called Harmonic Transfer Function [69, 134–136].

Among the different devices in microgrids and distribution grids, the presence of PLL in grid-feeding inverters, for instance for PV applications, can have negative impact on the system stability [129, 137–139]. In particular, the study of this phenomenon for three-phase AC systems with the dq transformation theory shows that the stability is affected because the PLL introduces a negative incremental behavior on the dq impedances, in particular for Z_{qq} [137, 138]. The study of PLL in single-phase connections is generally more difficult for the reasons seen so far. dq space vector representation for single-phase systems can be one approach [127–129]. One-dimensional analysis is used to study PLL effects in three-phase [140] and single-phase systems: in particular [141] compares the stabilizing effects of PLL, such as basic T/4 delayed PLL and Second-Order Generalized Integrator (SOGI) PLL.

This Chapter describes an approach to obtain a small-signal impedance-based model for single-phase AC systems that is equivalent to dq method for three-phase systems. However, rather than using the dq transformation, the frequency-selective averaging technique of [142] is used to identify an operating point for the single-phase system, that is done with approximations in other papers, as [126]. This identification enables a small-signal stability analysis on a well-defined operating point [122]. The obtained small-signal model is MIMO as for three-phase AC systems and it is studied with the GNC [55, 66]. The new contribution of this work, in particular compared to [127, 128], is validating this modeling on a single-phase laboratory-scale setup, that in particular includes PLL for the synchronization of grid-feeding inverters.

4.2 System description and modeling

The dq method for three-phase systems can be extended to single-phase connections, for instance considering the single-phase system as a part of an artificial three-phase system where two phases are shifted respectively of $120°$ and $240°$ with respect to the single-phase system or exploiting an Hilbert filter to generate an orthogonal component to the single-phase one as done in [127,128]: with these methods, the stability analysis can be addressed with the three-phase dq approach, i.e. dq impedances and GNC.

The approach used here, on the other hand, is described in a slightly different way compared to [128], that is the averaging method of [142]. Such approach is equivalent to that used in three-phase systems with the dq transformation and for this reason it bases on the same hypotheses: three-phase system is balanced and symmetric with negligible harmonic distortions and so for the single-phase system all quantities are dominated by their fundamental components (at the line frequency). Thus, it is important to highlight that the modeling is not new respect to the dq impedance-based stability analysis, but applications and experimental validations will be done on single-phase system and this is not included in [128].

This Chapter considers the stability analysis of a single-phase AC system at a particular point of connection between a source and a load system, as in Fig. 1.13. This can be done theoretically with no loss of generalization, because if the considered scenario is more complex, it can be split in two subsystems: one clustered in a source subsystem and another in a load one.

4.2.1 Multifrequency averaging technique

The averaging method proposed in [142] is now recalled, because later it is used in the modeling. The Fourier series describes a signal $x(\tau)$ in the interval $\tau \in [t-T,\, t]$ as

$$x(\tau) = \sum_{l=-\infty}^{+\infty} \langle x \rangle_l (t)\, e^{jl\omega_o \tau} \tag{4.1}$$

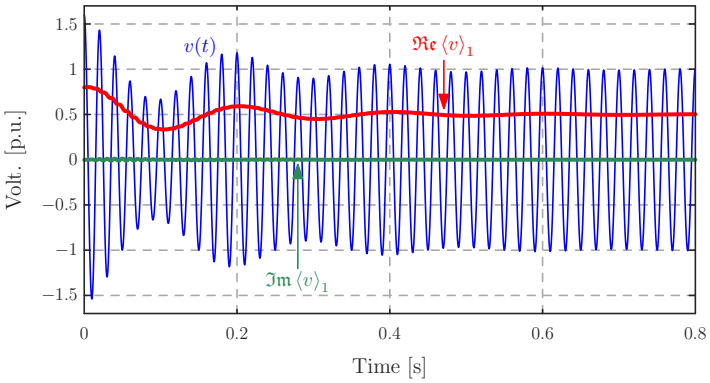

Figure 4.1: Example of application of dynamic phasor

where $\omega_o = 2\pi/T$ and the $\langle x\rangle_l(t)$ are the complex Fourier coefficients that are given by

$$\langle x\rangle_k(t) = \frac{1}{T}\int_{t-T}^{t} x(\tau)\, e^{-jk\omega_o\tau}\mathrm{d}\tau \tag{4.2}$$

Observe that such Fourier coefficients are functions of time t. As in [142], the k-th coefficient of the Fourier series is here called *k-phasor*. For sake of simplicity, the same notation of [142] is used herein.

The transformation (4.2) has an important property related to the differentiation with respect to time [142]:

$$\frac{\mathrm{d}\langle x\rangle_k(t)}{\mathrm{d}t} = \left\langle \frac{\mathrm{d}x}{\mathrm{d}t} \right\rangle_k (t) - jk\omega_o\langle x\rangle_k(t) \tag{4.3}$$

Consider also that if $x(\tau) \in \mathbb{R}$, $\forall\, \tau \in [t-T,\, t]$ then

$$\langle x\rangle_k(t) = \left[\langle x\rangle_{-k}(t)\right]^* \tag{4.4}$$

Dynamic phasors have been introduced because they allow to identify a steady-state operation for the model of a single-phase AC system (more details later). In Fig. 4.1 there is an example: considering an AC signal at ω_o and applying the (4.2), the real and imaginary components of the corresponding 1-phasor result to be constant in an single-phase AC steady-state operation.

4.2.2 Single-phase AC system modeling

A single-phase AC system, for instance that in Fig. 1.13, can be modeled with a nonlinear time-varying set of differential equations

$$\frac{\mathrm{d}x}{\mathrm{d}t} = f\left(x,\, t\right) \tag{4.5}$$

where x is a n-dimensional real vector of states, t is the time variable and f is a function from $\mathbb{R}^{n+1}$ to $\mathbb{R}^n$. Such model is *non-autonomous* because of the sinusoidal behavior of the electric grid, i.e. there is at least one sinusoidal term inside f, as for example $V_o \cos \omega_o t$. Notice that the function f in (4.5) can contain some input variables, for example some inverter or load references, but they are not explicitly written in that equation for sake of simplicity.

Looking at Fig. 1.13, it is reasonable to assume that the states of the source system do not directly depend on the states of the load system and conversely that the states of the load do not directly depend on the states of the source. Thus, the interactions between the two systems are only due to the quantities at their interfaces, that are the current i and the voltage v. So suppose that i is an input for the model of the source and v an input for the model of the load: also the opposite choice is possible [143]. So, with these observations equation (4.5) can be divided in

$$\begin{cases} \left.\begin{array}{rcl} \dfrac{\mathrm{d}x_1}{\mathrm{d}t} & = & f_1\left(x_1,\, i,\, t\right) \\ v & = & g_1\left(x_1,\, i,\, t\right) \end{array}\right\} & \text{source} \\ \left.\begin{array}{rcl} \dfrac{\mathrm{d}x_2}{\mathrm{d}t} & = & f_2\left(x_2,\, v,\, t\right) \\ i & = & g_2\left(x_2,\, v,\, t\right) \end{array}\right\} & \text{load} \end{cases} \tag{4.6}$$

where x_1 and x_2 are two sub-vectors of x and f_1, f_2, g_1, and g_2 are general nonlinear functions of suitable dimensions.

The analysis of source and load systems separately can bring to an impedance-based representation for both of them and, since their analysis is similar, here only the source model is investigated. As stated before, the AC single-

phase system has quantities (currents and voltages) mainly dominated by their fundamental components at the nominal line frequency ω_o (as done in [65] and in the following papers for dq impedance-based models). This hypothesis enables the modeling of the grid with a Fourier series analysis truncated at the 1-phasor. This truncation is an approximation and later it will be validated with experimental results. In general, the model can include also the 0-phasor components because some variables can have significant average value, for instance DC currents and voltages in hybrid AC-DC systems (rectifiers, inverters, etc.), Fig. 4.2, or quantities of the regulators. However, 0-phasor components will be neglected to keep the mathematical formulation closer to the dq transformation approach of three-phase systems, where only descriptions of dq space vectors at the nominal frequency are considered.

Standard modeling approaches for DC-DC converters and for converter-based three-phase AC systems (modeled in the abc domain or dq reference frame) usually have ranges of validity from DC up to fractions of the switching frequency f_s, e.g. $f_s/3 - f_s/2$: this is due to the averaging technique at f_s that is used to address the time-varying behavior of switches. Also dq impedance-based analysis for three-phase systems has the same frequency range of validity because it uses the same hypotheses: the results for dq impedance plots are often given up to fractions of the switching frequency. Examples are for DC systems in [63] and for three-phase AC systems in [55, 126]. Notice that if the system includes diode/thyristor rectifiers, then the validity of the averaged model can be limited to a lower fraction of the averaging frequency (e.g. 6 or 12 times the line frequency, for six or twelve pulse rectifies).

In this Chapter, the use of the dynamic phasors could potentially introduce some limits on the frequency range of validity, in particular because of the presence of multiple frequency components. Anyway, when the fundamental component phasor is dominant, the frequency range of validity can be extended as done for the application of the dq method for three-phase systems. One reason is that dynamic phasors do not introduce further approximations compared to the base averaged modeling, since there are not hypotheses on the frequency range of validity of dynamic phasors [142]. This means that the k-phasor has

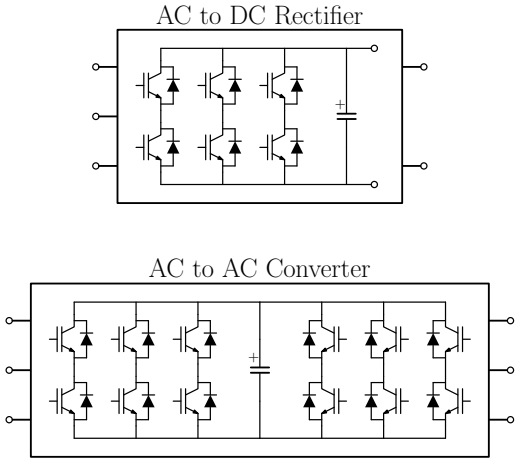

Figure 4.2: Examples of hybrid AC/DC systems

a valid definition even for frequencies higher than $k\omega_o$. So, as long as the averaged model of the single-phase system, valid up to a fraction of the switching frequency, is correctly represented by the fundamental dynamic phasor (the 1-phasor), then the analysis is still valid up to a fraction of the switching frequency. Similarly to the three-phase systems, the presence of diode rectifiers or single-phase systems requiring averaging at lower frequency, further limits the model bandwidth. However, further direct investigations on the frequency range of validity of this modeling should be performed as future tasks.

Writing the source model of (4.6) for 1-phasors using (4.3), it becomes

$$\begin{cases} \dfrac{\mathrm{d}\langle x_1\rangle_1}{\mathrm{d}t} &= \langle f_1\left(x_1,\, i,\, t\right)\rangle_1 - j\omega_o\langle x_1\rangle_1 \\ \langle v\rangle_1 &= \langle g_1\left(x_1,\, i,\, t\right)\rangle_1 \end{cases} \tag{4.7}$$

The (-1)-phasor model is not included in (4.7) because it is fully described by the $\langle x\rangle_1$ components, since $\langle x\rangle_{-1} = \langle x\rangle_1{}^*$ from (4.4).

According to the initial hypotheses, in a steady-state operation of the AC grid where all variables are dominated by their 1-phasors, the complex states in (4.7) are constant and so their derivatives are null. This means that an equilibrium for such model exists and a small-signal stability analysis is possible. Suppose that two complex functions that describe the phasors of the right-hand

sides of (4.7) according to the phasors of the state x_1 and the input i exist, because all quantities are assumed to be well described by their 1-phasors. With these functions the system (4.7) can be written as

$$\begin{cases} \dfrac{\mathrm{d}\langle x_1\rangle_1}{\mathrm{d}t} &= \mathbf{f}_1\left(\langle x_1\rangle_1, \langle i\rangle_1\right) - j\omega_o\langle x_1\rangle_1 \\ \langle v\rangle_1 &= \mathbf{g}_1\left(\langle x_1\rangle_1, \langle i\rangle_1\right) \end{cases} \tag{4.8}$$

where $\mathbf{f}_1$ and $\mathbf{g}_1$ are suitable complex functions.

In order to apply the standard state-space representation, the system (4.8) is described with real and imaginary components:

$$\begin{cases} \dfrac{\mathrm{d}\langle x_1\rangle_1^R}{\mathrm{d}t} &= \mathbf{f}_1^R\left(\langle x_1\rangle_1^R, \langle x_1\rangle_1^I, \langle i\rangle_1^R, \langle i\rangle_1^I\right) + \omega_o\langle x_1\rangle_1^I \\ \dfrac{\mathrm{d}\langle x_1\rangle_1^I}{\mathrm{d}t} &= \mathbf{f}_1^I\left(\langle x_1\rangle_1^R, \langle x_1\rangle_1^I, \langle i\rangle_1^R, \langle i\rangle_1^I\right) - \omega_o\langle x_1\rangle_1^R \\ \langle v\rangle_1^R &= \mathbf{g}_1^R\left(\langle x_1\rangle_1^R, \langle x_1\rangle_1^I, \langle i\rangle_1^R, \langle i\rangle_1^I\right) \\ \langle v\rangle_1^I &= \mathbf{g}_1^I\left(\langle x_1\rangle_1^R, \langle x_1\rangle_1^I, \langle i\rangle_1^R, \langle i\rangle_1^I\right) \end{cases} \tag{4.9}$$

where the R and I superscripts refer to real and imaginary components. In particular, such real and imaginary components of dynamic phasors are the same of [142].

The application of the average method [142] with a fundamental period equal to the nominal line period leads to a state-space model (4.9) with a well-defined operating point. This steady-state operation is referred as

$$\left(\langle X_1\rangle_1^R, \langle X_1\rangle_1^I, \langle I\rangle_1^R, \langle I\rangle_1^I\right) \tag{4.10}$$

The state-space model (4.9) can be linearized in the operating point (4.10) and its linearization leads to a description for the variations of the real and imaginary components of the dynamic phasors

$$\Delta\langle x_1\rangle_1^R,\ \Delta\langle x_1\rangle_1^I,\ \Delta\langle i\rangle_1^R,\ \Delta\langle i\rangle_1^I \tag{4.11}$$

The Laplace transform $\mathcal{L}$ can provide a compact description of the linearization of (4.9) between the real and imaginary components of $\langle v \rangle_1$ and $\langle i \rangle_1$

$$V(s) \triangleq \begin{bmatrix} V_R(s) \\ V_I(s) \end{bmatrix} = \underbrace{\begin{bmatrix} Z_{RR}(s) & Z_{RI}(s) \\ Z_{IR}(s) & Z_{II}(s) \end{bmatrix}}_{\triangleq Z(s)} \underbrace{\begin{bmatrix} I_R(s) \\ I_I(s) \end{bmatrix}}_{\triangleq I(s)} \tag{4.12}$$

where

$$V_R(s) \triangleq \mathcal{L}\left[\Delta\langle v \rangle_1^R\right](s) \tag{4.13a}$$

$$V_I(s) \triangleq \mathcal{L}\left[\Delta\langle v \rangle_1^I\right](s) \tag{4.13b}$$

$$I_R(s) \triangleq \mathcal{L}\left[\Delta\langle i \rangle_1^R\right](s) \tag{4.13c}$$

$$I_I(s) \triangleq \mathcal{L}\left[\Delta\langle i \rangle_1^I\right](s) \tag{4.13d}$$

and where $Z_{RR}(s)$, $Z_{RI}(s)$, $Z_{IR}(s)$, and $Z_{II}(s)$ are four Laplace transfer functions, that are here called RI *small-signal impedances*.

The same analysis can be performed for the load system of Fig. 1.13, whose equations are in (4.6). Considering for example the voltage v as input and the current $-i$ as output, it results:

$$-I(s) = \begin{bmatrix} -I_R(s) \\ -I_I(s) \end{bmatrix} = \underbrace{\begin{bmatrix} Y_{RR}(s) & Y_{RI}(s) \\ Y_{IR}(s) & Y_{II}(s) \end{bmatrix}}_{\triangleq Y(s)} \underbrace{\begin{bmatrix} V_R(s) \\ V_I(s) \end{bmatrix}}_{V(s)} \tag{4.14}$$

4.2.3 Generalized Nyquist stability criterion

Each quantity in the derived models, currents and voltages in (4.12) and (4.14), are represented by a couple of two real variables: the real R and the imaginary I components of the phasor. For the small-signal model, an impedance-based representation similar to that for DC systems in [63] can be used. The only difference is that the resulting model is MIMO where each quantity is a 2-dimensional vector and each impedance is a 2×2 matrix of transfer functions, as for the study of balanced AC three-phase systems [55, 65].

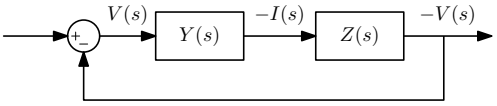

Figure 4.3: Block diagram representation

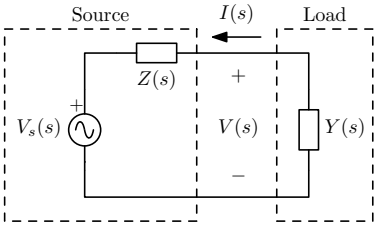

Figure 4.4: Thévenin representation of the system

Since the output voltage and current used in the source and load models are the same, their small-signal variations of (4.12) and (4.14) can depict a feedback loop system as in Fig. 4.3. This can be seen as the block diagram generated by the Thévenin representation of Fig. 4.4.

The GNC can be applied to the loop gain

$$T(s) \triangleq Z(s)\ Y(s) \tag{4.15}$$

of the system in Fig. 4.3 to infer the stability of the closed-loop system and thus of the interaction of the source and load subsystems. The complete formulation of the GNC is in [66]. The eigenvalues of $T(s)$, $\lambda_1(s)$ and $\lambda_2(s)$, are frequency-dependent and they trace in the complex plane the characteristic loci of matrix $T(s)$ as the variable s moves on the standard Nyquist contour in clockwise direction. The closed-loop system is stable if and only if the net sum of anticlockwise encirclements of the critical point $-1 + j0$ by the set of characteristic loci of $T(s)$ is equal to the total number of right-half plane poles of $Z(s)$ and $Y(s)$. So if the source and load systems are stable on their own (no right-half plane poles for $Z(s)$ and $Y(s)$), then the closed-loop system is stable if and only if the Nyquist diagrams of the two eigenvalues do not encircle the critical point. A stable transfer function $Z(s)$ means that the source can work in an open-circuit configuration (zero output current) and a $Y(s)$ stable transfer function means that the load can work in a short circuit configuration

(zero output voltage) [143].

4.3 Signal injection

The approach to the stability analysis presented in Sec. 4.2 is now described with some implementation details related to signal injection [122]. The focus is again on the source system, whose model has the current as input and the voltage as output, see (4.12). In order to determine the four RI impedances of (4.12), a single frequency disturbance at ω_p can be injected in the system to perturb the steady-state in (4.10), first on the real component of the phasor $\langle i \rangle_1$ and then on the imaginary one. So a sinusoidal disturbance $I_p \cos \omega_p t$ of the real component of $\langle i \rangle_1$ is

$$\langle i \rangle_1 (t) = \underbrace{\langle I \rangle_1^R + j \langle I \rangle_1^I}_{\text{steady-state}} + \underbrace{I_p \cos \omega_p t}_{\text{perturbation}} \tag{4.16a}$$

and similarly an imaginary perturbation of the 1-phasor is

$$\langle i \rangle_1 (t) = \underbrace{\langle I \rangle_1^R + j \langle I \rangle_1^I}_{\text{steady-state}} + \underbrace{j I_p \cos \omega_p t}_{\text{perturbation}} \tag{4.16b}$$

To inject such perturbations in the single-phase system, the time-domain expression for $i(t)$ has to be evaluated using (4.1) and (4.4). Setting $\langle I \rangle_1 = \langle I \rangle_1^R + j \langle I \rangle_1^I$, the real perturbation (4.16a) becomes

$$i\,(t) = \, 2\,|\langle I \rangle_1| \cos\left(\omega_o t + \arg\langle I \rangle_1\right) + 2 I_p \cos\left(\omega_p t\right) \cos\left(\omega_o t\right) \tag{4.17a}$$

and the imaginary perturbation (4.16b)

$$i\,(t) = \, 2\,|\langle I \rangle_1| \cos\left(\omega_o t + \arg\langle I \rangle_1\right) - 2 I_p \cos\left(\omega_p t\right) \sin\left(\omega_o t\right) \tag{4.17b}$$

This disturbance injection consists of a modulation of the fundamental phasors, i.e. an amplitude modulation (4.16a) and a phase modulation (4.16b) as in [142]. For sake of simplicity, consider a steady-state operation with $\langle I \rangle_1^I = 0$

and $\langle I \rangle_1^R > 0$. From (4.17a), it follows:

$$i\left(t\right) = 2\left[\langle I \rangle_1^R + I_p \cos\left(\omega_p t\right)\right] \cos\left(\omega_o t\right) \tag{4.18a}$$

that is an amplitude modulation of the line frequency component. From (4.17b), considering again $\langle I \rangle_1^I = 0$ and $\langle I \rangle_1^R > 0$, it results:

$$\begin{aligned} i\left(t\right) &= 2\langle I \rangle_1^R \cos\left(\omega_o t\right) - 2I_p \cos\left(\omega_p t\right) \sin\left(\omega_o t\right) \simeq \\ &\simeq 2\langle I \rangle_1^R \cos\left(\omega_o t\right) \cos\left[\frac{I_p}{\langle I \rangle_1^R} \cos\left(\omega_p t\right)\right] + \\ &- 2\langle I \rangle_1^R \sin\left(\omega_o t\right) \sin\left[\frac{I_p}{\langle I \rangle_1^R} \cos\left(\omega_p t\right)\right] \\ &= 2\langle I \rangle_1^R \cos\left[\omega_o t \; + \frac{I_p}{\langle I \rangle_1^R} \cos\left(\omega_p t\right)\right] \end{aligned} \tag{4.18b}$$

where the following approximations are done for I_p small enough:

$$\cos\left[\frac{I_p}{\langle I \rangle_1^R} \cos\left(\omega_p t\right)\right] \simeq 1 \tag{4.19a}$$

$$\sin\left[\frac{I_p}{\langle I \rangle_1^R} \cos\left(\omega_p t\right)\right] \simeq \frac{I_p}{\langle I \rangle_1^R} \cos\left(\omega_p t\right) \tag{4.19b}$$

Equation (4.18b) represents a phase modulation of the fundamental component.

Performing a current injection means adding to the output current a term equal to the last one of (4.17a) or (4.17b), and so a parallel current generator as shown in Fig. 4.5.a can be used [127, 144, 145]. Observe that in general to inject such terms, a PLL may be required to synchronize the signal to the fundamental system component $\cos \omega_o t$. On the other hand, for voltage signals, series voltage injection as in Fig. 4.5.b is often used in literature [127,144,145].

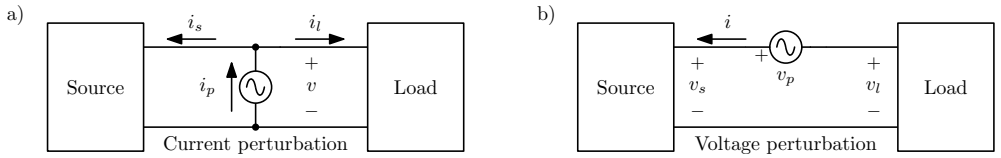

Figure 4.5: a) Parallel current injection and b) series voltage injection to perturb the system for impedance identification

4.4 Measurements and impedance evaluation

When a current perturbation is performed, the corresponding output voltage v of Fig. 4.5.a has to be measured, while for a voltage perturbation, a current has to be measured i in Fig. 4.5.b. In both cases, the input and output signals are all post-processed to evaluate the corresponding 1-phasors that will be used in (4.12) or (4.14) for the impedance identification. According to (4.2), the real and imaginary components of 1-phasor, for instance on the voltage $v\,(t)$, can be calculated as

$$\langle v \rangle_1^R(t) = \frac{1}{T}\int_{t-T}^{t} v\,(\tau)\cos\left(\omega_o \tau\right) \mathrm{d}\tau \tag{4.20a}$$

and

$$\langle v \rangle_1^I(t) = -\frac{1}{T}\int_{t-T}^{t} v\,(\tau)\sin\left(\omega_o \tau\right) \mathrm{d}\tau \tag{4.20b}$$

The Laplace transforms of these components are

$$\mathcal{L}\left[\langle v \rangle_1^R\right](s) = H\,(s)\ \mathcal{L}\left[\,v\,(t)\cos\left(\omega_o t\right)\,\right](s) \tag{4.21a}$$

$$\mathcal{L}\left[\langle v \rangle_1^I\right](s) = H\,(s)\ \mathcal{L}\left[\,-v\,(t)\sin\left(\omega_o t\right)\,\right](s) \tag{4.21b}$$

where $H\,(s) \triangleq \left(1 - e^{-Ts}\right) / \left(Ts\right)$.

The RI identification is performed by the injection of a disturbance, as in (4.16a) or (4.16b), at one frequency ω_p to evaluate the four impedances at ω_p and then repeating the injection for different ω_p frequencies. From equations (4.12) and (4.21), it follows that

$$\begin{aligned}\mathcal{L}\left[\,v\,(t)\cos\left(\omega_o t\right)\,\right](j\omega_p) = Z_{RR}\,(j\omega_p)\,\mathcal{L}\left[\,i\,(t)\cos\left(\omega_o t\right)\,\right](j\omega_p) + \\ + Z_{RI}\,(j\omega_p)\,\mathcal{L}\left[\,-i\,(t)\sin\left(\omega_o t\right)\,\right](j\omega_p)\end{aligned} \tag{4.22a}$$

$$\begin{aligned}\mathcal{L}\left[-v\left(t\right)\sin\left(\omega_o t\right)\right]\left(j\omega_p\right) = Z_{IR}\left(j\omega_p\right)\mathcal{L}\left[i\left(t\right)\cos\left(\omega_o t\right)\right]\left(j\omega_p\right) + \\ + Z_{II}\left(j\omega_p\right)\mathcal{L}\left[-i\left(t\right)\sin\left(\omega_o t\right)\right]\left(j\omega_p\right)\end{aligned} \tag{4.22b}$$

where all the $H(j\omega_p)$ transfer functions vanish. From an operative point of view, the Discrete Fourier Transform (DFT) of the input current signal can evaluate the Laplace transforms of $i\left(t\right)\cos\left(\omega_o t\right)$ and $i\left(t\right)\sin\left(\omega_o t\right)$ for $j\omega_p$ and the same for the output voltage to evaluate the Laplace transforms of $v\left(t\right)\cos\left(\omega_o t\right)$ and $v\left(t\right)\sin\left(\omega_o t\right)$ in $j\omega_p$. Defining

$$\mathcal{L}\left[i\left(t\right)\cos\left(\omega_o t\right)\right]\left(j\omega_p\right) \triangleq \tilde{I}_R\left(j\omega_p\right) \tag{4.23a}$$

$$\mathcal{L}\left[-i\left(t\right)\sin\left(\omega_o t\right)\right]\left(j\omega_p\right) \triangleq \tilde{I}_I\left(j\omega_p\right) \tag{4.23b}$$

$$\mathcal{L}\left[v\left(t\right)\cos\left(\omega_o t\right)\right]\left(j\omega_p\right) \triangleq \tilde{V}_R\left(j\omega_p\right) \tag{4.23c}$$

$$\mathcal{L}\left[-v\left(t\right)\sin\left(\omega_o t\right)\right]\left(j\omega_p\right) \triangleq \tilde{V}_I\left(j\omega_p\right) \tag{4.23d}$$

the four RI impedances in (4.22) are evaluated by injecting two linearly independent perturbations: for instance $\left(\tilde{I}_{R1},\, \tilde{I}_{I1}\right)$ generating $\left(\tilde{V}_{R1},\, \tilde{V}_{I1}\right)$ and $\left(\tilde{I}_{R2},\, \tilde{I}_{I2}\right)$ generating $\left(\tilde{V}_{R2},\, \tilde{V}_{I2}\right)$. Thus, the four RI impedances are the solutions of

$$\begin{bmatrix}\tilde{V}_{R1}\\ \tilde{V}_{I1}\\ \tilde{V}_{R2}\\ \tilde{V}_{I2}\end{bmatrix} = \begin{bmatrix}\tilde{I}_{R1} & \tilde{I}_{I1} & 0 & 0\\ 0 & 0 & \tilde{I}_{R1} & \tilde{I}_{I1}\\ \tilde{I}_{R2} & \tilde{I}_{I2} & 0 & 0\\ 0 & 0 & \tilde{I}_{R2} & \tilde{I}_{I2}\end{bmatrix}\begin{bmatrix}Z_{RR}\\ Z_{RI}\\ Z_{IR}\\ Z_{II}\end{bmatrix} \tag{4.24}$$

Two linear perturbations mean that the rank of the matrix in (4.24) is equal to 4. A similar approach is also used in [127, 128].

4.5 Equivalence with dq transformation theory

In this section, it is shown that the method described so far leads to a final model that is similar to the one obtained with the dq impedance-based method proposed first for balanced three-phase systems in [55, 65] and then extended to the single-phase systems in [127, 128].

Recalling what said at the beginning of Sec. 4.2, the single-phase system

can be seen as one phase of an artificial three-phase system. For example, it can be created considering the phase a as the phase of the single-phase system and the phases b and c as two artificial phases that are shifted respectively of $120°$ and $240°$ with respect to the phase a. This enables the application of the dq small-signal analysis for three-phase systems [55, 65] to this artificial abc model. As hypotheses, such system is *balanced* and *symmetric*, as in the standard three-phase theory [55, 65]: these are the same hypotheses of Secs. 4.2-4.4.

Using the Bounded-Input Bounded-Output (BIBO) stability definition of [65], the single-phase system is BIBO stable if and only if its artificial three-phase system is BIBO stable because in a balanced and symmetric three-phase system the quantities are simply shifted of $120°$ and of $240°$ from one phase to the other. This observation is needed in order to use the dq impedanced-based approach proposed in [55, 65] to infer the stability of the single-phase system.

The dq impedanced-based analysis of [55, 65] is based on a different description for the currents and the voltages of the grid compared to the approach of this Chapter. However, at the end such analysis arrives at small-signal descriptions of source and load systems that are equivalent to those in (4.12) and (4.14) and so the GNC can be applied. In this approach, the perturbations consist of modulating (for different frequency ω_p) the d and q components of space vector of current or voltage at the interface between source and load subsystems in order to obtain the impedances in (4.12) and (4.14), now called dq impedances. A sinusoidal perturbation of the d component or of the q component, after its transformation into the single-phase domain with (1.9) and (1.10), results equal to the amplitude or phase modulation in (4.17a) or (4.17b).

After injecting the perturbation of the system with (4.17a) or (4.17b), the voltage at the source-load interface is measured and post-processed by applying the abc to dq transformation for three-phase systems, namely (1.9) and (1.10). The DFT of the d and q components can be evaluated numerically to obtain the voltage coefficients at the frequency of the disturbance $j\omega_p$ and then with these complex coefficients the dq impedances can be calculated solving a linear system equivalent to (4.24). Setting the quantities of phases b and c to zero in

(1.9) and (1.10) to evaluate the d and q components and calculating the DFT, the evaluation process of the impedances results equal to that in (4.22). This means that both the signal injections and the post-processing of the measured values are equivalent to those of Secs. 4.3 and 4.4.

At the beginning of this section, it is stated that an artificial three-phase system is built from the single-phase system to be balanced and symmetric, however since the components of phases b and c can not be directly measured, it is possible to set them to zero rather than calculating them during post-processing. This will lead to an unbalanced and asymmetric system, but the dq impedances can still be evaluated. The measured variable v contains only components at the fundamental line frequency ω_o plus the harmonics injected with the dq perturbation (remember that the harmonic distortions are negligible) and so v has an expression similar to that in (4.17a) or (4.17b). Such behavior can be expected even if the system is nonlinear considering that the disturbance injection is small enough to avoid nonlinearity distortions. So if the fundamental component for the voltage is $V_o \cos(\omega_o t)$, the voltage $v(t)$ results

$$\begin{aligned} v(t) &= V_o \cos(\omega_o t + \varphi_o) + V_p \cos(\omega_p t + \varphi_p) \cos(\omega_o t) = \\ &= V_o \cos(\omega_o t + \varphi_o) + \frac{V_p}{2} \cos[(\omega_o - \omega_p) t - \varphi_p] + \\ &\quad + \frac{V_p}{2} \cos[(\omega_o + \omega_p) t + \varphi_p] \end{aligned} \tag{4.25}$$

for the signal in (4.17a). In the single-phase domain (4.25) there are three components: one at the nominal frequency ω_o and two at $\omega_o - \omega_p$ and $\omega_o + \omega_p$ as for standard amplitude modulated signals. This situation is depicted in Fig. 4.6.a.

Considering the artificial three-phase system by setting the b and c components to zero and transforming (4.25) with (1.9) and (1.10), the d component results

$$\begin{aligned} v_d(t) &= \frac{V_o}{3} \cos\varphi_o + \frac{V_p}{3} \cos(\omega_p t + \varphi_p) + \\ &\quad + \frac{V_p}{6} \cos[(2\omega_o - \omega_p) t - \varphi_p] + \frac{V_o}{3} \cos(2\omega_o t + \varphi_o) + \\ &\quad + \frac{V_p}{6} \cos[(2\omega_o + \omega_p) t + \varphi_p] \end{aligned} \tag{4.26}$$

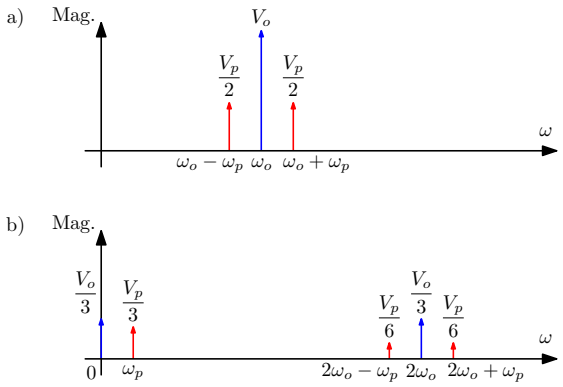

Figure 4.6: Amplitude spectral components: a) for the single-phase initial system and b) for the artificial three-phase system for d component [122]

The spectral components of this signal are shown in Fig. 4.6.b: to calculate the dq impedances, the component at ω_p of this figure has to be evaluated. On the other hand, in an artificial balanced and symmetric three-phase system the d and q quantities contain only DC components (null frequency) plus the frequency of the injected component ω_p: in this situation the three highest frequency components of Fig. 4.6.b are missing. Anyway, both these two techniques can theoretically calculate the same impedances thanks to the frequency selectivity of the DFT: frequency overlaps should however be avoided and, from Fig. 4.6.b, this happens for $\omega_p \neq \omega_o$. So setting the b and c components to zero enables the evaluation of the same dq impedances, except for $\omega_p = \omega_o$.

In the next section, the approach of Secs. 4.2-4.4 based on RI impedances is applied experimentally to study the stability of a single-phase system to analyze the behavior of a grid-feeding inverter synchronized via PLL.

4.6 Experimental validation

The validation of the stability analysis is done on a single-phase experimental setup that consists of a voltage-controlled inverter and a current-controlled inverter, see Fig. 4.7 [122]. This test-case is seen as the case of current injection made by a PV system into a slight AC grid (the mains) that has a certain output impedance. Both inverters have $5\,\mathrm{kVA}$ rated power, but the experiments

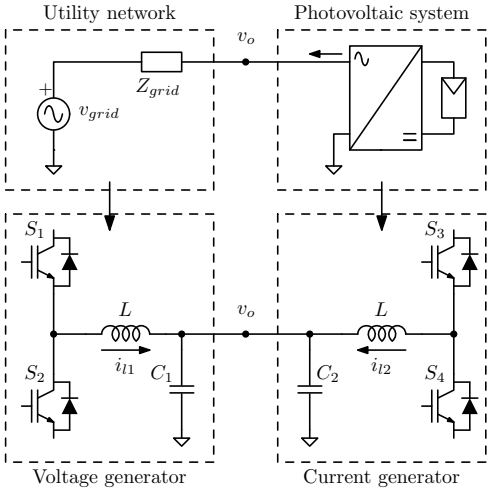

Figure 4.7: Test-case whose parameters are in Tab. 4.1 [122]

are performed at reduced voltage, that is $V_o = 50\,\mathrm{V_{RMS}}$, and reduced power.

The voltage-controlled inverter generates a sinusoidal voltage at its output v_o tracking a reference $v_{o,ref}$ equal to $V_o\sqrt{2}\cos\omega_o t$, where $\omega_o = 2\pi 50\,\mathrm{rad/s}$ is the nominal frequency. It includes an inner current regulation loop and an outer voltage controller as shown in Fig. 4.8.a: the current loop has a closed-loop bandwidth of $1.5\,\mathrm{kHz}$ and the voltage loop of $320\,\mathrm{Hz}$. The parameters of the experimental setup are in Tab. 4.1.

PV applications usually include current-controlled inverters synchronized to the grid via PLL [20, 146]. Different solutions for PLL have been studied in literature, both in three-phase and single-phase connections [20, 147]. Here, an SRF-PLL is used to synchronize the current-controlled inverter to the grid (Fig. 4.8.b): its outputs, i.e. the angle θ of the voltage waveform and its amplitude V_{pll}, are used to generate the current reference for the inverter. For instance in PV applications, the current reference is in phase with the inverter voltage (and so with θ), while the current amplitude reference ($I_{l2,ref}$ in Fig. 4.8.b) is set by the DC link voltage controller to inject all the available active power [146]. On the other hand, in constant power sources (or loads) the current amplitude reference $I_{l2,ref}$ results from the PLL voltage amplitude measurement as $I_{l2,ref} = P/V_{pll}$ after suitable filtering. For single-phase applications, the PLL needs to estimate the in-quadrature component of the input

Table 4.1: Experimental setup parameters [122]

Grid	V_o	$=$	$50\,\mathrm{V_{RMS}}$
	ω_o	$=$	$2\pi 50\,\mathrm{rad/s}$
Filters	L	$=$	$1.6\,\mathrm{mH}$
	C_1	$=$	$50\,\mu\mathrm{F}$
	C_2	$=$	$10\,\mu\mathrm{F}$
Grid inverter	$k_{P,i}$	$=$	3
	$k_{I,i}$	$=$	0.1
	$k_{P,u}$	$=$	1
	$k_{I,u}$	$=$	0.15
	f_{PWM}	$=$	$12.5\,\mathrm{kHz}$
PV inverter + PLL	$k_{P,i}$	$=$	2
	$k_{I,i}$	$=$	0.25
	$k_{P,pll}$	$=$	1.4
	$k_{I,pll}$	$=$	$7 \cdot 10^{-4}$
	$k_{I,pll,un}$	$=$	0.1
	f_{PWM}	$=$	$12.5\,\mathrm{kHz}$

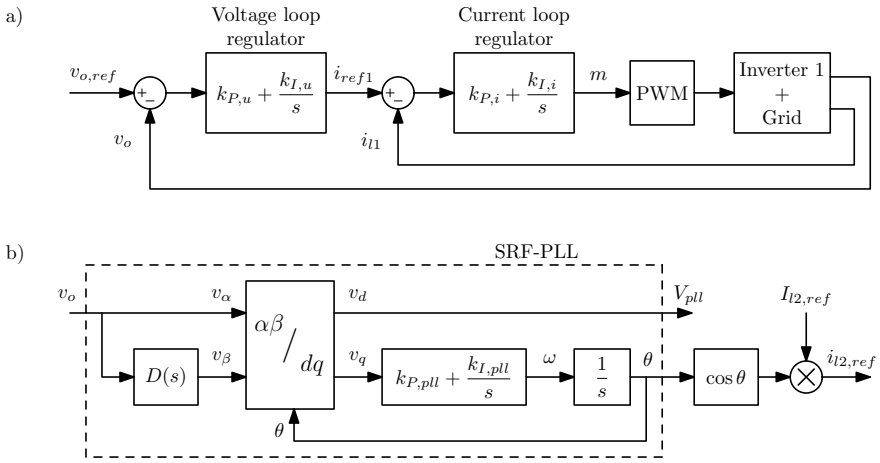

Figure 4.8: Controller scheme of a) the voltage generator and b) the current generator with PLL: parameter values are in Tab. 4.1

voltage and different solutions exist in literature, such as fixed $T_o/4$ delay, linear filtering, SOGI, etc. [20, 147]. In this section, a linear filter that introduces a $T_o/4$ time delay at ω_o is used (Fig. 4.8.b):

$$D(s) = \frac{\omega_s^2}{s^2 + s\omega_s + \omega_s^2} \tag{4.27}$$

with $\omega_s = \omega_o$ (ω_s can also be adaptively changed according to the PLL frequency).

In this validation, since the feasibility of the stability analysis described before has to be proved, the current amplitude reference $I_{l2,ref}$ is set to be proportional to the voltage amplitude of the PLL V_{pll} (after filtering) in the controller of Fig. 4.8.b: this will exhibit two behaviors of the system, one stable and one unstable. The current reference $i_{l2,ref}$ is then tracked by a current loop, similar to that of Fig. 4.8.a, that has a closed-loop bandwidth of $1\,\mathrm{kHz}$. The parameters of the controllers are in Tab. 4.1. Such system can be potentially dangerous for the stability since it exhibits a negative Z_{qq} or Z_{II} output impedance at low frequencies due to the PLL [137]. Generally, power sources have negative Z_{qq} impedances, while constant power loads have negative Z_{dd} impedances [137].

To validate the stability analysis of this Chapter and to describe the stability characteristics of the PLL, two different conditions for the test-case of Fig. 4.7

are considered, presenting two different designs of the PLL. In the first test, the PLL has been designed to obtain a *stable system* with a $20\,\mathrm{Hz}$ closed-loop bandwidth for the PLL (parameters are in Tab. 4.1). In a second test-case the integral parameter $k_{I,pll}$ of the PLL (Fig. 4.8.b) has been increased to $k_{I,pll,un} = 0.1$: this system is *unstable* and it presents a divergent behavior. Observe the experimental results in Fig. 4.9.a for a steady-state operation of the stable condition. In Fig. 4.9.b, at the beginning the system is in stable conditions and then suddenly the $k_{I,pll}$ is increased to bring the system in unstable condition: an initial divergent transient on the voltage and the current can be observed. However, after few line periods some controller parameters saturate (as the output of the load PLL that is limited) and limit cycles appear, see Fig. 4.9.b. So this system is unstable in a small-signal sense and then it goes to stable harmonic amplification due to saturation of controller parameters. In the results for the unstable case, oscillations at $96\,\mathrm{Hz}$ and $196\,\mathrm{Hz}$ appear on the voltage and current.

In this Chapter, the injection of current or voltage does not need additional hardware, because the current generator can inject a current disturbance into the voltage generator and vice versa the voltage generator can inject a voltage signal into the current generator. In order to do this, the voltage reference of the controller in 4.8.a is modified with terms similar to those in (4.17a) or (4.17b). For the current perturbation, instead of using the controller of 4.8.b, the current reference $i_{l2,ref}$ is directly set as in (4.17a) or (4.17b). Concerning the settings of the controllers during the impedance evaluation, the parameters of the current and voltage generators of Tab. 4.1 for the stable case are used to evaluate the impedances of source and load systems for the stable case. The same impedances of the source system are used also for the unstable case, since they are the same. On the other hand, to evaluate the impedances of the load system (current generator) for the unstable case, the system has to be stabilized to perform the perturbations, without changing the load subsystem itself. This is done increasing the bandwidth of the voltage controller loop of the voltage generator (source system) to $400\,\mathrm{Hz}$, with $k_{P,u} = 1.4$ and $k_{I,u} = 0.2$. Furthermore, a load resistance of $12.5\,\Omega$ is added at the source-load interface to increase the damping and attention is given to avoid that the operating point (i.e. the load

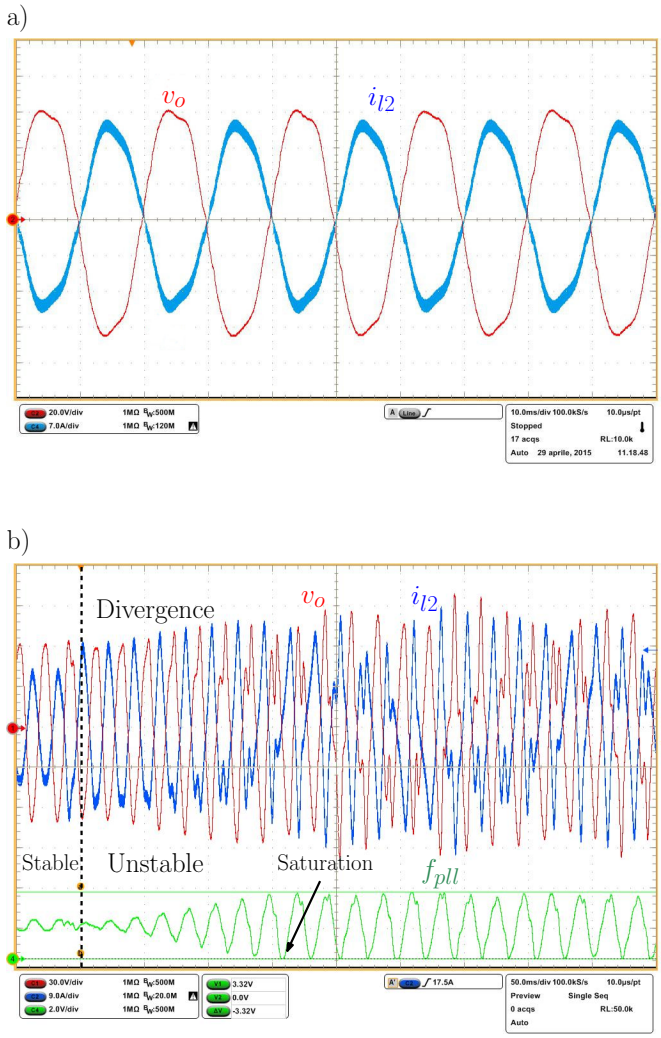

Figure 4.9: a) Voltage v_o ($20\,\mathrm{V/div}$) and current i_{l2} ($7\,\mathrm{A/div}$) of Fig. 4.7 in steady-state stable condition (time with $10\,\mathrm{ms/div}$) and b) Voltage v_o ($30\,\mathrm{V/div}$), current i_{l2} ($9\,\mathrm{A/div}$) and frequency of the load PLL f_{pll} ($30\,\mathrm{Hz/div}$) of Fig. 4.7 for the transition from stable to unstable condition (time with $50\,\mathrm{ms/div}$) [122]

current) changes. The load impedances are then measured downstream of the load resistance.

The perturbation injections are small in order to avoid changes in the steady-state operations of the two subsystems. In particular, current perturbations made by the current generator to evaluate the source impedances are about $2-3\,\%$ of the inverter current (at higher frequencies they decrease to $1\,\%$). To evaluate the load impedances (of current generator), the voltage generator injects a perturbation that is about $2.2\,\%$ of the steady-state voltage of the system.

Even if the PLL of the load system can make a coupling between phase and amplitude modulations of the phasors, the only requirement for the signal injection is that the two injections are independent to solve the system in (4.24) as done in [55], even if they are both phase and amplitude modulations simultaneously. To inject the two independent perturbations with the voltage generator, the voltage reference signal within its controller has been exploited, $v_{o,ref} = V_o\sqrt{2}\cos(\omega_o t)$ in Fig. 4.8: the two independent perturbations can be generated as $V_p\cos(\omega_p t)\cos(\omega_o t)$ and $V_p\sin(\omega_p t)\cos(\omega_o t)$, within the controller of the source system. On the other hand, for the perturbations injected by the load, the inner PLL can be exploited to obtain a reference of the voltage as $\cos(\omega_o t)$: the independent disturbances can be evaluated from this and generated in a similar manner to those of the voltage generator. This has already been implemented in many papers related to the impedance measurement units as those cited in [127, 144, 145].

During current or voltage disturbance injection, both current and voltage at the interface are measured with an oscilloscope that samples at $100\,\mathrm{kS/s}$ for $1\,\mathrm{s}$ interval. The post-processing of these data sets is done with Matlab and so on-line synchronization is not required (no PLL is used for the measurements). Fast Fourier Transform (FFT) is performed both for voltage and current and the $50\,\mathrm{Hz}$ component is used for the synchronization, i.e. the component at $50\,\mathrm{Hz}$ is the d-axis voltage and the component rotated by $90\,\mathrm{deg}$ is the q-axis. Then the RI impedances are calculated from the complex coefficients of voltage and current at the frequency ω_p. Impedances are shown in Figs. 4.10 and 4.11, respectively for the stable and unstable conditions, both for source and load

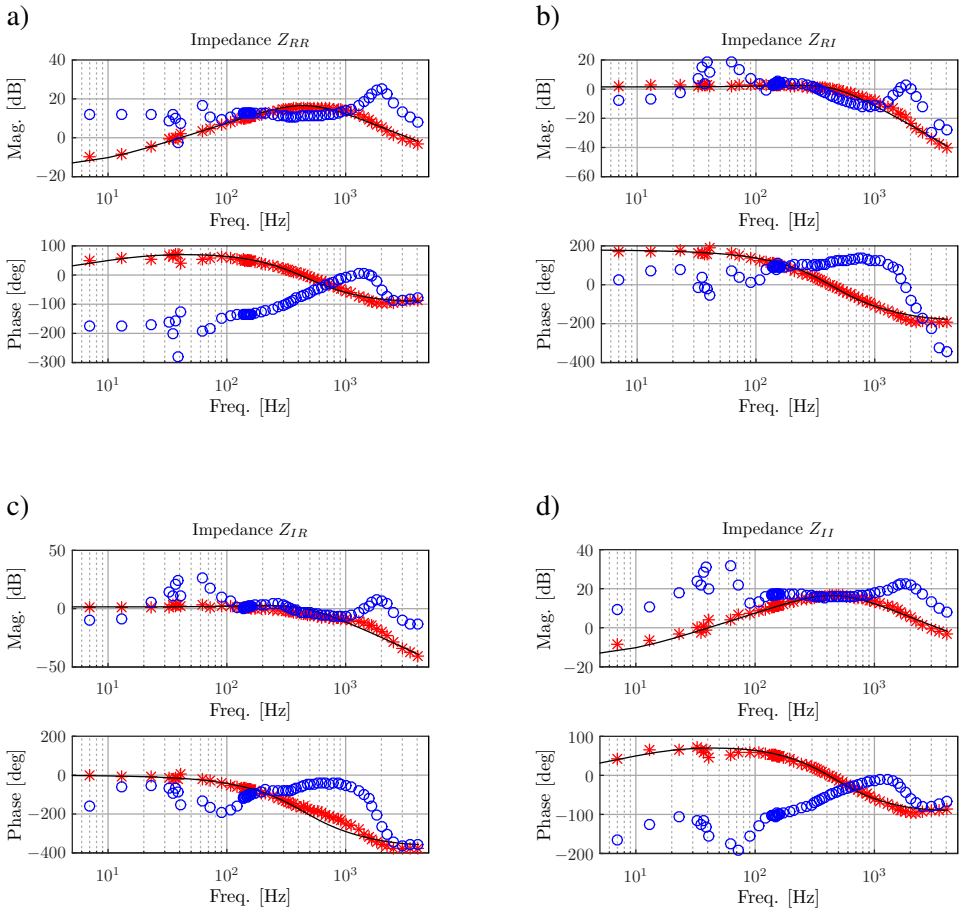

Figure 4.10: Bode diagrams of a) Z_{RR}, b) Z_{RI}, c) Z_{IR}, and d) Z_{II} impedances for stable condition: asterisks refer to experimental data for the source, circles refer to experimental data for the load and solid lines refer to analytic model of the source [122]

systems. Notice that the Z_{II} of the load (inverter with PLL) is negative for low frequencies (the phase is $-180\,\mathrm{deg}$), similar to the negative Z_{qq} of [137] because of the presence of PLL. Fig. 4.12 compares the Z_{II} for the load systems for the two conditions of this section: the unstable case exhibits a negative Z_{II} in a larger frequency range, for low frequencies, compared to the stable case.

The experimental data are compared to theoretical data where the impedance of the phase domain $Z_a\,(s)$ for the source system is evaluated first, considering an ideal system with no parasitic components and with continuous-time regulators. After this, the RI impedances are evaluated from (4.22) exploiting the

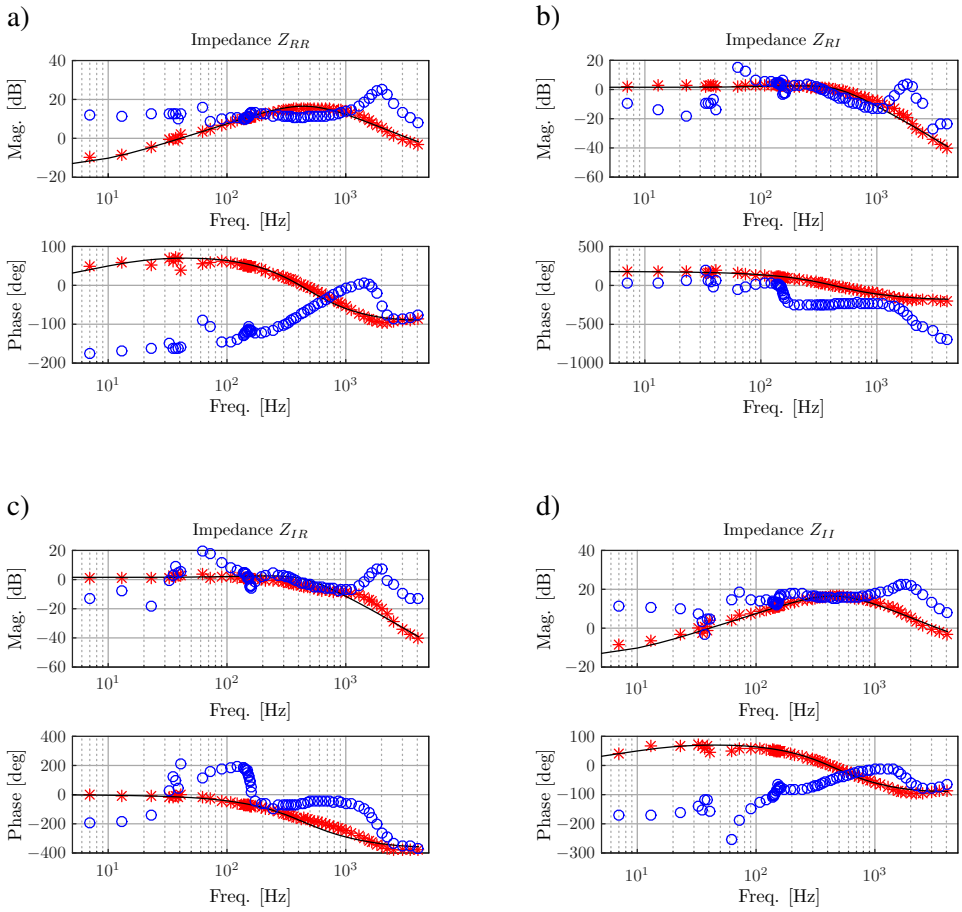

Figure 4.11: Bode diagrams of a) Z_{RR}, b) Z_{RI}, c) Z_{IR}, and d) Z_{II} impedances for unstable condition: asterisks refer to experimental data for the source, circles refer to experimental data for the load and solid lines refer to analytic model of the source [122]

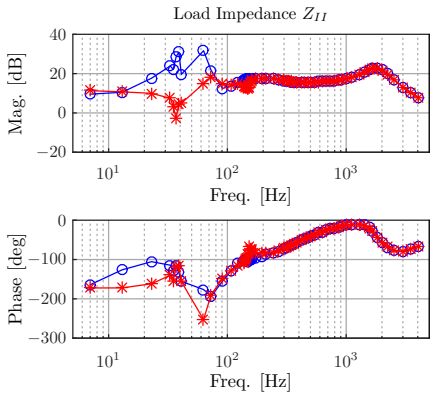

Figure 4.12: Bode diagram of Z_{II} impedance of the load for stable and unstable conditions: circles refer to experimental data for stable condition, asterisks refer to experimental data for unstable condition, and solid lines to interpolations [122]

properties of the Laplace transform:

$$Z_{RR}(s) = Z_{II}(s) = \frac{Z_a(s + j\omega_o) + Z_a(s - j\omega_o)}{2} \tag{4.28a}$$

$$Z_{IR}(s) = -Z_{RI}(s) = \frac{Z_a(s + j\omega_o) - Z_a(s - j\omega_o)}{2j} \tag{4.28b}$$

More details about the transformation (4.28) are given in [148, 149], which describes how to transform a Laplace transfer function defined in the abc or phase domain to the dq domain for balanced and symmetric three-phase systems. So the model (4.12) is derived in terms of RI impedances exploiting (4.28) and the equivalence with the dq domain. Notice that these analytic results are valid only for linear systems and that the source system is linear considering its time-averaging model and regulators with continuous-time implementations. A good agreement appears comparing the experimental and analytic results for the source system in Figs. 4.10 and 4.11 (notice that the impedances of the source are the same in the two cases).

After the evaluation of the impedances, the loop gain $T(j\omega)$ can be built and its two eigenvalues $\lambda_1(j\omega)$ and $\lambda_2(j\omega)$ plotted on the Nyquist charts (Figs. 4.13 and 4.14). In such graphs, there are only the Nyquist diagrams for the positive part of the Nyquist contour, that means only for positive ω frequencies (the other part of the contour is symmetric with respect to the real axis). The GNC applied

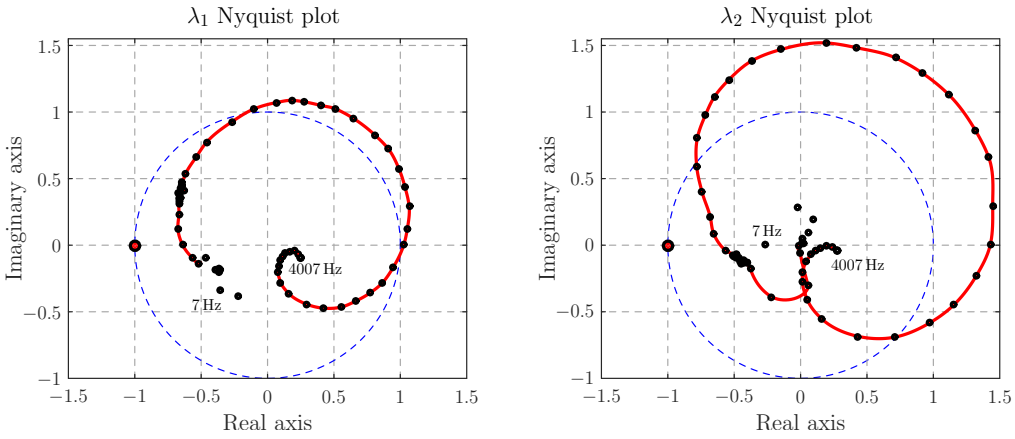

Figure 4.13: λ_1 and λ_2 Nyquist plots for stable conditions: dots refer to experimental data and solid lines to interpolations [122]

to a single-phase system can describe its stability characteristics: the eigenvalue traces for the stable system of Fig. 4.9.a do not encircle the $-1 + j0$ critical point and they are always far from that point, see Fig. 4.13. On the other hand, the unstable system of Fig. 4.9.b is described by Nyquist diagrams that are very close to the critical point, see Fig. 4.14. In particular, eigenvalue λ_2 encircles the critical point $-1 + j0$ and so the system is divergent in a small-signal sense as after the parameter change in Fig. 4.9.b. Moreover, the λ_2 Nyquist plot for unstable condition is close to the critical point at about $146\,\text{Hz}$ meaning that in the model for 1-phasors there are undamped oscillations at such frequency. These oscillations correspond to oscillations at frequencies $146 - 50 = 96\,\text{Hz}$ and $146 + 50 = 196\,\text{Hz}$ in the time-domain, due to the exponential terms in the definition (4.1). This observation given by the Nyquist diagrams matches with the oscillations found before in the time-domain results. These results prove that the stability approach used herein is applicable to the single-phase systems to obtain precise small-signal models for the stability characterization even with PLL for grid-synchronization.

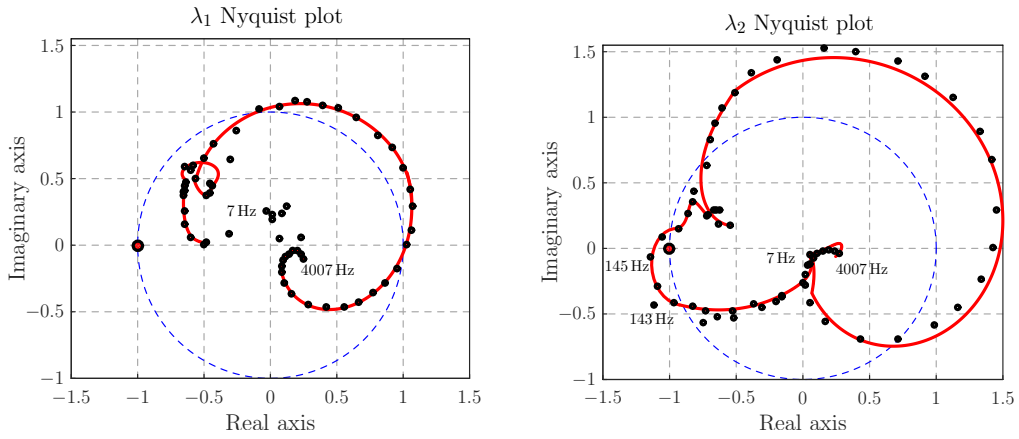

Figure 4.14: λ_1 and λ_2 Nyquist plots for unstable conditions: dots refer to experimental data and solid lines to interpolations [122]

4.7 Summary

So far different papers on small-signal stability analysis at a source-load interface have been proposed for DC and AC systems, for both three-phase and single-phase connections. This Chapter shows a method to identify a steady-state operation for single-phase AC systems that can be time-varying and nonlinear, enabling a small-signal impedance-based analysis. This analysis can be used to address the stability of the interactions of more and more DERs in microgrids and distribution grids. The approach used here exploits the dynamic averaging technique (dynamic phasors) leading to MIMO models that are analyzed with the Generalized Nyquist stability Criterion. The mathematical formulation and hypotheses on the final model result to be equivalent to the dq transformation approach, proposed to address the stability in three-phase AC systems. In this Chapter, this theory is validated experimentally, showing that it can be used for the stability analysis by injecting and measuring quantities at an electric port of the grid.

Chapter 5

Analysis of the dynamics of the distribution network

Distribution grid scenarios are very complex and varied, because of the presence of different types of device that work simultaneously and with different time scale characteristics, as introduced in Chapter 1. Pure steady-state or static analyses can not observe the phenomena generated by the interactions of these devices and so dynamic studies of the distribution grid are needed, both analytic and with simulation. Dynamic studies often use very detailed models for devices, loads and DERs, generating very complicated and less scalable approaches, poor load modeling, and so on [56].

This Chapter does not aim to focus on single-device stability and on its complete set of dynamics, but it wants to focus on the interactions of several units in the grid, approximating the dynamic contributions, and considering only those relevant during the interactions of these units. This drives to avoid the use of very detailed approaches for dynamic studies, while approximated analyses are preferred because they can address the stability of the grid as a whole. Moreover, this allows to obtain scalable models that are more handleable and meaningful for large grid studies [56].

For these reasons, the activity described herein aims to develop simplified models for the devices of the grid and then a scalable small-signal approach that links all the device models. Another important point to be considered is

the higher level algorithms, i.e. primary, secondary, and tertiary, of the grid that can influence the voltage stability [56]. Among different DER algorithms, an application of the Q/V local droop controller will be shown, because it is one of the most investigated in literature and because it has already been regulated by some country level standards, see Sec. 1.1.3 and [56].

This Chapter describes the research activity done during a visiting research period of the Author at the Institute Automation of Complex Power Systems of RWTH Aachen University (Germany), from January 2014 till October 2014. This work was done within a part of the European research project *IDE4L Project* [150]: it regards the study of the dynamics in distribution energy grids, considering a high penetrated scenario of DERs, completed with the writing of the report [56].

Some results from [56] are here described focusing on the development of a small-signal approach to address the stability of a high DG penetrated grid in Sec. 5.1. This approach is general and scalable and so it enables the study of a grid of generic size. In Sec. 5.2, an extension of this small-signal model is presented in order to account the effects of a primary level control, i.e. the Q/V droop control for voltage regulation support. Some simulation results of these models are described in Sec. 5.3, with an application to a real LV distribution grid test-bench.

5.1 Open-loop small-signal stability analysis

In this section, a small-signal model is described to study the dynamics of a distribution grid with a large penetration of DG, in an open-loop configuration. A linear model for the electric grid is first obtained and then a nonlinear model for the users (loads and generators) is proposed. From this model, through a linearization process, the small-signal model of all the users of the grid is written and then linked to the model of the electric grid. This result enables the dynamic study of the network and also the design of primary level controllers for DERs (Sec. 1.1).

The following analysis exploits the space vectors defined in the rotating

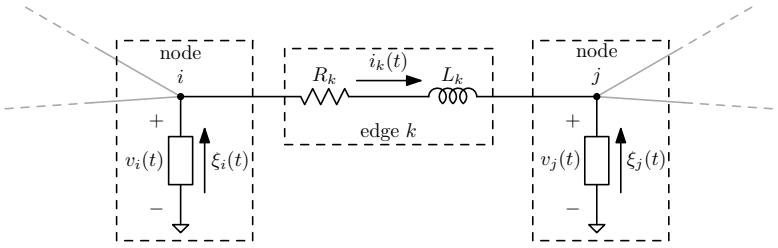

Figure 5.1: Edge of the network as RL line

reference frame, i.e. dq frame to describe currents and voltages of the grid (Sec. 1.2): all sinusoidal quantities can correctly be described even in presence of variations of amplitude and frequency, as also described in Chapter 2 and in Appendix A. For three-phase systems, the dq transformation is well defined, but this description can be applied also to single-phase systems considering them as a part of a fictitious three-phase system. That is, the single-phase system is considered as one of the three phases of a balanced and symmetric three-phase system and the other two phases derive from the first one after a phase shift of $120°$ and $240°$, respectively. More details are in Chapter 4 and in Appendix A.

5.1.1 Dynamic network model

Consider a single-phase resistive-inductive electric line, as in Fig. 5.1. If $i_k(t)$ is the instantaneous inductor current, the differential equation that relates instantaneous voltages and current is:

$$L_k \frac{\mathrm{d}i_k(t)}{\mathrm{d}t} = v_i(t) - v_j(t) - R_k i_k(t) \tag{5.1}$$

From now, the time dependencies are dropped for sake of simplicity.

If the RL line belongs to a three-phase system or to a single-phase one, it is possible to write the (5.1) with the space vectors defined in the dq reference frame, i.e. with (1.9) and (1.10):

$$L_k \frac{\mathrm{d}\mathbf{i}_{k,dq}}{\mathrm{d}t} = \mathbf{v}_{i,dq} - \mathbf{v}_{j,dq} - (R_k + j\omega_o L_k)\, \mathbf{i}_{k,dq} \tag{5.2}$$

where the dq transformation is performed on a reference frame that rotates with

the nominal angular frequency of the system, ω_o.

Now all the Kirchhoff's voltage laws (LKV) and Kirchhoff's current laws (LKI) of the grid are written in a compact form exploiting the matrix notation: a graph theory approach is used as in [52], assuming that the grid has N_n nodes and N_e edges or branches. All the LKV for the grid are:

$$L_k \frac{\mathrm{d}\mathbf{i}_k}{\mathrm{d}t} = \mathbf{v}_i - \mathbf{v}_j - (R_k + j\omega_o L_k)\,\mathbf{i}_k \qquad k = 1, \ldots, N_e \tag{5.3}$$

where all the space vectors are defined in the dq rotating reference frame (the dq subscripts are dropped) and k index identifies the edge of the graph with resistance R_k and inductance L_k. Also the subscripts i and j of $\mathbf{v}$ identify the nodes where the branch k is connected.

The *incidence matrix* A is defined as in [52] to write all the LKV (5.3):

$$A \in \{0,\, \pm 1\}^{N_e \times N_n} \tag{5.4a}$$

where:

$$a_{eu} \triangleq \begin{cases} -1 & \text{if the edge } e \text{ starts form the node } u \\ 1 & \text{if the edge } e \text{ arrives at the node } u \\ 0 & \text{otherwise} \end{cases} \tag{5.4b}$$

Define the two diagonal matrices L and R as:

$$L \triangleq \mathrm{diag}\,(L_1,\, L_2,\, \ldots,\, L_{N_e}) \in \mathbb{R}^{N_e \times N_e} \tag{5.5a}$$

$$R \triangleq \mathrm{diag}\,(R_1,\, R_2,\, \ldots,\, R_{N_e}) \in \mathbb{R}^{N_e \times N_e} \tag{5.5b}$$

where $\mathrm{diag}\,(\cdot)$ denotes a diagonal matrix having the entries of the vector as diagonal elements, and the two vectors $\mathbf{i}$ and $\mathbf{v}$ as:

$$\mathbf{i} \triangleq \begin{bmatrix} \mathbf{i}_1 & \mathbf{i}_2 & \cdots & \mathbf{i}_{N_e} \end{bmatrix}^T \in \mathbb{C}^{N_e \times 1} \tag{5.6a}$$

$$\mathbf{v} \triangleq \begin{bmatrix} \mathbf{v}_1 & \mathbf{v}_2 & \cdots & \mathbf{v}_{N_n} \end{bmatrix}^T \in \mathbb{C}^{N_n \times 1} \tag{5.6b}$$

Notice that $\mathbf{i}$ and $\mathbf{v}$ are complex vectors which contain the space vectors of all the edge currents and node voltages respectively.

Considering all the previous definitions, (5.4)-(5.6), the LKV (5.3) can be written in this compact form:

$$\frac{\mathrm{d}\mathbf{i}}{\mathrm{d}t} = -L^{-1}A\mathbf{v} - \left(L^{-1}R + j\omega_o\mathbb{I}_{N_e}\right)\mathbf{i} \tag{5.7}$$

considering that L is diagonal, and so invertible, and where $\mathbb{I}_{N_e}$ is the identity matrix of dimension $N_e \times N_e$.

Indicate with $\boldsymbol{\xi}_i$ the space vector (in the dq reference frame) of the current that is injected at the node i, for example by a load or a DER, as in Fig. 5.1. All the LKI can be written by summing all the currents that flow toward each node. Defining:

$$\boldsymbol{\xi} \triangleq \begin{bmatrix} \boldsymbol{\xi}_1 & \boldsymbol{\xi}_2 & \cdots & \boldsymbol{\xi}_{N_n} \end{bmatrix}^T \in \mathbb{C}^{N_n \times 1} \tag{5.8}$$

as the vector of all the space vectors that represent the node currents, a compact way to write all the LKI is [52]:

$$A^T\mathbf{i} + \boldsymbol{\xi} = 0 \tag{5.9}$$

Merging the LKV and LKI equations, respectively (5.7) and (5.9), the model of the grid results:

$$\begin{cases} \dfrac{\mathrm{d}\mathbf{i}}{\mathrm{d}t} &= -\left(L^{-1}R + j\omega_o\mathbb{I}_{N_e}\right)\mathbf{i} - L^{-1}A\mathbf{v} \\ \boldsymbol{\xi} &= -A^T\mathbf{i} \end{cases} \tag{5.10}$$

The model (5.10) results to be linear and described as state-space model: $\mathbf{i}$ is the state vector, $\mathbf{v}$ the input vector, and $\boldsymbol{\xi}$ the output vector.

All the matrices and vectors in (5.10) are complex and, to exploit the well-known results of the state-space theory, such model has to be expressed with

real-value matrices and vectors:

$$\begin{cases} \dfrac{\mathrm{d}i_r}{\mathrm{d}t} &= A_g i_r + B_g v_r \\ \xi_r &= C_g i_r \end{cases} \tag{5.11}$$

where:

$$i_r \triangleq \begin{bmatrix} \mathfrak{Re}\left[\mathbf{i}\right] \\ \mathfrak{Im}\left[\mathbf{i}\right] \end{bmatrix} \qquad A_g \triangleq \begin{bmatrix} -L^{-1}R & \omega_o \mathbb{I}_{N_e} \\ -\omega_o \mathbb{I}_{N_e} & -L^{-1}R \end{bmatrix} \tag{5.12a}$$

$$B_g \triangleq -\begin{bmatrix} L^{-1}A & 0 \\ 0 & L^{-1}A \end{bmatrix} \qquad v_r \triangleq \begin{bmatrix} \mathfrak{Re}\left[\mathbf{v}\right] \\ \mathfrak{Im}\left[\mathbf{v}\right] \end{bmatrix} \tag{5.12b}$$

$$\xi_r \triangleq \begin{bmatrix} \mathfrak{Re}\left[\boldsymbol{\xi}\right] \\ \mathfrak{Im}\left[\boldsymbol{\xi}\right] \end{bmatrix} \qquad C_g \triangleq \begin{bmatrix} -A^T & 0 \\ 0 & -A^T \end{bmatrix} \tag{5.12c}$$

5.1.2 Static network model

The *singular perturbation* theory describes how to approximate a differential equation system that has a set of *fast dynamics* and a set of *slow dynamics* [151] (Appendix A). With appropriate hypotheses, the set of faster equations in the system, i.e. the equations that describe the fast state variables, can be replaced by a set of algebraic equations. With this approximation, the model loses the information about fast modes, assuming their state variables always in a steady-state condition. In this way, the order of the differential equation system can be reduced, as well as the complexity of the system itself.

In a distribution grid, there are different time-scale dynamics and usually the dynamics of the electric cables can be considered as fast [56, 152]. This means that the differential equation system for the network dynamics, i.e. (5.10), describes fast dynamics within the differential equation system of the whole model of the system. So it is possible to approximate the dynamics of the grid with a static model for the dq space vectors at the nominal angular frequency ω_o. With other words, the dynamic model (5.10) can be approximated with a

full algebraic model by setting the time derivative of $\mathbf{i}$ equal to zero:

$$A\mathbf{v} + \mathbf{Z}\mathbf{i} = 0 \qquad \Rightarrow \qquad \mathbf{i} = -\mathbf{Z}^{-1}A\mathbf{v} \tag{5.13}$$

where $\mathbf{Z} \triangleq R + j\omega_o L \in \mathbb{C}^{N_e \times N_e}$ is diagonal and so invertible. Substituting (5.13) in the second equation of (5.10), it follows:

$$\boldsymbol{\xi} = \left(A^T\mathbf{Z}^{-1}A\right)\mathbf{v} \tag{5.14}$$

The model (5.14) is written with real-value matrices and vectors, as done with (5.11):

$$\xi_r = H_g v_r \tag{5.15}$$

where H_r is defined as:

$$H_g \triangleq \begin{bmatrix} \mathfrak{Re}\left[A^T\mathbf{Z}^{-1}A\right] & -\mathfrak{Im}\left[A^T\mathbf{Z}^{-1}A\right] \\ \mathfrak{Im}\left[A^T\mathbf{Z}^{-1}A\right] & \mathfrak{Re}\left[A^T\mathbf{Z}^{-1}A\right] \end{bmatrix} \tag{5.16}$$

and with the same definitions for ξ_r and v_r of (5.12).

5.1.3 PCC model

Among all the nodes of the grid, the PCC node connects the distribution grid to the higher voltage level, for example at the MV-LV transformer location for an LV distribution grid. Since the rated power of the main grid behind the PCC is very large compared to the considered part of the distribution grid, the PCC node is here described with an ideal voltage generator with a certain output impedance. This is usually done by several works on grid-connected operation for DERs, reported in Chapter 1 and in [56]. This modeling choice neglects the dynamics of the frequency, which is assumed to be constant. The impedance of the PCC is accounted by the edge that departs from this node.

Assuming the PCC is at the node 1, its model can be written as:

$$\mathbf{v}_{PCC} = \mathbf{v}_1 = V_o \in \mathbb{R} \qquad \forall \quad \boldsymbol{\xi}_1 \in \mathbb{C} \tag{5.17}$$

where the space vectors are used to represent the PCC node voltage $\mathbf{v}_1$ and its injected current $\boldsymbol{\xi}_1$. Since the dq space vector is constant, the PCC voltage results to be a sinusoidal waveform with angular frequency equal to the nominal one ω_o and with voltage amplitude equal to the nominal line to neutral voltage V_o.

Splitting (5.17) in its d and q components ($\mathbf{v}_1 = v_{1d} + jv_{1q}$), a small-signal model for the PCC results:

$$\Delta v_{1d} = 0 \tag{5.18a}$$

$$\Delta v_{1q} = 0 \tag{5.18b}$$

These components are null, because the space vector $\mathbf{v}_1$ is constant and so its real and imaginary components. The d and q subscripts indicate respectively the d and q components of a space vector or of a complex quantity.

5.1.4 Node model

The same model for each node of the grid is considered to make scalable and automatable the building of the final model. Each node consists of the parallel connection of (see Fig. 5.2):

- a series of a resistance and an inductance, that can roughly model a motor or other loads [56];
- a capacitor, that can be a real capacitor connected to the grid or the shunt capacitance of the cables;
- a constant power generator with a first-order dynamic of the current, that approximates a DER;
- a constant power load with a first-order dynamic of the current, that can model dynamic loads (for example inverter-interfaced loads).

By setting different parameters for these elements, different types of node can be described. More details on this choices and generality are in [56].

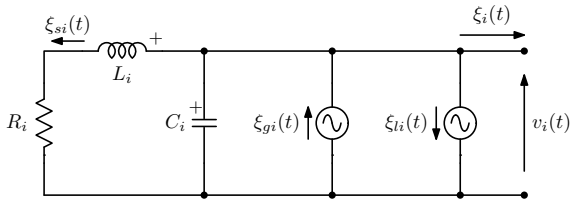

Figure 5.2: Schematic of the i-th node model [56]

From Fig. 5.2, the instantaneous voltages and currents of node i are described as:

$$C_i \frac{\mathrm{d}v_i(t)}{\mathrm{d}t} = \xi_{gi}(t) - \xi_{si}(t) - \xi_{li}(t) - \xi_i(t) \tag{5.19a}$$

$$L_i \frac{\mathrm{d}\xi_{si}(t)}{\mathrm{d}t} = v_i(t) - R_i \xi_{si}(t) \tag{5.19b}$$

Transforming (5.19) in the dq rotating reference frame, it results:

$$C_i \frac{\mathrm{d}\mathbf{v}_i}{\mathrm{d}t} = \boldsymbol{\xi}_{gi} - \boldsymbol{\xi}_{si} - \boldsymbol{\xi}_{li} - \boldsymbol{\xi}_i - j\omega_o C_i \mathbf{v}_i \tag{5.20a}$$

$$L_i \frac{\mathrm{d}\boldsymbol{\xi}_{si}}{\mathrm{d}t} = \mathbf{v}_i - (R_i + j\omega_o L_i)\, \boldsymbol{\xi}_{si} \tag{5.20b}$$

where the time dependencies (t) and the dq symbols are dropped. Observe that all the quantities have the subscript i because they are related to the node number $i = 2, \ldots, N_n$ ($i = 1$ is for the PCC).

Focusing on grid-connected inverters for PV applications, DER are usually controlled as grid-following devices which operate as current sources (Sec. 1.1.3). So DERs are dynamically modeled as current source with a first-order approximation on the active and reactive power tracking capabilities [56]. While the active power dynamic can be due to the speed of the MPPT algorithm [153], the reactive power dynamic can be due to the presence of a closed-loop regulation that adjusts the generated current [40]. The first-order model for the

constant power source and load is also used in [15]:

$$\tau_{gi}\frac{\mathrm{d}\boldsymbol{\xi}_{gi}}{\mathrm{d}t} = -\boldsymbol{\xi}_{gi} + 2\left(\frac{\mathbf{s}_{gi}}{\mathbf{v}_i}\right)^* \tag{5.21a}$$

$$\tau_{li}\frac{\mathrm{d}\boldsymbol{\xi}_{li}}{\mathrm{d}t} = -\boldsymbol{\xi}_{li} + 2\left(\frac{\mathbf{s}_{li}}{\mathbf{v}_i}\right)^* \tag{5.21b}$$

for the i-th node of Fig. 5.2, where $\mathbf{s}_{gi} = p_{gi} + jq_{gi} \in \mathbb{C}$ and $\mathbf{s}_{li} = p_{li} + jq_{li} \in \mathbb{C}$ are the complex power references respectively for the PV generator and the load. Consider that by setting a fast time-constant, the load behaves like a constant power load and, by setting a slow time constant, it can behave like a constant current load. This modeling choice can include and describe all the major load models [56].

Putting together (5.20) and (5.21), it is possible to obtain the complete model for the node i. The use of the dq space vectors allows to identify a steady-state operation for the model that can be linearized in order to study the small-signal stability (Chapter 4 and Appendix A). In this way, the small-signal model for the i-th node of the grid results:

$$\frac{\mathrm{d}}{\mathrm{d}t}\Delta z_i = D_{ni}\Delta z_i + E_{ni}\Delta\xi_i + G_{ni}\Delta s_i \qquad i = 2, \ldots, N_n \tag{5.22}$$

where the following definitions are used:

$$\Delta z_i \triangleq \begin{bmatrix}\Delta v_{di} & \Delta v_{qi} & \Delta\xi_{sdi} & \Delta\xi_{sqi} & \Delta\xi_{gdi} & \Delta\xi_{gqi} & \Delta\xi_{ldi} & \Delta\xi_{lqi}\end{bmatrix}^T \tag{5.23a}$$

$$\Delta\xi_i \triangleq \begin{bmatrix}\Delta\xi_{di} & \Delta\xi_{qi}\end{bmatrix}^T \in \mathbb{R}^{2\times 1} \tag{5.23b}$$

$$\Delta s_i \triangleq \begin{bmatrix}\Delta p_{gi} & \Delta q_{gi} & \Delta p_{li} & \Delta q_{li}\end{bmatrix}^T \in \mathbb{R}^{4\times 1} \tag{5.23c}$$

with $\Delta z_i \in \mathbb{R}^{8\times 1}$. The matrices D_{ni}, E_{ni}, and G_{ni} are suitable matrices that contain the partial derivatives obtained during the differentiation of (5.20) and (5.21): these matrices are not reported here explicitly for sake of explanation, but all the mathematical details can be found in [56].

Since, the grid models, (5.11) and (5.15), receive as input the voltages of all the nodes, the outputs of the node model is chosen as the node voltages Δv_{di}

and Δv_{qi}:

$$\Delta v_i = F_{ni} \Delta z_i \tag{5.24a}$$

where

$$F_{ni} = \begin{bmatrix} 1 & 0 & 0 & 0 & 0 & 0 & 0 & 0 \\ 0 & 1 & 0 & 0 & 0 & 0 & 0 & 0 \end{bmatrix} \in \mathbb{R}^{2\times 8} \tag{5.24b}$$

and

$$\Delta v_i = \begin{bmatrix} \Delta v_{di} \\ \Delta v_{qi} \end{bmatrix} \in \mathbb{R}^{2\times 1} \tag{5.24c}$$

Merging (5.22) and (5.24) for all the nodes of the grid, the model results:

$$\begin{cases} \dfrac{\mathrm{d}}{\mathrm{d}t}\Delta z &= D_n \Delta z + E_n \Delta \xi_r + G_n \Delta s \\ \Delta v_r &= F_n \Delta z \end{cases} \tag{5.25}$$

where these definitions are used, extending (5.23):

$$\Delta z \triangleq \begin{bmatrix} z_2^T & z_3^T & \cdots & z_{N_n}^T \end{bmatrix}^T \in \mathbb{R}^{8(N_n-1)\times 1} \tag{5.26a}$$

$$\Delta \xi_r \triangleq \begin{bmatrix} \xi_1^T & \xi_2^T & \cdots & \xi_{N_n}^T \end{bmatrix}^T \in \mathbb{R}^{2N_n\times 1} \tag{5.26b}$$

$$\Delta s \triangleq \begin{bmatrix} s_2^T & s_3^T & \cdots & s_{N_n}^T \end{bmatrix}^T \in \mathbb{R}^{4(N_n-1)\times 1} \tag{5.26c}$$

$$\Delta v_r \triangleq \begin{bmatrix} v_1^T & v_2^T & \cdots & v_{N_n}^T \end{bmatrix} \in \mathbb{R}^{2N_n\times 1} \tag{5.26d}$$

and these definitions extending the matrices of (5.22):

$$D_n \triangleq \operatorname{diag}\left(D_{n2},\, D_{n3},\, \ldots,\, D_{nN_n}\right) \in \mathbb{R}^{8(N_n-1)\times 8(N_n-1)} \tag{5.27a}$$

$$E_n \triangleq \left[\begin{array}{cc|cccc} 0 & 0 & E_{n2} & & & \\ 0 & 0 & & E_{n3} & & \\ \vdots & \vdots & & & \ddots & \\ 0 & 0 & & & & E_{nN_n} \end{array}\right] \in \mathbb{R}^{8(N_n-1)\times 2N_n} \tag{5.27b}$$

$$F_n \triangleq \left[\begin{array}{cccc} 0 & 0 & \dots & 0 \\ 0 & 0 & \dots & 0 \\ \hline F_{n2} & & & \\ & F_{n3} & & \\ & & \ddots & \\ & & & F_{nN_n} \end{array}\right] \in \mathbb{R}^{2N_n \times 4(N_n-1)} \tag{5.27c}$$

$$G_n \triangleq \operatorname{diag}\left(G_{n2},\, G_{n3},\, \dots,\, G_{nN_n}\right) \in \mathbb{R}^{8(N_n-1)\times 4(N_n-1)} \tag{5.27d}$$

Observe that two null columns are added to the matrix E_n, because the vector $\Delta\xi_r$ has as first elements the PCC currents, as defined in (5.26b). Similarly, two null rows are added to the matrix F_n to account the PCC voltage components that are in the vector Δv_r, as defined in (5.26d).

5.1.5 Overall small-signal model

Once the model of all nodes (5.25) and model of the grid, (5.11) or (5.15), are obtained the model of the complete system can be evaluated linking them together. Observe that the models (5.11) and (5.15) are linear and so they can describe the whole quantities i_r, ξ_r, and v_r as well as their small-signal variations, i.e. Δi_r, $\Delta\xi_r$, and Δv_r, in the same manner.

Notice that the arrangements of vectors $\Delta\xi_r$ and Δv_r in (5.25) and in (5.11) or (5.15) are different, and for this reason some row and column permutations are needed in the E_n and F_n matrices before joining the two models. These trivial details are skipped for briefness reasons [56]. The model (5.25) and (5.11) can be linked to obtain the overall small-signal model:

$$\frac{\mathrm{d}}{\mathrm{d}t}\begin{bmatrix}\Delta z \\ \Delta i_r\end{bmatrix} = \underbrace{\begin{bmatrix} D_n & E_n C_g \\ B_g F_n & A_g \end{bmatrix}}_{A_{tot}} \begin{bmatrix}\Delta z \\ \Delta i_r\end{bmatrix} + \underbrace{\begin{bmatrix} G_n \\ 0 \end{bmatrix}}_{B_{tot}} \Delta s \tag{5.28}$$

On the other hand, merging (5.25) and (5.15), it results:

$$\frac{\mathrm{d}\Delta z}{\mathrm{d}t} = \underbrace{(D_n + E_n H_g F_n)}_{A_{tot}} \Delta z + \underbrace{G_n}_{B_{tot}} \Delta s \tag{5.29}$$

Now the evaluation of the eigenvalues of the matrix A_{tot} in (5.28) or (5.29) allows to study the dynamics of distribution grid, under the hypotheses of approximation done in this section. This can be done for an open-loop configuration, that is with constant power references for the loads and DERs, i.e. constant. However, the standard tools of state-space feedback control theory can be used to design controllers, either local or centralized, for the DERs that set their power references with respect to some feedback variables [56]. One example is described in the next section for the Q/V droop control for grid support.

5.2 Local Q/V droop control application

The small-signal model presented in Sec. 5.1 is now extended to study the Q/V droop control described in Sec. 1.1.3. Since Q/V droop control sets the reactive power references in Δs based on the measurements of the voltage amplitude, the voltage amplitude for each node is evaluated starting from the state Δz which contains the voltage variations of the d and q components, in (5.28) or (5.29). Consider an inverter that is connected at the node i with the voltage $\mathbf{v}_i = v_{di} + jv_{qi}$. The voltage amplitude V_i is related to the real and imaginary components as:

$$|\mathbf{v}_i| = V_i = \sqrt{{v_{di}}^2 + {v_{qi}}^2} \tag{5.30}$$

and linearizing this equation:

$$\Delta V_i = \frac{V_{di}}{\sqrt{{V_{di}}^2 + {V_{qi}}^2}} \Delta v_{di} + \frac{V_{qi}}{\sqrt{{V_{di}}^2 + {V_{qi}}^2}} \Delta v_{qi} \tag{5.31}$$

where V_{di} and V_{qi} refer to the steady-state d and q components of the node voltage where the linearization is performed, and Δv_{di} and Δv_{qi} refer to their small-signal variations. V_i and ΔV_i are respectively the voltage amplitude steady-state solution and its small-signal variation.

Writing the (5.31) for all the nodes of the grid, the variations of the voltage amplitudes can be written according to the variations of the d and q components of all the nodes. Remembering that these last quantities are included in the state vector of the grid model (in particular in Δz), for example in (5.28), it results:

$$\Delta V = \begin{bmatrix} T_{ctr} & 0 \end{bmatrix} \begin{bmatrix} \Delta z \\ \Delta i_r \end{bmatrix} \tag{5.32}$$

where

$$\Delta V \triangleq \begin{bmatrix} \Delta V_1 & \Delta V_2 & \cdots & \Delta V_{N_n} \end{bmatrix}^T \in \mathbb{R}^{N_n \times 1} \tag{5.33}$$

and $T_{ctr} \in \mathbb{R}^{N_n \times 8(N_n-1)}$ is a suitable matrix containing the linearizations (5.31) for all the nodes, and where the subdivision of the two matrices is done accordingly. A similar relation can be obtained also from the model in (5.29) [56].

The Q/V droop control model for all the DERs of the grid is again represented with a small-signal state-space model, that is:

$$\begin{cases} \dfrac{\mathrm{d}\Delta V_m}{\mathrm{d}t} &= -\Omega \Delta V_m + \Omega \Delta V \\ \Delta s &= K_{ctr} \Delta V_m \end{cases} \tag{5.34}$$

All the modeling details can be found in [56], while here only brief description and discussion are reported.

To apply the Q/V droop characteristic, the inverter controller has to measure the amplitude voltage at its terminals. In order to describe this measurement in the mathematical model, first-order filters are used to get the measured voltage amplitude ΔV_m from the actual voltage amplitude ΔV (for their variations): this leads to the first equation of (5.34), where Ω is a suitable matrix of time constants of the first-order filters. These filters can also account and set the speed of droop regulations, as some standards impose [7].

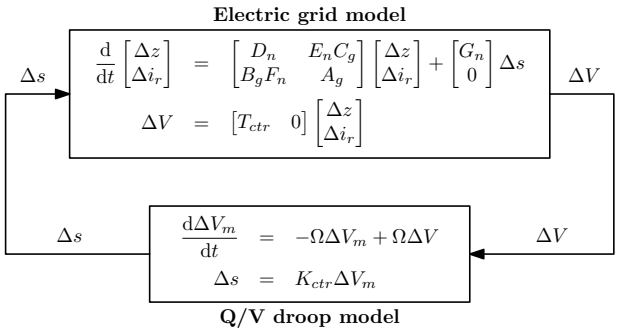

Figure 5.3: Representation of the closed-loop model from the complete grid model (5.28) and the Q/V droop controller model (5.34) [56]

Once the voltage amplitude measurement is described, the reactive power reference of the inverter is changed according to the Q/V droop characteristic (Sec. 1.1.3). Since a small-signal model is needed, the Q/V droop characteristic is linearized as (for node i):

$$\Delta q_{gi} = -k_{vi}\Delta V_{mi} \tag{5.35}$$

where k_{vi} is the slope of the curve in the particular operating point where the linearization is performed (it can be a positive or null number). Including (5.35) for all the inverters of the grid, the second equation of (5.34) is obtained, with a suitable K_{ctr} matrix [56].

Merging the complete grid model (5.28) with (5.34), it is possible to evaluate the closed-loop state-space model. Similarly, a reduced order model results from (5.29) and (5.34) [56]. The feedback model is represented in Fig. 5.3 for the complete grid model (5.28). Once the state-space model of the closed-loop system is calculated, an eigenvalue analysis of the state matrix can be done to study the dynamics of the closed-loop system and to design properly the regulator (5.34).

Summarizing, an approach to address the small-signal stability analysis is proposed: it allows both the study of the dynamics of the distribution grid as a whole and also the design of a primary level control for DERs. Indeed, first an open-loop configuration of the grid was analyzed, that is when the DERs receive constant power references, and then a closed-loop configuration with the

Q/V droop control for DERs was introduced as in [56]. This approach to study distribution grid stability and dynamics, compared to others in literature, is detailed since it considers the load dynamics and the coupled power dependencies due to cables with low X/R ratio and also it is scalable and easily applicable to grids of generic number of nodes, thanks to the matrix notation herein exploited. In the next section, this model is applied to a real LV distribution grid test-bench to study its dynamic behavior and also to address the impacts of Q/V droop control on the grid stability, through simulations.

5.3 Simulation results for a real distrbution grid test-bench

In this section, some results obtained from the small-signal analysis described in this Chapter are shown together with some time-domain simulations. In particular, both the open-loop configuration, that is the distribution grid with constant power references for the inverters, as in Sec. 5.1, and the closed-loop system, referring to the local Q/V droop control, as in Sec. 5.2 are investigated.

5.3.1 Test-bench description

All the results of this Chapter are based on the A2A grid test-bench that is described in detail in [56]. This grid is an LV three-phase network with a nominal frequency of $\omega_o = 2\pi 50\,\mathrm{rad/s}$ and nominal line to neutral peak voltage of $V_o = 230\sqrt{2}\,\mathrm{V}$. The grid has $N_e = 41$ edges and $N_n = 42$ nodes where all the users and generators are single-phase connected (with neutral wire): the grid results unbalanced and asymmetric. For this reason, the study is performed phase-per-phase and here only one phase is considered, since similar results can be found for the others [56].

The description of the cables is in Tab. 5.1, while the details of the topology and the lengths of the electric cables are reported in Tab. 5.2. Information about the users, in terms of rated power and DG capabilities, is provided in Tabs. 5.3 and 5.4.

Table 5.1: Cable description of the A2A LV grid test-bench [56]

Cable code	G5OCR	RG7OCR	RG7CR
Material	Copper	Copper	Copper
Cross Section $[\,\mathrm{mm}^2\,]$	3x95+1x50C	3x50+1x25C	1x6+6C
Max current $[\,\mathrm{A}\,]$	249	166	62
$R\ [\,\Omega/\mathrm{km}\,]$	0.25	0.391	3.11
$X@50\,\mathrm{Hz}\ [\,\Omega/\mathrm{km}\,]$	0.07	0.0779	0.092

For the dynamic study, these choices are done [56]:

- the PV units inject all the nominal power at unity PF, during the open-loop operation ($q_{gi} = 0$);
- 40% of the load rated power is given by the linear RLC load, while the remaining 60% is from the dynamic power load (Sec. 5.1.4);
- all the constant power loads have a PF of 0.85 (inductive), while the RLC loads have a 0.9 inductive PF;
- the time constants of the PV generator models, i.e. τ_{gi} in (5.21a), are set randomly between $5\,\mathrm{ms}$ and $30\,\mathrm{ms}$ (they are different from one node to the other);
- the time constants of the load models, i.e. τ_{li} in (5.21b), are set randomly between $1\,\mathrm{ms}$ and $5\,\mathrm{s}$ (they are different from one node to the other).

Table 5.2: Electric line description of the A2A LV grid test-bench [56]

MV/LV substation	LV Line ID	Start node	End node	Length [m]	Code	Phase
1056	6	SS1056	Condo	49	RG7OCR	3
1056	8	SC1	C01	18	RG7CR	1
1056	8	SC1	C02	18	RG7CR	1
1056	8	SC1	C03	18	RG7CR	1
1056	8	SC1	C04	18	RG7CR	1
1056	8	SC2	C05	33	RG7CR	1
1056	8	SC2	C06	39	RG7CR	1
1056	8	SC2	C07	36	RG7CR	1
1056	8	SC2	C08	34	RG7CR	1
1056	8	SC2	C09	22	RG7CR	1
1056	8	SC2	C10	26	RG7CR	1
1056	8	SC2	C11	15	RG7CR	1
1056	8	SC2	C12	19	RG7CR	1
1056	8	SC2	C13	9	RG7CR	1
1056	8	SC2	C14	15	RG7CR	1
1056	8	SC2	C15	14	RG7CR	1
1056	8	SC2	C16	13	RG7CR	1
1056	8	SC2	C17	9	RG7CR	1
1056	8	SC2	C18	16	RG7CR	1
1056	8	SC2	C19	21	RG7CR	1
1056	8	SC2	C20	22	RG7CR	1
1056	8	SC2	C21	28	RG7CR	1
1056	8	SC2	C22	30	RG7CR	1
1056	8	SC2	SC1	69	G5OCR	3
1056	8	SC3	C23	31	RG7CR	1
1056	8	SC3	C24	35	RG7CR	1
1056	8	SC3	C25	22	RG7CR	1
1056	8	SC3	C26	28	RG7CR	1
1056	8	SC3	C27	16	RG7CR	1
1056	8	SC3	C28	22	RG7CR	1
1056	8	SC3	C29	9	RG7CR	1
1056	8	SC3	C30	17	RG7CR	1
1056	8	SC3	C31	8	RG7CR	1
1056	8	SC3	C32	17	RG7CR	1
1056	8	SC3	C33	13	RG7CR	1
1056	8	SC3	C34	21	RG7CR	1
1056	8	SC3	C35	20	RG7CR	1
1056	8	SC3	C36	26	RG7CR	1
1056	8	SC3	C37	28	RG7CR	1
1056	8	SC3	C38	32	RG7CR	1
1056	8	SC3	SC2	94	RG7OCR	3
1056	8	SS1056	SC1	204	RG7OCR	3

Table 5.3: Node description of the A2A LV grid test-bench (part 1) [56]

Line	Customer ID	Phase	Contractual Power [kW]	PV Peak Power [kW]	Comment
8	C01		4.5		Not active
8	C02		4.5		Not active
8	C03	A	4.5	1.296	
8	C04	B	4.5	1.296	
8	C05	C	4.5	/	
8	C06	A	4.5	/	
8	C07	C	4.5	1.296	
8	C08	B	4.5	1.296	
8	C09	B	4.5	1.296	
8	C10	A	4.5	1.296	
8	C11	B	4.5	1.296	
8	C12	C	4.5	1.296	
8	C13	C	4.5	1.296	
8	C14	A	4.5	1.296	
8	C15	B	4.5	1.296	
8	C16	C	4.5	1.296	
8	C17	B	4.5	1.296	
8	C18	A	4.5	1.296	
8	C19	A	4.5	1.296	
8	C20	C	4.5	1.296	
8	C21	B	4.5	1.296	
8	C22	A	4.5	1.296	
8	C23	A	4.5	1.296	
8	C24	B	4.5	1.296	
8	C25	C	4.5	1.296	
8	C26	A	4.5	1.296	

Table 5.4: Node description of the A2A LV grid test-bench (part 2) [56]

Line	Customer ID	Phase	Contractual Power [kW]	PV Peak Power [kW]	Comment
8	C27	B	4.5	1.296	
8	C28	C	4.5	1.296	
8	C29	A	4.5	1.296	
8	C30	B	4.5	1.296	
8	C31	C	4.5	1.296	
8	C32	A	4.5	1.296	
8	C33	B	4.5	1.296	
8	C34	C	4.5	1.296	
8	C35	A	4.5	1.296	
8	C36	B	4.5	1.296	
8	C37	C	4.5	1.296	
8	C38	A	4.5	1.296	
6	C39	A	4.5	/	
6	C40	C	4.5	/	
6	C41	B	4.5	/	
6	C42	A	4.5	/	
6	C43	C	4.5	/	
6	C44	B	4.5	/	
6	C45	A	4.5	/	
6	C46	A	4.5	/	
6	C47	C	4.5	/	
6	C48	B	4.5	/	
6	C49	C	4.5	/	
6	C50				Not active
6	C51	ABC			Not active
6	C52	ABC	15	/	
6	C53	ABC	30	3	Condominium

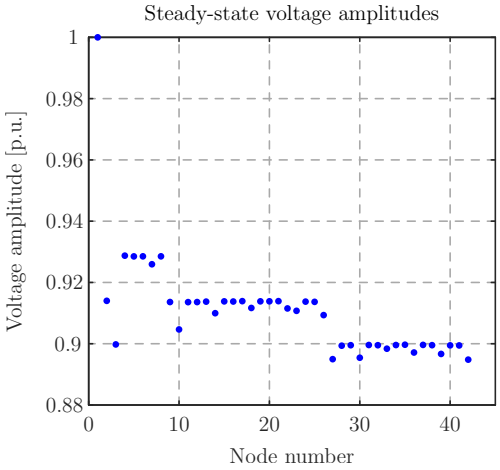

Figure 5.4: Steady-state voltage amplitudes for the open-loop grid model [56]

5.3.2 Open-loop dynamic results

The eigenvalue analysis presented in Sec. 5.1 is now used to study the dynamic characteristics of the grid in an open-loop configuration. In Fig. 5.4, there are the steady-state voltage amplitudes of all nodes where the linearization is performed.

The dynamic study of the grid is done in terms of eigenvalue analysis of the matrix A_{tot} of the full order model (5.28), while more results and comparisons for the reduced order model (5.29) can be found in [56]. The sets of eigenvalues that will be shown have absolute values that range from factions of 1 up to 10^6, and for this reason they are represented in complex planes after applying this compressing function:

$$\mathbf{g}_i \in \mathbb{C} \quad : \quad \mathbf{f}(\mathbf{g}_i) = \begin{cases} \mathbf{g}_i & \text{if } |\mathbf{g}_i| \leq 1 \\ \mathbf{g}_i \frac{1+\log|\mathbf{g}_i|}{|\mathbf{g}_i|} & \text{otherwise} \end{cases} \tag{5.36}$$

This means that the complex planes that are shown do not contain the eigenvalues $\mathbf{g}_i$ as they are, but they show $\mathbf{f}(\mathbf{g}_i)$. This operation makes more readable the graphs.

Fig. 5.5 shows the eigenvalues of the A_{tot} matrix of the model (5.28) to evaluate the dynamic characteristics of the grid, in terms of modes of the system:

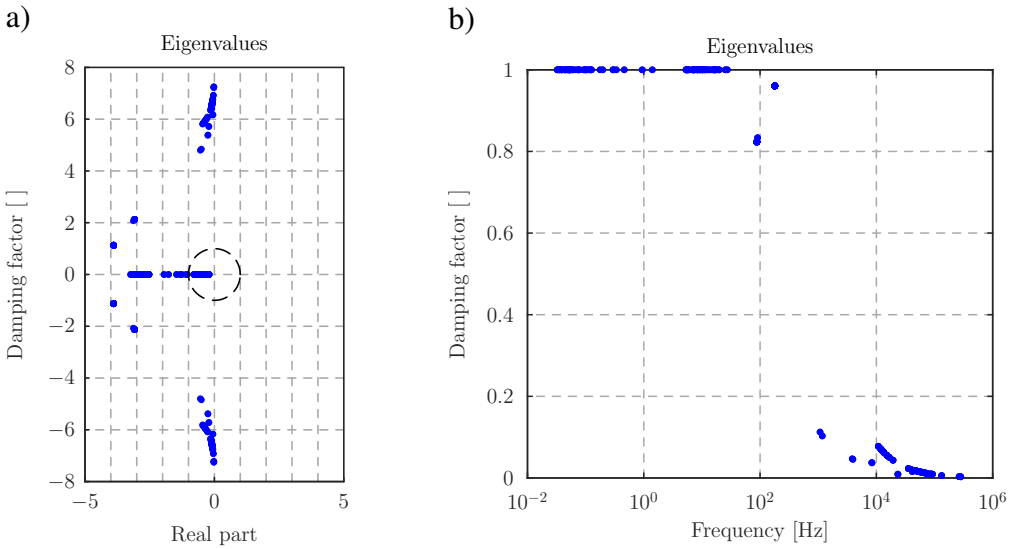

Figure 5.5: Eigenvalues of the matrix A_{tot} of (5.28) for the test-bench of Sec. 5.3.1: a) on the complex plane applying the function $\mathbf{f}(\cdot)$ of (5.36) and b) with damping factor as function of frequency [56]

remember that among the states of the model there are all the voltages of the grid. The eigenvalues are shown in the complex plane, by applying the function $\mathbf{f}(\cdot)$ of (5.36), and also with the damping factor as function of the frequency of the eigenvalue, that is its absolute value divided by 2π [56].

The presence of modes in a very extended range of frequencies can be observed: they have all negative real parts, leading to a stable small-signal dynamic system. The slowest modes of the system are real eigenvalues, while some complex conjugate eigenvalues appear at frequencies near $100\,\mathrm{Hz}$.

The reduced order model (5.29) can also be used to perform this analysis: it only introduces some approximations in the description of the fastest modes of the system, as anticipated in Sec. 5.1.2, and so its results may have a limited validity in terms of frequency [56]. However, the important dynamic behaviors of the grid that are the slowest dynamics are well described also by the model (5.29) [56].

5.3.3 Closed-loop dynamic results

The effects of the Q/V droop control is discussed with the small-signal analysis, considering the complete model of the grid given by (5.28) and (5.34), as in Sec. 5.2. The eigenvalues of the state matrix of system given by the feedback of Fig. 5.3 are compared with those of the open-loop model (5.28), to see how the dynamic characteristics of the grid are affected by the primary level voltage control given by the Q/V droop.

It is assumed that all the PV DERs work within the droop area and not within the dead-bands of the curve in Fig. 1.9, irrespective of the output voltage. This means that all the k_v parameters for all the nodes are set to be different from zero, leading to the worst-case scenario of the impact of such regulation [56].

The results of Fig. 5.6 are for the closed-loop system with a *slow* time response for the droop controllers: the first-order filters described in Sec. 5.2 have a bandwidth equal to one tenth of the line frequency, i.e. $\omega_o/10$, for all the DERs. The droop control affects slightly some poles with intermediate frequencies, near $10\,\mathrm{Hz}$: these differences can be seen comparing Figs. 5.5 and 5.6: a slow voltage measurement causes the reduction of the damping factors of such eigenvalues. If faster droop regulations are considered the reduction of the damping factor is less visible [56].

5.3.4 Time-domain results

This section shows some time-domain simulations of the small-signal model and some comparisons with the initial nonlinear model. The small-signal model used for simulation is (5.28) as in Secs. 5.3.2 and 5.3.3, while the nonlinear models used here, one for the open-loop system and another for the closed-loop system, consider the nonlinearity due to the node model of Sec. 5.1.4. Moreover, the nonlinear closed-loop model includes also the nonlinearity of the real Q/V droop curve as in Fig. 1.9. Once again, the bandwidth of the voltage measurement considered is equal to $\omega_o/10$ for all the DERs.

Comparisons between the small-signal model (5.28) and the nonlinear open-loop systems for the response to a step change of the active power reference of

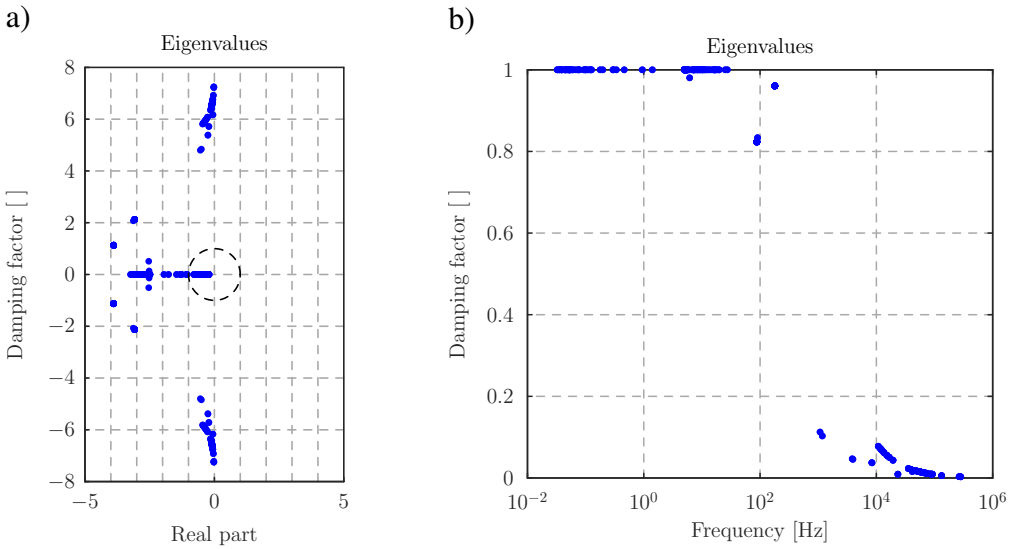

Figure 5.6: Eigenvalues of the closed-loop system given by (5.28) and (5.34) for a bandwidth for the voltage amplitude measurement of $\omega_o/10$ for all the DERs, for the test-bench of Sec. 5.3.1: a) on the complex plane applying the function $\mathbf{f}(\,\cdot\,)$ of (5.36) and b) with damping factor as function of frequency [56]

the inverter at node C35 (Tab. 5.4) are shown in: Fig. 5.7 for voltage amplitude variation, and Fig. 5.8 for voltage phase variation. The results are reported in terms of variations with respect to the steady-state solution for the node C29 (Tab. 5.4). The transient is triggered by a step reduction of the active power reference of the inverter connected at node C35 of $1\,\mathrm{kW}$ at $t = 3\,\mathrm{s}$ [56].

Comparisons between the nonlinear open-loop and closed-loop systems for the response to a step change of the active power reference of the inverter at node C35 are shown in: Fig. 5.9 for voltage amplitude variation, Fig. 5.10 for voltage phase variation, and Fig. 5.11 for active and reactive powers injected by the PCC. The results are again reported in terms of variations with respect to the steady-state solution for the node C29. The transient is triggered by a step reduction of the active power reference of the inverter connected at node C35 of $1\,\mathrm{kW}$ at $t = 3\,\mathrm{s}$ [56].

From these results, it is possible to observe that the dynamic models presented in this Chapter describe both very slow dynamics (orders of tens of seconds) and fast dynamics (orders of milliseconds). In Figs. 5.7 and 5.8, the results of the small-signal open-loop model and the results for the nonlinear

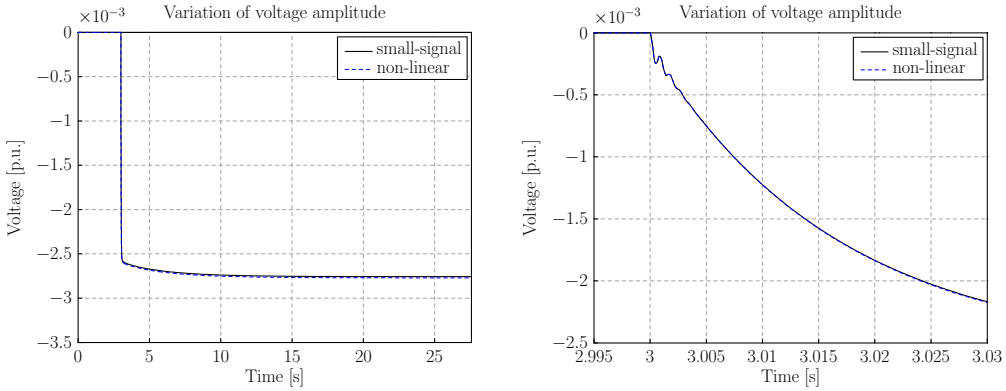

Figure 5.7: Voltage amplitude variation from the steady-state solution for the node C29 after a step reduction of 1 kW of the active power reference of the DER at node C35: comparison between the small-signal open-loop model (5.28) in solid line, and the nonlinear open-loop model in dashed line [56]

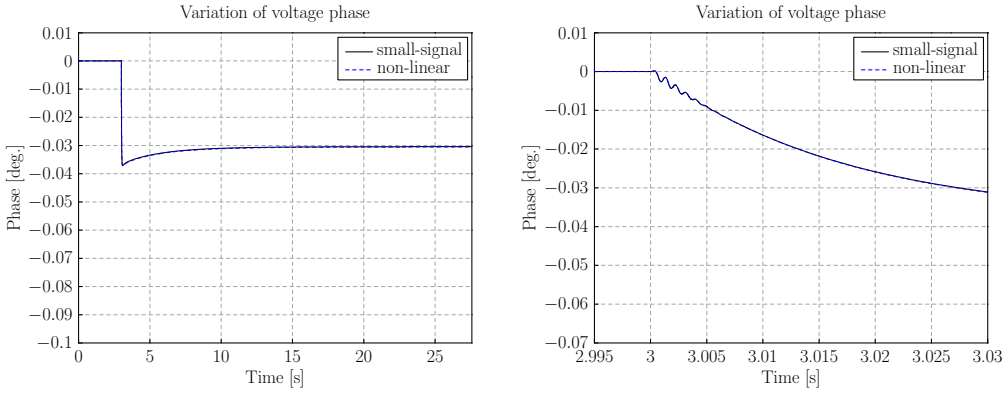

Figure 5.8: Voltage phase variation from the steady-state solution for the node C29 after a step reduction of 1 kW of the active power reference of the DER at node C35: comparison between the small-signal open-loop model (5.28) in solid line, and the nonlinear open-loop model in dashed line [56]

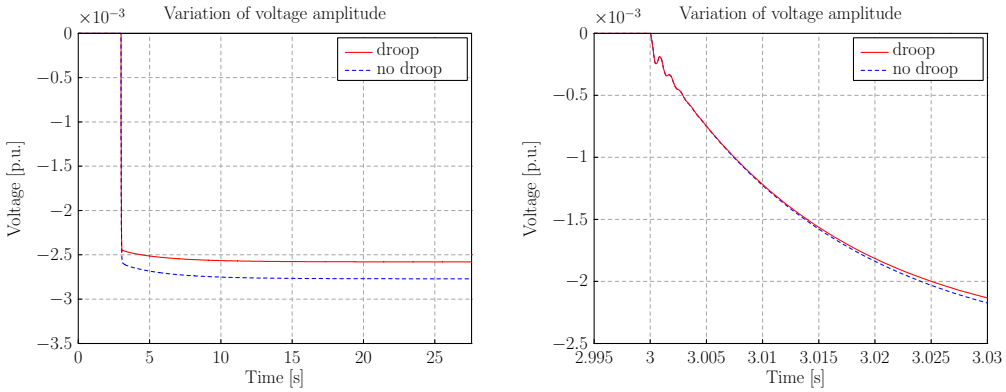

Figure 5.9: Voltage amplitude variation from the steady-state solution for the node C29 after a step reduction of 1 kW of the active power reference of the DER at node C35: comparison between the nonlinear open-loop (dashed line) and closed-loop (solid line) models [56]

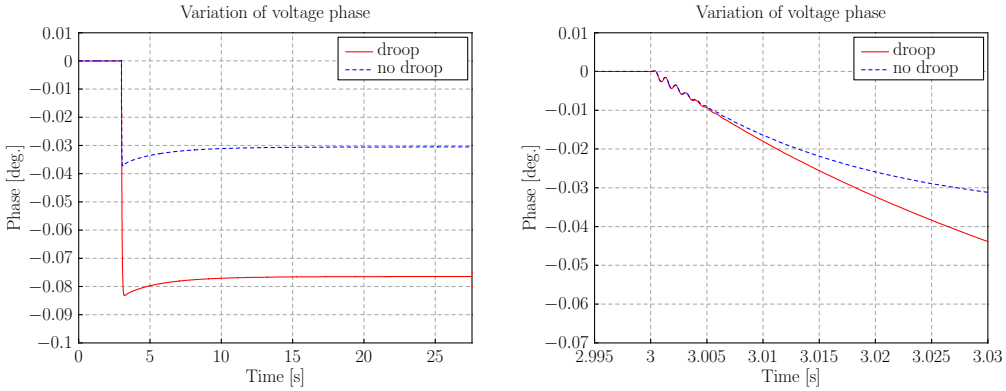

Figure 5.10: Voltage phase variation from the steady-state solution for the node C29 after a step reduction of 1 kW of the active power reference of the DER at node C35: comparison between the nonlinear open-loop (dashed line) and closed-loop (solid line) models [56]

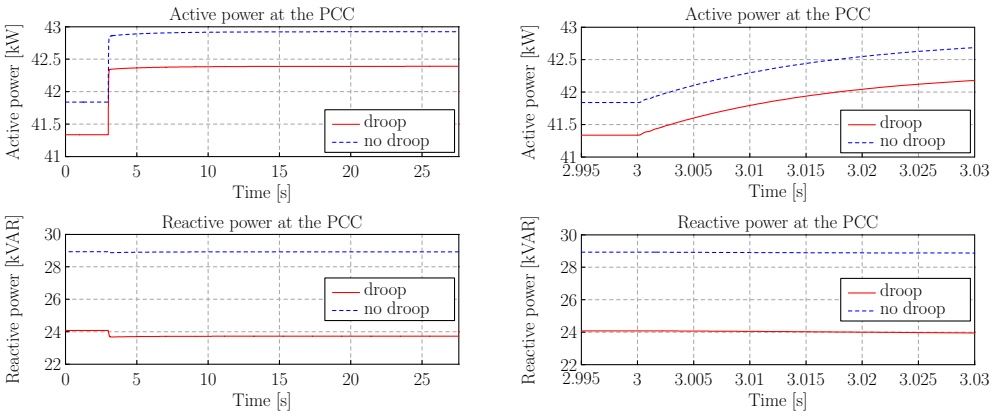

Figure 5.11: Active and reactive powers injected at the PCC after a step reduction of 1 kW of the active power reference of the DER at node C35: comparison between the nonlinear open-loop (dashed line) and closed-loop (solid line) models [56]

open-loop model are almost overlapped, meaning that the small-signal model describes quite well the nonlinear initial system. It is interesting to observe from Fig. 5.9, that the droop control can limit the steady-state voltage variation at the node C29 for the considered transient, but its effect is limited. On the other hand, the reactive power injection has more influence on the voltage phase variation rather than on the voltage amplitude one (compare Figs. 5.9 and 5.10), because the X/R ratio of the cables is quite small (Sec. 1.1.2). From Fig. 5.11, injecting reactive power with the DERs seems to be an effective way to keep the PF of the PCC closer to 1, as anticipated in Sec. 1.1.3.

5.4 Summary

This Chapter addresses the dynamic and the stability studies of distribution grids with large penetration of DG. Since some instability issues can be due to the interactions of a multitude of grid devices as shown in Sec. 1.2 and in [56], the analysis proposed here focuses on the characterization of the grid as a whole, rather than focusing on the the single device stability. This is done with simplified dynamic models for loads and DERs, that then are linked in a small-signal state-space model. The result is a scalable approach for the dynamic analysis, that can address the study of a grid with a generic number of node,

with no more effort by the user. Also some control architectures can potentially worsen the stability of the grid operation and so the modeling discussed in this Chapter includes the possibility to account and design high level controllers for the devices of the grid, in particular Q/V droop control for voltage regulation support is considered.

The results coming from a real LV distribution grid test-bench, are given in terms of both eigenvalue analyses and of time-domain simulations. From all these results and from those in [56], it appears that there are different types of dynamics within the distribution grid systems and they are quite separated in terms of frequency: there are fast dynamics of the cables with sub-millisecond time responses, dynamics of the inverters an their primary controllers with time scale of tens of milliseconds or hundreds of milliseconds and, finally, load dynamics that can last for hundreds of milliseconds up to tens of seconds [56]. Of course, if secondary and/or tertiary controllers (Sec. 1.1) are included other dynamic behaviors can appear.

Chapter 6

Conclusions

This Thesis depicts the distribution grid scenario as a very complex and varied environment, where several kinds of device and control algorithm can interact and work simultaneously. The penetration of renewable energy sources is driving a great spread of power electronics converters as interfaces for the energy sources. A proper control and management of these devices, exploiting the capabilities of the inveter control, can help improve the overall distribution grid performances and provide new functionalities. On the other hand, inverters can introduce fast dynamics and nonlinear behaviors that can worsen the distribution grid normal operation or introduce additional risks for the operation.

In this scenario, this Thesis described a local controller for the distributed energy resources in order to improve the reliability of a microgrid, even when the mains disconnect. This regulator can manage a microgrid in both islanded and grid-connected operating modes, and it can achieve the seamless microgrid transition from grid-connected to autonomous mode without any time-critical communication. The controller exploits P/f and Q/V droop control to share the load power in islanded operation and feedback control to track power references in grid-connected operation.

The other contributions of the Thesis are related to possible risks associated to the distributed energy resources: the instability concerns and the unintentional islanded operation. Regarding the first, this Thesis proposes an experimental method to address the single-phase AC system stability, that in general

is not a trivial problem because of the time-varying behavior and the nonlinearities of these systems. The method described in this Thesis allows to identify a steady-state operation for single-phase AC systems, enabling a small-signal impedance-based analysis. This analysis can be used to address the stability of the interactions of more and more distributed energy resources in microgrids and distribution grids, which are usually single-phase connected. Again in this scenario, another contribution of this Thesis is an approach to study the stability and the dynamics of distribution grids with large penetration of distributed generation. Such method focuses on the characterization of the grid as a whole, rather than focusing on the single device stability. The result is a scalable approach for the dynamic analysis, that can address the study of a grid with a generic number of node, and also it allows the analysis and the design of some high level control architectures.

The last contribution of this Thesis is an assessment of the risk of permanent and temporary unintentional islanding. The results show that unintentional islanding operation can appear in distribution grids because of the load and source dependencies of active and reactive powers to the voltage and frequency of the grid. In particular, P/f and Q/V droop curves that are imposed by new standards for PV connections can increase such risk. Furthermore, it was observed that the speed of response of the P/f and Q/V droop functions increases the unintentional islanding risk. As solution, the non-simultaneous operation of P/f and Q/V resulted an effective approach to reduce this risk and an online method based on this was proposed and validated.

Appendix A

Generalized stability analysis for droop controlled microgrids

In this Appendix the approach of [154] is described to study the stability of a droop controlled microgrid with a generic number of DERs. This is a simplified method which neglects fast dynamics of the system but keeps a sufficient accuracy to describe the interactions of several droop controlled inverters. This stability analysis bases on a small-signal model of the system. Whereas other papers as [19, 155] have already proposed models at a similar level of detail, here a generalized method is described to generate a mathematical model for a grid with a generic number of inverters without increasing the complexity of the analysis. This enables a powerful method for the design of droop controllers in networks of arbitrary complexity.

This Appendix is organized as follows: Sec. A.1 describes the key features of the analysis introduced afterwards, while the mathematical model of the process is described in Sec. A.2 and that of the regulator in Sec. A.3. Finally Sec. A.4 describes how to merge the two models and how to design the droop regulators for a microgrid of arbitrary size.

A.1 General considerations on the approach

Droop control techniques consist of setting the voltage amplitude V_i and the angular frequency ω_i of the i-th inverter (with $i = 1 \dots n$ where n is the number of inverters of the microgrid) from the output active and reactive power measurements of the inverter itself, as described in Sec. 1.1.2. The measurements of active and reactive power are intrinsically slow, especially in single-phase systems or three-phase systems in unbalanced conditions due to the ripple on the instantaneous power quantities at twice the line frequency. While several filters can be used for the extraction of the average power terms, for the purpose of explanation, a simple first-order one is used here as in (3.14) and in [18, 19]:

$$\begin{cases} p_{mi} &= \dfrac{\omega_c}{s+\omega_c} p_i \\ q_{mi} &= \dfrac{\omega_c}{s+\omega_c} q_i \end{cases} \qquad \text{for} \quad i = 1 \dots n \tag{A.1}$$

where p_{mi} and q_{mi} are measured active and reactive powers at the output of the i-th inverter and p_i and q_i are actual active and reactive powers at output of the i-th inverter. The filter bandwidth is smaller than the line angular frequency and thus droop controllers can achieve slow dynamics well-below the line frequency. The same filter for every inverter of the grid is here considered in order to simplify the analysis, however it is possible to easily extend the results for filters with different time constants. On the other hand, the filter structure can be potentially more complex: for example with a higher order filter or a moving average filter (commonly used for single-phase systems). Here the particular filtering structure is approximated with a first order filter to make the mathematical description simpler.

Fig. A.1 shows an example of a simplified microgrid with droop control. The *Inverter* blocks receive the references of instantaneous phase and amplitude to be tracked and impose the voltages to the *electric grid and load* block; S_m blocks evaluate the active and the reactive powers from output currents and voltages of each inverter; they also contain the first-order filters (A.1). These powers are used as input for the droop regulators to set angular frequency and

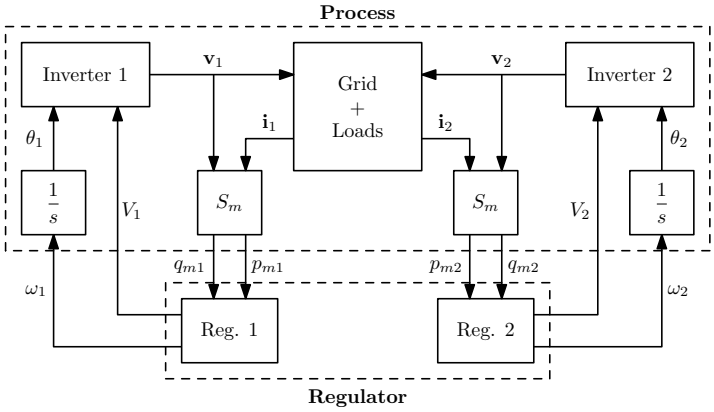

Figure A.1: Block diagram of a simple microgrid with droop control (θ_i are angles in the abc domain)

voltage amplitude for the inverters. The basic droop scheme described in (1.8) with constant p_s and q_s is here considered. Notice that the choice of the specific droop controller is arbitrary and the model that will be presented in the following sections can be extended to any other droop scheme.

The following points qualitatively describe the peculiarities of the proposed model, which is described in details afterward:

- the model neglects fast dynamics of the system by exploiting results of *singular perturbation theory* [151]: a theorem provides a tool to simplify nonlinear mathematical model by approximating "faster" differential equations in a mathematical model with algebraic equations. The neglected fast dynamics are related to the inner control loops (current and voltage loops) and to the output filters of inverters and to the electric grid. This approximation is possible under certain hypotheses, but especially when there are other variables in the system with slower dynamics. In the case under study, these variables are the measurements of powers at the outputs of the inverters. With these approximations, the model loses the information about fast modes, assuming the state variables associated to these modes to be in steady-state.
- The model of the grid is linearized around the steady-state solution.
- A simplified model can speed up and make easier the design of droop

regulators.

The generality of the proposed method is due to the use of matrices that describe synthetically and easily systems of any size. In fact, it is possible to consider a system composed by a generic number n of inverters, and model it by linearization. The proposed tool is based on the use of space vectors defined in the rotating reference frame (Sec. 1.2): this makes possible to describe exactly currents and voltages of the grid. In particular, its application correctly describes all the sinusoidal quantities, even in the presence of small and slow variations of amplitude and frequency. For three-phase systems the dq transformation is well defined, but this description can be applied also to single-phase systems, considering them as a part of a fictitious balanced three-phase system (see Chapter 4). That is, the single-phase system is one of the three phases of a balanced three-phase system and the other two phases derive from the first one after a phase shift of $120°$ and $240°$, respectively. The adoption of the space vectors allows also to apply the results of the *singular perturbation* theory, neglecting the fast dynamics of the microgrid and reducing the order of the mathematical model of the network.

As a result, a small-signal model of the physical system can be obtained. This model is split into two state-space models: one describes the process, including the combination of inverters, electric grid, and loads, and the other describes the droop regulators that calculate all the angular frequencies and voltage amplitudes to create the voltage references for the inverters. The overall small-signal model is represented by the feedback of these two models, as shown in Fig. A.2.

A.2 Process model

Referring to the state-space models of the Fig. A.2, the state vector Δx of the process contains the variations of all measured active and reactive powers of all inverters from the steady-state solution and it also contains the variations

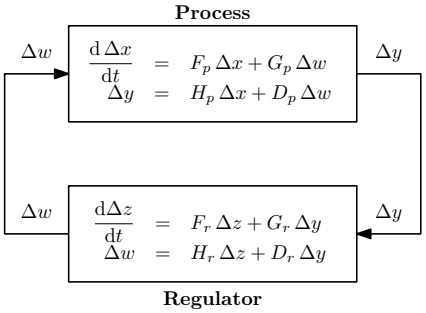

Figure A.2: Small-signal model of process and regulator

of all instantaneous phases φ_i.

$$\Delta x \triangleq \begin{bmatrix} \Delta p_{m1} & \Delta p_{m2} & \cdots & \Delta q_{m1} & \Delta q_{m2} & \cdots & \Delta\varphi_1 & \Delta\varphi_2 & \cdots \end{bmatrix}^T \tag{A.2}$$

where $\Delta x \in \mathbb{R}^{3n\times 1}$. The input vector Δw of the process contains the variations of all amplitude voltage references V_i and all the variations of angular frequency references for the inverters:

$$\Delta w \triangleq \begin{bmatrix} \Delta V_1 & \Delta V_2 & \cdots & \Delta\omega_1 & \Delta\omega_2 & \cdots \end{bmatrix}^T \in \mathbb{R}^{2n\times 1} \tag{A.3}$$

The output vector Δy of the process model contains the variations of all measured active and reactive powers and therefore corresponds to the state Δx excluding the phases $\Delta\varphi_i$. The regulator receives as input the output Δy of the process and computes all the references Δw for the inverters. Define the vector Δs_m which contains the variations of measured powers from the steady-state solution:

$$\Delta s_m \triangleq \begin{bmatrix} \Delta p_{m1} & \Delta p_{m2} & \cdots & \Delta q_{m1} & \Delta q_{m2} & \cdots \end{bmatrix}^T = \Delta y \in \mathbb{R}^{2n\times 1} \tag{A.4}$$

Observe that Δs_m is equal to the output Δy, but conceptually it has a different meaning: Δs_m is a sub-vector of the state Δx and Δy is the output of the process model. Define also the vector Δs of variations of actual powers:

$$\Delta s \triangleq \begin{bmatrix} \Delta p_1 & \Delta p_2 & \cdots & \Delta q_1 & \Delta q_2 & \cdots \end{bmatrix}^T \in \mathbb{R}^{2n\times 1} \tag{A.5}$$

Writing the differential equations of the filters (A.1) of all the inverters and re-arranging them in real-value vectors it follows:

$$\frac{\mathrm{d}}{\mathrm{d}t}\Delta s_m = \omega_c \left(\Delta s - \Delta s_m\right) \tag{A.6}$$

Observe that it is possible to describe filters with different time constants by replacing ω_c with a suitable diagonal matrix.

Now, the vector Δs of the actual powers has to be written as a function of the space vectors of voltages and currents. For the i-th inverter and defining the space vectors in the rotating reference frame dq:

$$\mathbf{s}_i = \frac{1}{2}\mathbf{v}_i\ \mathbf{i}_i^* = \frac{1}{2}\left(v_{id} + jv_{iq}\right)\left(i_{id} - ji_{iq}\right) \tag{A.7}$$

where $\mathbf{s}_i$ is the complex power generated from the i-th inverter, $\mathbf{v}_i = v_{id} + jv_{iq}$ is its output voltage and $\mathbf{i}_i = i_{id} + ji_{iq}$ is its delivered current. Equation (A.7) is nonlinear, but through linearization, the variations of powers can be expressed in terms of variations of real and imaginary parts of space vectors of currents and voltages. By using the matrix notation all these linearized relations for $\mathbf{s}_i$ can be expressed in the following compact form:

$$\Delta s = H_1 \Delta v + H_2 \Delta i \tag{A.8}$$

where the vectors $\Delta v,\ \Delta i \in \mathbb{R}^{2n\times 1}$ are defined in this way:

$$\Delta v \triangleq \begin{bmatrix} \Delta v_{1d} & \Delta v_{2d} & \cdots & \Delta v_{1q} & \Delta v_{2q} & \cdots \end{bmatrix}^T \tag{A.9a}$$

$$\Delta i \triangleq \begin{bmatrix} \Delta i_{1d} & \Delta i_{2d} & \cdots & \Delta i_{1q} & \Delta i_{2q} & \cdots \end{bmatrix}^T \tag{A.9b}$$

and the matrices result:

$$H_1 = \frac{1}{2}\left[\begin{array}{ccc|ccc} I_{1d} & 0 & \cdots & I_{1q} & 0 & \cdots \\ 0 & I_{2d} & \cdots & 0 & I_{2q} & \cdots \\ \vdots & \vdots & \ddots & \vdots & \vdots & \ddots \\ \hline -I_{1q} & 0 & \cdots & I_{1d} & 0 & \cdots \\ 0 & -I_{2q} & \cdots & 0 & I_{2d} & \cdots \\ \vdots & \vdots & \ddots & \vdots & \vdots & \ddots \end{array}\right] \tag{A.10a}$$

$$H_2 = \frac{1}{2}\left[\begin{array}{ccc|ccc} V_{1d} & 0 & \cdots & V_{1q} & 0 & \cdots \\ 0 & V_{2d} & \cdots & 0 & V_{2q} & \cdots \\ \vdots & \vdots & \ddots & \vdots & \vdots & \ddots \\ \hline V_{1q} & 0 & \cdots & -V_{1d} & 0 & \cdots \\ 0 & V_{2q} & \cdots & 0 & -V_{2d} & \cdots \\ \vdots & \vdots & \ddots & \vdots & \vdots & \ddots \end{array}\right] \tag{A.10b}$$

where $H_1, H_2 \in \mathbb{R}^{2n\times 2n}$. Upper-case letters indicate the operating point values where the linearization is carried out. Notice that the matrices H_1 and H_2 result easily extensible in the case of a grid with n inverters because they always contain four diagonal sub-matrices.

With the admittance matrix it is possible to write a relation between the space vectors of currents and voltages. These relations can be split in real-value equations. By defining:

$$Y_r \triangleq \left[\begin{array}{ccc|ccc} Y_{11d} & Y_{12d} & \cdots & -Y_{11q} & -Y_{12q} & \cdots \\ Y_{21d} & Y_{22d} & \cdots & -Y_{21q} & -Y_{22q} & \cdots \\ \vdots & \vdots & \ddots & \vdots & \vdots & \ddots \\ \hline Y_{11q} & Y_{12q} & \cdots & Y_{11d} & Y_{12d} & \cdots \\ Y_{21q} & Y_{22q} & \cdots & Y_{21d} & Y_{22d} & \cdots \\ \vdots & \vdots & \ddots & \vdots & \vdots & \ddots \end{array}\right] \in \mathbb{R}^{2n\times 2n} \tag{A.11}$$

it follows:

$$\Delta i = Y_r \Delta v \tag{A.12}$$

Here it is possible to introduce the description of some inputs for the model. For instance, a load with fixed absorbed current (as input of the model) can be added by writing $\Delta i = Y_r \Delta v + N \Delta r$ in place of (A.12), where Δr is a vector of the d and q components of a current load and N is a suitable matrix. These inputs are not accounted in the following analysis for sake of simplicity, but it can be extended if they are present.

Substituting (A.12) in (A.8) and then all in (A.6) it follows:

$$\frac{\mathrm{d}}{\mathrm{d}t}\Delta s_m = \omega_c \left[\left(H_1 + H_2 Y_r \right) \Delta v - \Delta s_m \right] \tag{A.13}$$

The next step is to describe Δv as a function of variables that are contained in the state vector Δx and in the input vector Δw, i.e. as a function of variations $\Delta \varphi_i$ (in Δx) and ΔV_i (in Δw). To do this, the following equation which relates the real and the imaginary parts of the space vectors $\mathbf{v}_i$ to their magnitudes and phases is linearized:

$$\begin{aligned} &\mathbf{v}_i = v_{id} + j v_{iq} = V_i e^{j\varphi_i} \qquad \Rightarrow \\ &\quad \Rightarrow \Delta \mathbf{v}_i = e^{j\varphi_i} \Delta V_i + j V_i e^{j\varphi_i} \Delta \varphi_i = \frac{\mathbf{v}_i}{V_i} \Delta V_i + j \mathbf{v}_i \Delta \varphi_i \end{aligned} \tag{A.14}$$

and evaluating the real and the imaginary parts the final linearized equations are obtained:

$$\Delta v_{id} = \mathfrak{Re}\left[\Delta \mathbf{v}_i \right] = \frac{V_{id}}{V_i} \Delta V_i - V_{iq} \Delta \varphi_i \tag{A.15a}$$

$$\Delta v_{iq} = \mathfrak{Im}\left[\Delta \mathbf{v}_i \right] = \frac{V_{iq}}{V_i} \Delta V_i + V_{id} \Delta \varphi_i \tag{A.15b}$$

With the previous relations, the matrix equation that links the vector Δv to the variations of magnitudes and phases of the space vectors can be easily built.

To this aim, define:

$$U \triangleq \left[\begin{array}{ccc|ccc} \frac{V_{1d}}{V_1} & 0 & \cdots & -V_{1q} & 0 & \cdots \\ 0 & \frac{V_{2d}}{V_2} & \cdots & 0 & -V_{2q} & \cdots \\ \vdots & \vdots & \ddots & \vdots & \vdots & \ddots \\ \hline \frac{V_{1q}}{V_1} & 0 & \cdots & V_{1d} & 0 & \cdots \\ 0 & \frac{V_{2q}}{V_2} & \cdots & 0 & V_{2d} & \cdots \\ \vdots & \vdots & \ddots & \vdots & \vdots & \ddots \end{array}\right] \in \mathbb{R}^{2n\times 2n} \tag{A.16}$$

Now it is possible to write:

$$\begin{aligned} \Delta v &= \begin{bmatrix} \Delta v_{1d} & \Delta v_{2d} & \cdots & \Delta v_{1q} & \Delta v_{2q} & \cdots \end{bmatrix}^T = \\ &= U \begin{bmatrix} \Delta V_1 & \Delta V_2 & \cdots & \Delta \varphi_1 & \Delta \varphi_2 & \cdots \end{bmatrix}^T \end{aligned} \tag{A.17}$$

and expressing the last vector in terms of the state Δx and the input Δw:

$$\begin{bmatrix} \Delta V_1 & \Delta V_2 & \cdots & \Delta \varphi_1 & \Delta \varphi_2 & \cdots \end{bmatrix}^T = C_1 \Delta x + C_2 \Delta w \tag{A.18}$$

with:

$$C_1 \triangleq \left[\begin{array}{c|c} 0 & 0 \\ \hline 0 & \mathbb{I}_n \end{array}\right] \in \mathbb{R}^{2n\times 3n} \tag{A.19a}$$

$$C_2 \triangleq \left[\begin{array}{c|c} \mathbb{I}_n & 0 \\ \hline 0 & 0 \end{array}\right] \in \mathbb{R}^{2n\times 2n} \tag{A.19b}$$

where $\mathbb{I}_n$ is the identity matrix of dimensions $n \times n$.

Replacing (A.19) into (A.13) and observing that $\Delta s_m = C_3 \Delta x$ with $C_3 \triangleq \begin{bmatrix} \mathbb{I}_{2n} & 0 \end{bmatrix} \in \mathbb{R}^{2n\times 3n}$, it follows:

$$\frac{\mathrm{d}}{\mathrm{d}t}\Delta s_m = \omega_c \left[\left(H_1 + H_2 Y_r\right) U C_1 - C_3 \right] \Delta x + \omega_c \left(H_1 + H_2 Y_r\right) U C_2 \Delta w \tag{A.20}$$

Writing the process model as in Fig. A.2:

$$\begin{cases} \dfrac{\mathrm{d}\,\Delta x}{\mathrm{d}t} &= F_p\,\Delta x + G_p\,\Delta w \\ \Delta y &= H_p\,\Delta x + D_p\,\Delta w \end{cases} \tag{A.21a}$$

and recalling that between the variations of the instantaneous phases $\Delta\varphi_i$ and of the instantaneous angular frequencies $\Delta\omega_i$ there is a derivative operation, it is possible to get F_p and G_p matrices of the process:

$$F_p = \omega_c \left[\begin{array}{c} (H_1 + H_2 Y_r)\,UC_1 - C_3 \\ \hline 0 \end{array}\right] \in \mathbb{R}^{3n\times 3n} \tag{A.21b}$$

$$G_p = \left[\begin{array}{c|c} \omega_c\,(H_1 + H_2 Y_r)\,UC_2 & \\ \hline 0 & \mathbb{I}_n \end{array}\right] \in \mathbb{R}^{3n\times 2n} \tag{A.21c}$$

and the matrices H_p and G_p:

$$H_p = \left[\mathbb{I}_{2n} \quad 0\right] \in \mathbb{R}^{2n\times 3n} \tag{A.21d}$$

$$D_p = 0 \in \mathbb{R}^{2n\times 2n} \tag{A.21e}$$

because the regulator acts only on the basis of the measurements of active and reactive powers. In this particular case the output of the process model results $\Delta y = \Delta s_m$.

With this method the matrices of the linearized model of the process are obtained. For a given network topology, the model of the process can be built following (A.2)-(A.21d), independently on the specific droop control law that will be applied.

A.3 Regulator model

A droop regulator receives as inputs the measured powers of each inverter and gives as outputs the amplitude and the angular frequency of the voltage reference for the same electronic interface. So the state-space model of a generic

droop regulation scheme can be written in this form:

$$\begin{cases} \dfrac{\mathrm{d}\Delta z}{\mathrm{d}t} &= F_r\,\Delta z + G_r\,\Delta y \\ \Delta w &= H_r\,\Delta z + D_r\,\Delta y \end{cases} \tag{A.22}$$

where $\Delta z \in \mathbb{R}^{m\times 1}$. Notice that the dimension m of the state Δz of the controller depends on the particular type of droop controller.

A.4 Overall model

Combining the model of the process (A.21a) (observe that $D_p = 0$) with that of the regulator (A.22), it results:

$$\frac{\mathrm{d}\Delta x}{\mathrm{d}t} = (F_p + G_p\,D_r\,H_p)\,\Delta x + G_p\,H_r\,\Delta z \tag{A.23a}$$

$$\frac{\mathrm{d}\Delta z}{\mathrm{d}t} = G_r\,H_p\,\Delta x + F_r\Delta z \tag{A.23b}$$

Now, let $\Delta g \triangleq \left[\,\Delta x^T\ \Delta z^T\,\right]^T \in \mathbb{R}^{(3n+m)\times 1}$ be an expanded state for the whole model which is the union of Δx (of dimension $3n$) and Δz (of dimension m). In this way, the whole model (A.23) can be written in this compact form:

$$\frac{\mathrm{d}\Delta g}{\mathrm{d}t} = F\,\Delta g \tag{A.24}$$

where:

$$F \triangleq \left[\begin{array}{c|c} F_p + G_p\,D_r\,H_p & G_p\,H_r \\ \hline G_r\,H_p & F_r \end{array}\right] \in \mathbb{R}^{(3n+m)\times(3n+m)} \tag{A.25}$$

The overall mathematical model describes an autonomous system without references for the regulators. In fact, droop control manages an islanded microgrid where the load power has to be properly shared among different energy sources.

The stability can now be studied with the eigenvalue analysis of the linearized model, which is an approximation of the complete system behavior

close to a particular operating point. Observe that all the matrices depend on the operating point.

Taking as example the droop controller in (1.8) with constant p_s and q_s, a state for the regulator is not necessary, since the control action is instantaneous. A small-signal model of the regulator leads to

$$\begin{cases} \Delta\omega_i &= -k_{pi}\,\Delta p_{mi} \\ \Delta V_i &= -k_{qi}\,\Delta q_{mi} \end{cases} \qquad \text{for} \quad i = 1 \dots n \tag{A.26}$$

Writing these equations for all the n inverters of the grid and remembering the definition of Δw in (A.3) and Δy in (A.4), it follows:

$$\Delta w = D_r\,\Delta y \tag{A.27}$$

where:

$$D_r = \left[\begin{array}{ccc|ccc} 0 & 0 & \cdots & -k_{q1} & 0 & \cdots \\ 0 & 0 & \cdots & 0 & -k_{q2} & \cdots \\ \vdots & \vdots & \ddots & \vdots & \vdots & \ddots \\ \hline -k_{p1} & 0 & \cdots & 0 & 0 & \cdots \\ 0 & -k_{p2} & \cdots & 0 & 0 & \cdots \\ \vdots & \vdots & \ddots & \vdots & \vdots & \ddots \end{array}\right] \tag{A.28}$$

In this case, combining the model of the process with that of the regulator (A.27), the state-space model (A.24) has:

$$F = F_p + G_p\,D_r\,H_p \;\in\; \mathbb{R}^{3n\times 3n} \tag{A.29}$$

A method to obtain a small-signal model for the entire microgrid where the inverters are controlled by the droop regulation (1.8) has been obtained for sake of explanation. However, notice that this method is more general and it allows to study the stability of a more complex droop controlled grid, for example with different kinds of regulator [34, 35], with virtual impedance technique [31, 32], etc. In fact, the only part that has to be changed to account different kinds of

regulator is the state-space model of the controller (A.22) or the output vector of the process model Δy.

The mathematical model described in this Appendix is tested and validated with Matlab/Simulink simulations in [154]. In particular, simulations of an extended islanded microgrid, which includes 16 nodes with 8 DERs and 7 linear loads, are performed therein.

Bibliography

[1] F. Katiraei and J. Agüero, "Solar PV integration challenges," *IEEE Power and Energy Magazine*, vol. 9, no. 3, pp. 62–71, May 2011.

[2] A. Ipakchi and F. Albuyeh, "Grid of the future," *IEEE Power and Energy Magazine*, vol. 7, no. 2, pp. 52–62, Mar 2009.

[3] F. Katiraei, R. Iravani, N. Hatziargyriou, and A. Dimeas, "Microgrids management," *IEEE Power and Energy Magazine*, vol. 6, no. 3, pp. 54–65, 2008.

[4] Enel Distribuzione, Workshop on "Uncontrolled islanding phenomena in distribution networks", Rome, Italy, April 2014.

[5] J. von Appen, M. Braun, T. Stetz, K. Diwold, and D. Geibel, "Time in the sun: The challenge of high PV penetration in the german electric grid," *IEEE Power and Energy Magazine*, vol. 11, no. 2, pp. 55–64, March 2013.

[6] S. Steffel and A. Dinkel, "Absorbing the rays: Advanced inverters help integrate PV into electric utility distribution systems," *IEEE Power and Energy Magazine*, vol. 11, no. 2, pp. 45–54, March 2013.

[7] CEI Comitato Elettrotecnico Italiano, "Standard-CEI 0-21, reference technical rules for the connection of active and passive users to the LV electrical utilities," 2011-12, standards.

[8] R. Sgarbossa, S. Lissandron, P. Mattavelli, R. Turri, and A. Cerretti, "Analysis of load-induced unintentional islanding in low voltage grids

with PV generators," in *2014 IEEE 15th Workshop on Control and Modeling for Power Electronics (COMPEL)*, June 2014.

[9] J. Guerrero, J. Vasquez, J. Matas, L. de Vicuña, and M. Castilla, "Hierarchical control of droop-controlled AC and DC microgrids - A general approach toward standardization," *IEEE Transactions on Industrial Electronics*, vol. 58, no. 1, pp. 158–172, Jan 2011.

[10] J. Rocabert, A. Luna, F. Blaabjerg, and P. Rodríguez, "Control of power converters in AC microgrids," *IEEE Transactions on Power Electronics*, vol. 27, no. 11, pp. 4734–4749, Nov 2012.

[11] "IEEE standard for interconnecting distributed resources with electric power systems," *IEEE Std 1547-2003*, pp. 1–28, July 2003.

[12] R. Lasseter, "Microgrids," in *IEEE Power Engineering Society Winter Meeting 2002*, vol. 1, 2002, pp. 305–308.

[13] S. Ashabani and Y.-R. Mohamed, "New family of microgrid control and management strategies in smart distribution grids - analysis, comparison and testing," *IEEE Transactions on Power Systems*, vol. 29, no. 5, pp. 2257–2269, Sept 2014.

[14] J. Vasquez, J. Guerrero, J. Miret, M. Castilla, and L. de Vicuña, "Hierarchical control of intelligent microgrids," *IEEE Industrial Electronics Magazine*, vol. 4, no. 4, pp. 23–29, Dec 2010.

[15] S. Bolognani, G. Cavraro, F. Cerruti, and A. Costabeber, "A linear dynamic model for microgrid voltages in presence of distributed generation," in *2011 IEEE First International Workshop on Smart Grid Modeling and Simulation (SGMS)*, Oct 2011, pp. 31–36.

[16] M. Chandorkar, D. Divan, and R. Adapa, "Control of parallel connected inverters in standalone AC supply systems," *IEEE Transactions on Industry Applications*, vol. 29, no. 1, pp. 136–143, Jan 1993.

[17] A. Tuladhar, K. Jin, T. Unger, and K. Mauch, "Parallel operation of single phase inverter modules with no control interconnections," in *Applied Power Electronics Conference and Exposition (APEC '97)*, vol. 1, 1997, pp. 94–100 vol.1.

[18] J. Guerrero, L. Garcia de Vicuña, J. Matas, M. Castilla, and J. Miret, "A wireless controller to enhance dynamic performance of parallel inverters in distributed generation systems," *IEEE Transactions on Power Electronics*, vol. 19, no. 5, pp. 1205–1213, 2004.

[19] E. Coelho, P. Cortizo, and P. Garcia, "Small-signal stability for parallel-connected inverters in stand-alone ac supply systems," *IEEE Transactions on Industry Applications*, vol. 38, no. 2, pp. 533–542, Mar 2002.

[20] Q.-C. Zhong and T. Hornik, *Control of Power Inverters in Renewable Energy and Smart Grid Integration*. Wiley-IEEE Press, Jan 2013.

[21] J. Kim, J. Guerrero, P. Rodriguez, R. Teodorescu, and N. Kwanghee, "Mode adaptive droop control with virtual output impedances for an inverter-based flexible AC microgrid," *IEEE Transactions on Power Electronics*, vol. 26, no. 3, pp. 689–701, March 2011.

[22] F. Katiraei and M. Iravani, "Power management strategies for a microgrid with multiple distributed generation units," *IEEE Transactions on Power Systems*, vol. 21, no. 4, pp. 1821–1831, Nov 2006.

[23] G. Andersson, "Electric Power Systems - Electric power transmission and distribution," Sept. 2009, EEH - Power Systems Laboratory - ETH Zürich.

[24] A. R. Bergen and V. Vittal, *Power Systems Analysis, 2nd Edition*. Prentice Hall, 2000.

[25] A. Engler and N. Soultanis, "Droop control in LV-grids," in *International Conference on Future Power Systems*, 2005.

[26] A. Hasanzadeh, O. Onar, H. Mokhtari, and A. Khaligh, "A proportional-resonant controller-based wireless control strategy with a reduced number of sensors for parallel-operated UPSs," *IEEE Transactions on Power Delivery*, vol. 25, no. 1, pp. 468–478, 2010.

[27] S. Iyer, M. Belur, and M. Chandorkar, "A generalized computational method to determine stability of a multi-inverter microgrid," *IEEE Transactions on Power Electronics*, vol. 25, no. 9, pp. 2420–2432, 2010.

[28] L. Xinchun, F. Feng, D. Shanxu, K. Yong, and C. Jian, "Modeling and stability analysis for two paralleled UPS with no control interconnection," in *IEEE International Electric Machines and Drives Conference 2003 (IEMDC'03)*, vol. 3, 2003, pp. 1772–1776.

[29] K. De Brabandere, "Voltage and frequency droop control in low voltage grids by distributed generators with inverter front-end," Ph.D. dissertation, Katholieke Universiteit Leuven - Faculteit Ingenieurswetenschappen - Departement Elektrotechniek, 2006.

[30] K. De Brabandere, B. Bolsens, J. Van den Keybus, A. Woyte, J. Driesen, and R. Belmans, "A voltage and frequency droop control method for parallel inverters," *IEEE Transactions on Power Electronics*, vol. 22, no. 4, pp. 1107–1115, July 2007.

[31] Y. W. Li and C.-N. Kao, "An accurate power control strategy for power-electronics-interfaced distributed generation units operating in a low-voltage multibus microgrid," *IEEE Transactions on Power Electronics*, vol. 24, no. 12, pp. 2977–2988, 2009.

[32] J. Guerrero, L. Garcia de Vicuña, J. Matas, M. Castilla, and J. Miret, "Output impedance design of parallel-connected UPS inverters with wireless load-sharing control," *IEEE Transactions on Industrial Electronics*, vol. 52, no. 4, pp. 1126–1135, 2005.

[33] J. Guerrero, J. Matas, L. de Vicuña, M. Castilla, and J. Miret, "Wireless-control strategy for parallel operation of distributed-generation invert-

ers," *IEEE Transactions on Industrial Electronics*, vol. 53, no. 5, pp. 1461–1470, 2006.

[34] C. Sao and P. Lehn, "Autonomous load sharing of voltage source converters," *IEEE Transactions on Power Delivery*, vol. 20, no. 2, pp. 1009–1016, 2005.

[35] Y.-R. Mohamed and E. El-Saadany, "Adaptive decentralized droop controller to preserve power sharing stability of paralleled inverters in distributed generation microgrids," *IEEE Transactions on Power Electronics*, vol. 23, no. 6, pp. 2806–2816, 2008.

[36] M. Prodanovic, K. De Brabandere, J. Van Den Keybus, T. Green, and J. Driesen, "Harmonic and reactive power compensation as ancillary services in inverter-based distributed generation," *IET Generation, Transmission Distribution*, vol. 1, no. 3, pp. 432–438, 2007.

[37] B. Kroposki, C. Pink, R. De Blasio, H. Thomas, M. Simões, and P. Sen, "Benefits of power electronic interfaces for distributed energy systems," *IEEE Transactions on Energy Conversion*, vol. 25, no. 3, pp. 901–908, Sept 2010.

[38] Y. T. Tan and D. Kirschen, "Impact on the power system of a large penetration of photovoltaic generation," in *2007 IEEE Power Engineering Society General Meeting*, June 2007.

[39] K. Turitsyn, P. Sulc, S. Backhaus, and M. Chertkov, "Options for control of reactive power by distributed photovoltaic generators," *Proceedings of the IEEE*, vol. 99, no. 6, pp. 1063–1073, June 2011.

[40] F. Andren, B. Bletterie, S. Kadam, P. Kotsampopoulos, and C. Bucher, "On the stability of local voltage control in distribution networks with a high penetration of inverter-based generation," *IEEE Transactions on Industrial Electronics*, vol. 62, no. 4, pp. 2519–2529, April 2015.

[41] P. Esslinger and R. Witzmann, "Evaluation of reactive power control concepts for PV inverters in low-voltage grids," in *CIRED 2012 Workshop on Integration of Renewables into the Distribution Grid*, May 2012.

[42] Y. Zhou, H. Li, and L. Liu, "Integrated autonomous voltage regulation and islanding detection for high penetration PV applications," *IEEE Transactions on Power Electronics*, vol. 28, no. 6, pp. 2826–2841, June 2013.

[43] L. Herman, B. Blazic, and I. Papic, "Voltage profile support in LV distribution networks with distributed generation," in *2009 Proceedings of the 44th International Universities Power Engineering Conference (UPEC)*, Sept 2009.

[44] P. Jahangiri and D. Aliprantis, "Distributed Volt/VAr control by PV inverters," *IEEE Transactions on Power Systems*, vol. 28, no. 3, pp. 3429–3439, Aug 2013.

[45] M. Farivar, L. Chen, and S. Low, "Equilibrium and dynamics of local voltage control in distribution systems," in *2013 IEEE 52nd Annual Conference on Decision and Control (CDC)*, Dec 2013, pp. 4329–4334.

[46] A. Hoke and D. Maksimovic, "Active power control of photovoltaic power systems," in *2013 1st IEEE Conference on Technologies for Sustainability (SusTech)*, Aug 2013, pp. 70–77.

[47] H. Alatrash, A. Mensah, E. Mark, G. Haddad, and J. Enslin, "Generator emulation controls for photovoltaic inverters," *IEEE Transactions on Smart Grid*, vol. 3, no. 2, pp. 996–1011, June 2012.

[48] H. Xin, Y. Liu, Z. Wang, D. Gan, and T. Yang, "A new frequency regulation strategy for photovoltaic systems without energy storage," *IEEE Transactions on Sustainable Energy*, vol. 4, no. 4, pp. 985–993, Oct 2013.

[49] A. Bidram and A. Davoudi, "Hierarchical structure of microgrids control system," *IEEE Transactions on Smart Grid*, vol. 3, no. 4, pp. 1963–1976, Dec 2012.

[50] A. Cagnano, E. De Tuglie, M. Liserre, and R. Mastromauro, "Online optimal reactive power control strategy of PV inverters," *IEEE Transactions on Industrial Electronics*, vol. 58, no. 10, pp. 4549–4558, Oct 2011.

[51] T. Caldognetto, P. Tenti, A. Costabeber, and P. Mattavelli, "Improving microgrid performance by cooperative control of distributed energy sources," *IEEE Transactions on Industry Applications*, vol. 50, no. 6, pp. 3921–3930, Nov 2014.

[52] S. Bolognani and S. Zampieri, "A distributed control strategy for reactive power compensation in smart microgrids," *IEEE Transactions on Automatic Control*, vol. 58, no. 11, pp. 2818–2833, Nov 2013.

[53] E. Dall'Anese, S. Dhople, and G. Giannakis, "Optimal dispatch of photovoltaic inverters in residential distribution systems," *IEEE Transactions on Sustainable Energy*, vol. 5, no. 2, pp. 487–497, April 2014.

[54] J. Sun, "Small-signal methods for AC distributed power systems - A review," *IEEE Transactions on Power Electronics*, vol. 24, no. 11, pp. 2545–2554, Nov 2009.

[55] B. Wen, D. Boroyevich, R. Burgos, P. Mattavelli, and Z. Shen, "Small-signal stability analysis of three-phase AC systems in the presence of constant power loads based on measured d-q frame impedances," *IEEE Transactions on Power Electronics*, vol. 30, no. 10, pp. 5952–5963, Oct 2015.

[56] S. Lissandron, "Analysis of the dynamics of the distribution network - e.g. analysis of the variability of loads and DERs," Nov 2014, internal report for Institute for Automation of Complex Power Systems (RWTH

Aachen University) on research activity for IDE4L European Project (`www.ide4l.eu`).

[57] J. Slootweg and W. Kling, "Impacts of distributed generation on power system transient stability," in *2002 IEEE Power Engineering Society Summer Meeting*, vol. 2, July 2002, pp. 862–867.

[58] M. Reza, D. Sudarmadi, F. Viawan, W. Kling, and L. van der Sluis, "Dynamic stability of power systems with power electronic interfaced DG," in *2006 IEEE PES Power Systems Conference and Exposition (PSCE 2006)*, Oct 2006, pp. 1423–1428.

[59] T. Alquthami, H. Ravindra, M. Faruque, M. Steurer, and T. Baldwin, "Study of photovoltaic integration impact on system stability using custom model of PV arrays integrated with PSS/E," in *2010 North American Power Symposium (NAPS)*, Sept 2010.

[60] M. Ilić, M. Cvetkovic, K. Bachovchin, and Q. Liu, "Modeling, analysis and control design complexities in future electric energy systems," in *2012 15th International Power Electronics and Motion Control Conference (EPE/PEMC)*, Sept 2012, pp. LS2b.3–1–LS2b.3–6.

[61] A. Emhemed, P. Crolla, and G. Burt, "Using real-time simulation to assess the impact of a high penetration of LV connected microgeneration on the wider system performance during severe low frequency," in *IECON 2011 - 37th Annual Conference on IEEE Industrial Electronics Society*, Nov 2011, pp. 3755–3760.

[62] S. Buso and T. Caldognetto, "Rapid prototyping of digital controllers for microgrid inverters," *IEEE Journal of Emerging and Selected Topics in Power Electronics*, vol. 3, no. 2, pp. 440–450, June 2015.

[63] R. D. Middlebrook, "Input filter considerations in design and application of switching regulators," in *Proceedings of IEEE Industry Applications Society Annual Meeting*, 1976, pp. 366–382.

[64] S. Vesti, T. Suntio, J. Oliver, R. Prieto, and J. Cobos, "Impedance-based stability and transient-performance assessment applying maximum peak criteria," *IEEE Transactions on Power Electronics*, vol. 28, no. 5, pp. 2099–2104, May 2013.

[65] M. Belkhayat, "Stability criteria for AC power systems with regulated loads," Ph.D. dissertation, Purdue University, 1997.

[66] A. G. J. MacFarlane and I. Postlethwaite, "The generalized Nyquist stability criterion and multivariable root loci," *International Journal of Control*, vol. 25, no. 1, pp. 81–127, 1977.

[67] L. Harnefors, M. Bongiorno, and S. Lundberg, "Input-admittance calculation and shaping for controlled voltage-source converters," *IEEE Transactions on Industrial Electronics*, vol. 54, no. 6, pp. 3323–3334, Dec 2007.

[68] M. Cespedes and J. Sun, "Impedance modeling and analysis of grid-connected voltage-source converters," *IEEE Transactions on Power Electronics*, vol. 29, no. 3, pp. 1254–1261, March 2014.

[69] E. Möllerstedt and B. Bernhardsson, "Out of control because of harmonics - An analysis of the harmonic response of an inverter locomotive," *IEEE Control Systems*, vol. 20, no. 4, pp. 70–81, Aug 2000.

[70] "ENTSO-E Network code for Requirements for Grid Connection Applicable to all Generators," March 8th, 2013.

[71] pr TS 50549-1, "Requirements for the connection of generators above 16 A per phase - Part 1: Connection to the LV distribution system (CLC TC 8X)," Status: approval stage.

[72] pr TS 50549-2, "Requirements for the connection of generators above 16 A per phase - Part 2: Connection to the MV distribution system (CLC TC 8X)," Status: approval stage.

[73] R. Sgarbossa, S. Lissandron, P. Mattavelli, R. Turri, and A. Cerretti, "Analysis of $\Delta P - \Delta Q$ area of uncontrolled islanding in low voltage grids with PV generators," in *2014 IEEE Energy Conversion Congress and Exposition (ECCE)*, Sept 2014, pp. 5667–5674.

[74] S. Lissandron, R. Sgarbossa, L. Dalla Santa, P. Mattavelli, R. Turri, and A. Cerretti, "Impact of non-simultaneous P/f and Q/V grid code requirements on PV inverters on unintentional islanding operation in distribution network," in *2015 IEEE 6th International Symposium on Power Electronics for Distributed Generation Systems (PEDG)*, June 2015.

[75] R. Walling and N. Miller, "Distributed generation islanding-implications on power system dynamic performance," in *2002 IEEE Power Engineering Society Summer Meeting*, vol. 1, July 2002, pp. 92–96.

[76] Z. Ye, A. Kolwalkar, Y. Zhang, P. Du, and R. Walling, "Evaluation of anti-islanding schemes based on nondetection zone concept," *IEEE Transactions on Power Electronics*, vol. 19, no. 5, pp. 1171–1176, Sept 2004.

[77] F. Noor, R. Arumugam, and M. Vaziri, "Unintentional islanding and comparison of prevention techniques," in *Proceedings of the 37th Annual North American Power Symposium (2005)*, 2005, pp. 90–96.

[78] R. Teodorescu, M. Liserre, and P. Rodriguez, *Grid Converters for Photovoltaic and Wind Power Systems*. Wiley-IEEE Press, 2011, ch. 5.

[79] I. Balaguer, H.-G. Kim, F. Peng, and E. Ortiz, "Survey of photovoltaic power systems islanding detection methods," in *2008 IECON 34th Annual Conference of IEEE Industrial Electronics*, Nov 2008, pp. 2247–2252.

[80] R. Kunte and W. Gao, "Comparison and review of islanding detection techniques for distributed energy resources," in *2008. NAPS '08. 40th North American Power Symposium*, 2008, pp. 1–8.

[81] D. Reigosa, F. Briz, C. Charro, P. Garcia, and J. Guerrero, "Active islanding detection using high-frequency signal injection," *IEEE Transactions on Industry Applications*, vol. 48, no. 5, pp. 1588–1597, Sept 2012.

[82] H. Zeineldin, E. El-Saadany, and M. Salama, "Impact of DG interface control on islanding detection and nondetection zones," *IEEE Transactions on Power Delivery*, vol. 21, no. 3, pp. 1515–1523, July 2006.

[83] A. Ghaderi and M. Kalantar, "Investigation of influential factors on passive islanding detection methods of inverter based distributed generation," in *2011 2nd Power Electronics, Drive Systems and Technologies Conference (PEDSTC)*, Feb 2011, pp. 217–222.

[84] O. Raipala, A. Mäkinen, S. Repo, and P. Järventausta, "The effect of different control modes and mixed types of DG on the non-detection zones of islanding detection," in *CIRED 2012 Workshop Integration of Renewables into the Distribution Grid*, May 2012, pp. 1–4.

[85] H. Zeineldin and M. Salama, "Impact of load frequency dependence on the NDZ and performance of the SFS islanding detection method," *IEEE Transactions on Industrial Electronics*, vol. 58, no. 1, pp. 139–146, Jan 2011.

[86] B. Bahrani, H. Karimi, and R. Iravani, "Nondetection zone assessment of an active islanding detection method and its experimental evaluation," *IEEE Transactions on Power Delivery*, vol. 26, no. 2, pp. 517–525, April 2011.

[87] "IEEE standard conformance test procedures for equipment interconnecting distributed resources with electric power systems," *IEEE Std 1547.1-2005*, pp. 1–62, July 2005.

[88] D. Salles, W. Freitas, J. Vieira, and B. Venkatesh, "A practical method for nondetection zone estimation of passive anti-islanding schemes applied to synchronous distributed generators," *IEEE Transactions on Power Delivery*, vol. 30, no. 5, pp. 2066–2076, Oct 2015.

[89] J. Bruschi, F. Cadoux, B. Raison, Y. Bésanger, and S. Grenard, "Impact of new european grid codes requirements on anti-islanding protections: a case study," in *23rd International Conference and Exhibition on Electricity Distribution (CIRED 2015)*, June 2015.

[90] L. A. C. Lopes and Y. Zhang, "Islanding detection assessment of multi-inverter systems with active frequency drifting methods," *IEEE Transactions on Power Delivery*, vol. 23, no. 1, pp. 480–486, Jan 2008.

[91] A. Cerretti, G. Scrosati, and L. Consiglio, "Upgrade of ENEL MV network automation to improve performances in presence of faults and to deal DG," in *21st International Conference and Exhibition on Electricity Distribution (CIRED 2011)*, June 2011.

[92] "Load representation for dynamic performance analysis [of power systems]," *IEEE Transactions on Power Systems*, vol. 8, no. 2, pp. 472–482, 1993.

[93] S. Lissandron, R. Sgarbossa, L. Dalla Santa, P. Mattavelli, R. Turri, and A. Cerretti, "$\Delta P - \Delta Q$ area assessment of temporary unintentional islanding with P/f and Q/V droop controlled PV generators in distribution networks," in *2015 IEEE Energy Conversion Congress and Exposition (ECCE)*, Sept 2015, pp. 1968–1975.

[94] S.-K. Chung, "Phase-locked loop for grid-connected three-phase power conversion systems," *IEE Proceeding on Electric Power Applications*, vol. 147, no. 3, pp. 213–219, May 2000.

[95] V. Kaura and V. Blasko, "Operation of a phase locked loop system under distorted utility conditions," *IEEE Transactions on Industry Applications*, vol. 33, no. 1, pp. 58–63, Jan 1997.

[96] R. Caldon, M. Coppo, R. Sgarbossa, L. Sgarbossa, and R. Turri, "Risk of unintentional islanding in LV distribution networks with inverter-based DGs," in *2013 48th International Universities Power Engineering Conference (UPEC)*, 2013, pp. 1–6.

[97] *DIgSILENT Power Factory 14.0 Manual*, `www.digsilent.de`.

[98] K. Tomiyama, S. Ueoka, T. Takano, I. Iyoda, K. Matsuno, K. Temma, and J. Paserba, "Modeling of load during and after system faults based on actual field data," in *2003 IEEE Power Engineering Society General Meeting*, vol. 3, July 2003.

[99] D. Dong, J. Li, D. Boroyevich, P. Mattavelli, I. Cvetkovic, and Y. Xue, "Frequency behavior and its stability of grid-interface converter in distributed generation systems," in *2012 27th Annual IEEE Applied Power Electronics Conference and Exposition (APEC)*, Feb 2012, pp. 1887–1893.

[100] S. Lissandron and P. Mattavelli, "A controller for the smooth transition from grid-connected to autonomous operation mode," in *2014 IEEE Energy Conversion Congress and Exposition (ECCE)*, Sept 2014, pp. 4298–4305.

[101] Y.-R. Mohamed and A. Radwan, "Hierarchical control system for robust microgrid operation and seamless mode transfer in active distribution systems," *IEEE Transactions on Smart Grid*, vol. 2, no. 2, pp. 352–362, 2011.

[102] S.-H. Hu, C.-Y. Kuo, T.-L. Lee, and J. Guerrero, "Droop-controlled inverters with seamless transition between islanding and grid-connected operations," in *2011 IEEE Energy Conversion Congress and Exposition (ECCE)*, 2011, pp. 2196–2201.

[103] Y. A. R. I. Mohamed, H. Zeineldin, M. Salama, and R. Seethapathy, "Seamless formation and robust control of distributed generation microgrids via direct voltage control and optimized dynamic power sharing," *IEEE Transactions on Power Electronics*, vol. 27, no. 3, pp. 1283–1294, Mar 2012.

[104] A. Kahrobaeian and Y.-R. Mohamed, "Interactive distributed generation interface for flexible micro-grid operation in smart distribution systems,"

IEEE Transactions on Sustainable Energy, vol. 3, no. 2, pp. 295–305, Apr 2012.

[105] J. Guerrero, J. Vasquez, J. Matas, M. Castilla, and L. de Vicuña, "Control strategy for flexible microgrid based on parallel line-interactive UPS systems," *IEEE Transactions on Industrial Electronics*, vol. 56, no. 3, pp. 726–736, 2009.

[106] T. Vandoorn, B. Meersman, J. D. Kooning, and L. Vandevelde, "Transition from islanded to grid-connected mode of microgrids with voltage-based droop control," *IEEE Transactions on Power Systems*, vol. 28, no. 3, pp. 2545–2553, 2013.

[107] B. Ren, X. Tong, S. Tian, and X. Sun, "Research on the control strategy of inverters in the micro-grid," in *2010 Asia-Pacific Power and Energy Engineering Conference (APPEEC)*, 2010, pp. 1–4.

[108] F. Gao and M. Iravani, "A control strategy for a distributed generation unit in grid-connected and autonomous modes of operation," *IEEE Transactions on Power Delivery*, vol. 23, no. 2, pp. 850–859, April 2008.

[109] Z. Liu, J. Liu, and Y. Zhao, "A unified control strategy for three-phase inverter in distributed generation," *IEEE Transactions on Power Electronics*, vol. 29, no. 3, pp. 1176–1191, March 2014.

[110] C. Cho, J.-H. Jeon, J.-Y. Kim, S. Kwon, K. Park, and S. Kim, "Active synchronizing control of a microgrid," *IEEE Transactions on Power Electronics*, vol. 26, no. 12, pp. 3707–3719, Dec 2011.

[111] K. Tan, X. Peng, P. So, Y. Chu, and M. Chen, "Centralized control for parallel operation of distributed generation inverters in microgrids," *IEEE Transactions on Smart Grid*, vol. 3, no. 4, pp. 1977–1987, Dec 2012.

[112] J.-H. Jeon, J.-Y. Kim, H.-M. Kim, S.-K. Kim, C. Cho, J.-M. Kim, J.-B. Ahn, and K.-Y. Nam, "Development of hardware in-the-loop simulation

system for testing operation and control functions of microgrid," *IEEE Transactions on Power Electronics*, vol. 25, no. 12, pp. 2919–2929, Dec 2010.

[113] L. Meegahapola, D. Robinson, A. Agalgaonkar, S. Perera, and P. Ciufo, "Microgrids of commercial buildings: Strategies to manage mode transfer from grid connected to islanded mode," *IEEE Transactions on Sustainable Energy*, vol. 5, no. 4, pp. 1337–1347, Oct 2014.

[114] G. Azevedo, F. Bradaschia, M. Cavalcanti, F. Neves, J. Rocabert, and P. Rodriguez, "Safe transient operation of microgrids based on master-slave configuration," in *2011 IEEE Energy Conversion Congress and Exposition (ECCE)*, 2011, pp. 2191–2195.

[115] S. Mishra, D. Ramasubramanian, and P. Sekhar, "A seamless control methodology for a grid connected and isolated PV-diesel microgrid," *IEEE Transactions on Power Systems*, vol. 28, no. 4, pp. 4393–4404, Nov 2013.

[116] M. Delghavi and A. Yazdani, "A unified control strategy for electronically interfaced distributed energy resources," *IEEE Transactions on Power Delivery*, vol. 27, no. 2, pp. 803–812, 2012.

[117] N. Pogaku, M. Prodanovic, and T. Green, "Modeling, analysis and testing of autonomous operation of an inverter-based microgrid," *IEEE Transactions on Power Electronics*, vol. 22, no. 2, pp. 613–625, 2007.

[118] M. Hassan and M. Abido, "Optimal design of microgrids in autonomous and grid-connected modes using particle swarm optimization," *IEEE Transactions on Power Electronics*, vol. 26, no. 3, pp. 755–769, 2011.

[119] E. Barklund, N. Pogaku, M. Prodanovic, C. Hernandez-Aramburo, and T. Green, "Energy management in autonomous microgrid using stability-constrained droop control of inverters," *IEEE Transactions on Power Electronics*, vol. 23, no. 5, pp. 2346–2352, Sept 2008.

[120] Z. Zeng, H. Yang, and R. Zhao, "Study on small signal stability of microgrids: A review and a new approach," *Renewable and Sustainable Energy Reviews*, vol. 15, no. 9, pp. 4818–4828, 2011.

[121] "National instruments' webpage," 2013, `www.ni.com`.

[122] S. Lissandron, L. Dalla Santa, P. Mattavelli, and B. Wen, "Experimental validation for impedance-based small-signal stability analysis of single-phase interconnected power systems with grid-feeding inverters," *IEEE Journal of Emerging and Selected Topics in Power Electronics*, 2015.

[123] M. Cespedes and J. Sun, "Renewable energy systems instability involving grid-parallel inverters," in *24th Annual IEEE Applied Power Electronics Conference and Exposition (APEC 2009)*, Feb 2009, pp. 1971–1977.

[124] S. Acevedo and M. Molinas, "Power electronics modeling fidelity: Impact on stability estimate of micro-grid systems," in *2011 IEEE PES Innovative Smart Grid Technologies Asia (ISGT)*, Nov 2011.

[125] J. Sun and Z. Bing, "Input impedance modeling of single-phase PFC by the method of harmonic linearization," in *2008 Twenty-Third Annual IEEE Applied Power Electronics Conference and Exposition (APEC 2008)*, Feb 2008, pp. 1188–1194.

[126] J. Sun, "Impedance-based stability criterion for grid-connected inverters," *IEEE Transactions on Power Electronics*, vol. 26, no. 11, pp. 3075–3078, Nov 2011.

[127] J. Huang, "AC/DC power system small-signal impedance measurement for stability analysis," Ph.D. dissertation, Missouri University of Science and Technology, 2009.

[128] J. Huang, K. Corzine, and M. Belkhayat, "Single-phase AC impedance modeling for stability of integrated power systems," in *IEEE ESTS 2007 Electric Ship Technologies Symposium*, May 2007, pp. 483–489.

[129] H. Wang, W. Mingli, and J. Sun, "Analysis of low-frequency oscillation in electric railways based on small-signal modeling of vehicle-grid system in dq frame," *IEEE Transactions on Power Electronics*, vol. 30, no. 9, pp. 5318–5330, Sept 2015.

[130] A. Paice and M. Meyer, "Rail network modelling and stability: the input admittance criterion," in *14th Int. Symp. Math. Theory Netw. Syst., Perpignan, France*, 2000.

[131] M. Jansson, A. Danielsson, J. Galic, K. Pietiläinen, and L. Harnefors, "Stable and passive traction drives," in *Proceedings of IEEE Nordic Power and Industrial Electronics Conference*, 2004.

[132] S. Danielsen, O. B. Fosso, M. Molinas, J. A. Suul, and T. Toftevaag, "Simplified models of a single-phase power electronic inverter for railway power system stability analysis–development and evaluation," *Electric Power Systems Research*, vol. 80, no. 2, pp. 204–214, 2010.

[133] C. Heising, M. Oettmeier, V. Staudt, A. Steimel, and S. Danielsen, "Improvement of low-frequency railway power system stability using an advanced multivariable control concept," in *35th Annual Conference of IEEE Industrial Electronics (IECON '09)*, Nov 2009, pp. 560–565.

[134] L. Harnefors, "Modeling of three-phase dynamic systems using complex transfer functions and transfer matrices," *IEEE Transactions on Industrial Electronics*, vol. 54, no. 4, pp. 2239–2248, Aug 2007.

[135] J. Kwon, X. Wang, C. Bak, and F. Blaabjerg, "Harmonic instability analysis of single-phase grid connected converter using harmonic state space (HSS) modeling method," in *2015 IEEE Energy Conversion Congress and Exposition (ECCE)*, Sept 2015, pp. 2421–2428.

[136] N. M. Wereley, "Analysis and control of linear periodically time varying systems," Ph.D. dissertation, Massachusetts Institute of Technology, Dept. of Aeronautics and Astronautics, 1991.

[137] B. Wen, D. Boroyevich, R. Burgos, P. Mattavelli, and Z. Shen, "Analysis of D-Q small-signal impedance of grid-tied inverters," *IEEE Transactions on Power Electronics*, vol. 31, no. 1, pp. 675–687, Jan 2016.

[138] B. Wen, D. Dong, D. Boroyevich, R. Burgos, P. Mattavelli, and Z. Shen, "Impedance-based analysis of grid-synchronization stability for three-phase paralleled converters," *IEEE Transactions on Power Electronics*, vol. 31, no. 1, pp. 26–38, Jan 2016.

[139] S. Lissandron, L. Dalla Santa, P. Mattavelli, and B. Wen, "Validation of impedance-based small-signal stability analysis for single-phase grid-feeding inverters with PLL," in *2015 IEEE 6th International Symposium on Power Electronics for Distributed Generation Systems (PEDG)*, June 2015.

[140] X. Wang, F. Blaabjerg, and W. Wu, "Modeling and analysis of harmonic stability in an ac power-electronics-based power system," *IEEE Transactions on Power Electronics*, vol. 29, no. 12, pp. 6421–6432, Dec 2014.

[141] C. Zhang, X. Wang, and F. Blaabjerg, "Analysis of phase-locked loop influence on the stability of single-phase grid-connected inverter," in *2015 IEEE 6th International Symposium on Power Electronics for Distributed Generation Systems (PEDG)*, June 2015.

[142] V. Caliskan, G. C. Verghese, and A. Stankovic, "Multifrequency averaging of DC/DC converters," *IEEE Transactions on Power Electronics*, vol. 14, no. 1, pp. 124–133, Jan 1999.

[143] L. Fangcheng, L. Jinjun, Z. Bin, Z. Haodong, and H. Ul, "General impedance/admittance stability criterion for cascade system," in *2013 IEEE ECCE Asia Downunder (ECCE Asia)*, June 2013, pp. 422–428.

[144] M. Jaksic, D. Boroyevich, R. Burgos, Z. Shen, I. Cvetkovic, and P. Mattavelli, "Modular interleaved single-phase series voltage injection converter used in small-signal dq impedance identification," in *2014 IEEE*

Energy Conversion Congress and Exposition (ECCE), Sept 2014, pp. 3036–3045.

[145] J. Huang, K. Corzine, and M. Belkhayat, "Small-signal impedance measurement of power-electronics-based ac power systems using line-to-line current injection," *IEEE Transactions on Power Electronics*, vol. 24, no. 2, pp. 445–455, Feb 2009.

[146] F. Blaabjerg, R. Teodorescu, M. Liserre, and A. Timbus, "Overview of control and grid synchronization for distributed power generation systems," *IEEE Transactions on Industrial Electronics*, vol. 53, no. 5, pp. 1398–1409, Oct 2006.

[147] R. Santos Filho, P. Seixas, P. Cortizo, L. Torres, and A. Souza, "Comparison of three single-phase PLL algorithms for UPS applications," *IEEE Transactions on Industrial Electronics*, vol. 55, no. 8, pp. 2923–2932, Aug 2008.

[148] D. Zmood, D. Holmes, and G. Bode, "Frequency-domain analysis of three-phase linear current regulators," *IEEE Transactions on Industry Applications*, vol. 37, no. 2, pp. 601–610, Mar 2001.

[149] D. Zmood and D. Holmes, "Stationary frame current regulation of PWM inverters with zero steady-state error," *IEEE Transactions on Power Electronics*, vol. 18, no. 3, pp. 814–822, May 2003.

[150] "IDE4L European project' webpage," 2014, `www.ide4l.eu`.

[151] H. K. Khalil, *Nonlinear Systems*, 3rd ed., 2002, pp. 423–434.

[152] T. V. Cutsem and C. Vournas, *Voltage Stability of Electric Power Systems*. Springer Science and Business Media, 1998.

[153] T. Esram and P. Chapman, "Comparison of photovoltaic array maximum power point tracking techniques," *IEEE Transactions on Energy Conversion*, vol. 22, no. 2, pp. 439–449, June 2007.

[154] S. Lissandron, A. Costabeber, and P. Mattavelli, "A generalized method to analyze the small-signal stability for a multi-inverter islanded grid with droop controllers," in *15th European Conference on Power Electronics and Applications (EPE 2013)*, 2013, pp. 1–10.

[155] M. Marwali, J.-W. Jung, and A. Keyhani, "Stability analysis of load sharing control for distributed generation systems," *IEEE Transactions on Energy Conversion*, vol. 22, no. 3, pp. 737–745, 2007.

List of Figures

List of Tables